THE UNIVERSITY OF QUEENSLAND

AUSTRALIA

Synthesis of Hollow-structured Electrode Material for Energy Storage

Xiaoran Sun

Master of Engineering

A thesis submitted for the degree of Doctor of Philosophy at

The University of Queensland in 2017

Australian Institute for Bioengineering and Nanotechnology

Abstract

Due to the high specific surface area, high chemical stability and good characteristics of electrical and thermal conductivity, hollow-structured materials have attracted extensive research interest as electrode materials for energy storage applications. The high specific surface area of hollow-structured materials provides a high contact area with electrolyte, facilitating the rapid diffusion and transport of electrolyte ions. The walls of electrode materials in hollow structures are relatively thin, providing short electron/ion diffusion length. Besides, the voids in hollow structures are beneficial for accommodating the volume expansion of the anode materials in lithium-ion batteries. Thus the specific capacity and cycling stability of the energy storage devices is enhanced with increased utilization of the electrode materials. However, it still remains challenging on maintaining the stability of the delicate hollow structure during cycling. Developing a facile strategy for the large-scale synthesis of hollow-structured electrode materials is worth studying as well.

The aims of this project include the design and synthesis of transition metal oxides hollow microspheres for lithium-ion battery application and highly porous carbon microspheres for supercapacitor and aluminum ion battery applications. In the aspect of transition metal oxides, double-shelled polypyrrole-zinc ferrite hollow microspheres will be fabricated and its electrochemical properties will be investigated. In the other aspect of highly porous carbon, nitrogen-doped mesopore-dominated carbon microspheres will be synthesized and its electrochemical properties will be investigated. Nitrogen-doped macroporous carbon microspheres will be fabricated and its structural parameters will be investigated. The specific achievements obtained in this thesis are listed as follows:

Nanocompositing is known as a promising approach for the structural stabilization of the preformed hollow structures. In the first part, $ZnFe_2O_4$ double-shell hollow microspheres are synthesized for the accommodation of the large volume expansion during lithiation. A facile and efficient vapor-phase polymerization method is developed to coat the $ZnFe_2O_4$ hollow spheres with polypyrrole. The thin polypyrrole coating improves not only the electronic conductivity but also the structural integrity of the $ZnFe_2O_4$ hollow spheres. When evaluated as the anode in lithium-ion batteries, the polypyrrole coated $ZnFe_2O_4$ hollow spheres manifest significantly improved cycling stability and rate capability than the pristine $ZnFe_2O_4$ hollow spheres.

Apart from transition metal oxide hollow spheres that used as anode in lithium-ion batteries, highly porous carbon materials show great potential on supercapacitors and other energy storage devices. Thus, in the second part, we develop a novel "spray drying-vapour deposition" method for the synthesis of the N-doped mesoporous carbon microspheres, in which, commercial Ludox silica nanoparticles are used as porogens for the surfactant-free synthesis. The resultant mesoporous

carbon microspheres possess a mesopore-dominate (95%) high surface area of 1528 m^2/g, an increased apparent density of 0.5 g/cm^3, thin walls with a high nitrogen content of 8 At %, and consequently superior gravimetric/volumetric capacitance performance (533.6 F/g and 208.1 F/cm^3) as an electrode material in EDLCs.

Following the second part, the developed "spray drying-vapour deposition" strategy is extended to the synthesis of N-doped three-dimensionally ordered macroporous carbon microspheres. The hexagonal-close-packed periodicity of macropores is achieved through the spray drying method. Vapour deposition of polypyrrole followed by carbonization and etching is beneficial for the generation of carbon network with a wall thickness of 3.5 nm. The resultant three-dimensionally ordered macroporous carbon microspheres possess a hexagonal close packing structure with a high surface area of 892 m^2/g, an ultrahigh pore volume of 7.5 cm^3/g and a high nitrogen doping of 8 At%. As a result, the synthesized three-dimensionally ordered macroporous carbon microspheres show good reversible capacity in aluminum ion batteries.

In conclusion, our innovative approaches in this thesis have shown great potentials in stabilizing the hollow structure of transition metal oxides and fabricating highly porous carbon materials, which is important for enhancing the electrochemical properties of the electrode for energy storage applications.

Declaration by author

This thesis *is composed of my original work, and contains* no material previously published or written by another person except where due reference has been made in the text. I have clearly stated the contribution by others to jointly-authored works that I have included in my thesis.

I have clearly stated the contribution of others to my thesis as a whole, including statistical assistance, survey design, data analysis, significant technical procedures, professional editorial advice, and any other original research work used or reported in my thesis. The content of my thesis is the result of work I have carried out since the commencement of my research higher degree candidature and does not include a substantial part of work that has been submitted *to qualify for the award of any* other degree or diploma in any university or other tertiary institution. I have clearly stated which parts of my thesis, if any, have been submitted to qualify for another award.

I acknowledge that an electronic copy of my thesis must be lodged with the University Library and, subject to the policy and procedures of The University of Queensland, the thesis be made available for research and study in accordance with the Copyright Act 1968 unless a period of embargo has been approved by the Dean of the Graduate School.

I acknowledge that copyright of all material contained in my thesis resides with the copyright holder(s) of that material. Where appropriate I have obtained copyright permission from the copyright holder to reproduce material in this thesis.

<u>Publications during candidature</u>

Peer-reviewed papers

1. **<u>Sun, Xiaoran</u>**; Zhang, Hongwei; Zhou, Liang*; Huang, Xiaodan; Yu, Chengzhong*. Polypyrrole-Coated Zinc Ferrite Hollow Spheres with Improved Cycling Stability for Lithium-Ion Batteries. *Small*, **2016**, 12 (27), 3732-3737. (Top 10 hot paper of Small in June 2016; highlighted in MaterialsViews China)

2. Shen, Guozhu; **<u>Sun, Xiaoran</u>**; Zhang, Hongwei; Liu, Yang; Zhang, Jun; Meka, Anand; Zhou, Liang*; Yu, Chengzhong*. Nitrogen-doped ordered mesoporous carbon single crystals: aqueous organic–organic self-assembly and superior supercapacitor performance. *J. Mater. Chem. A,* **2015**, 3 (47), 24041-24048.

3. Zhang, Hongwei; **<u>Sun, Xiaoran</u>**; Huang, Xiaodan; Zhou, Liang*. Encapsulation of α-Fe_2O_3 nanoparticles in graphitic carbon microspheres as high-performance anode materials for lithium-ion batteries, *Nanoscale*, **2015**, *7*, 3270-3275.

4. Lei, Chang; Zhou, Liang; Xu, Chun; **<u>Sun, Xiaoran</u>**; Nouwens, Amanda; Yu, Chengzhong*. Binder-free TiO_2 Monolith Packed Pipette-tips for the Enrichment of Phosphorylated Peptides. *Aust J Chem,* **2016** (CH16443.R1).

Conference proceedings

Posters:

1) **<u>Sun, Xiaoran</u>**. Polypyrrole-coated Transition Metal Oxide Hollow Spheres with Improved Cycling Stability for Lithium Ion Batteries. **<u>Asia Pacific Conference on Energy and Environmental Materials (APCEEM),</u>** 9th –11th February 2014, Gold Coast City, QLD, Australia.

2) **<u>Sun, Xiaoran</u>**. Polypyrrole-Coated Zinc Ferrite Hollow Spheres with Improved Cycling Stability for Lithium-Ion Batteries. **<u>NanoBio Australia 2014,</u>** 7th – 10th July 2014, Brisbane, Australia.

3) **<u>Sun, Xiaoran</u>**. N-doped mesoporous carbon microsphere by spray drying-vapour deposition for supercapacitor. **<u>The 8th International Symposium on Nano & Supramolecular Chemistry (ISNSC8),</u>** 13th – 16th July 2016, Brisbane, Australia.

Publications included in this thesis

1. **Sun, Xiaoran**; Zhang, Hongwei; Zhou, Liang*; Huang, Xiaodan; Yu, Chengzhong*. Polypyrrole-Coated Zinc Ferrite Hollow Spheres with Improved Cycling Stability for Lithium-Ion Batteries. *Small*, **2016**, 12 (27), 3732-3737. – incorporated as Chapter 4

Contributors	Statement of contribution
Author Sun, Xiaoran (Candidate)	Experimental design and performance (80%) Analysis and interpretation of data (75 %) Drafting and writing (70 %)
Author Dr. Zhang, Hongwei	Analysis and interpretation of data (15 %) Drafting and writing (5 %)
Author Prof. Zhou, Liang	Experimental design and performance (15%) Analysis and interpretation of data (10 %) Drafting and writing (15 %)
Author Dr. Huang, Xiaodan	Drafting and writing (5 %)
Author Prof. Yu, Chengzhong	Experimental design and performance (5%) Drafting and writing (5 %)

Contributions by others to the thesis

All X-ray photoelectron spectroscopy (XPS) measurements were conducted by Dr Barry J Wood.

Statement of parts of the thesis submitted to qualify for the award of another degree

None

Acknowledgements

Australian and New Zealand Standard Research Classifications (ANZSRC)

ANZSRC code: 091205, Functional materials, 40%

ANZSRC code: 100708, Nanomaterials, 20%

ANZSRC code: 030604, electrochemistry, 40%

Fields of Research (FoR) Classification

FoR code: 0912, Material Engineering, 40%

FoR code: 0904, Chemical Engineering, 30%

FoR code: 1007, Nanotechnology, 40%

Table of Contents

List of Abbreviations used in the thesis

3DOM: Three-dimensionally ordered macroporous

AD: Air drying

AIBs: Aluminum-ion batteries

BET: Brunauer–Emmett–Teller

BJH: Barrett–Joyner–Halanda

CNTs: Carbon nanotubes

CV: Cyclic voltammetry

CVD: Chemical vapour deposition

DEC: Dimethyl carbonate

DLS: Dynamic light scattering

EA: Elemental analysis

EC: Ethylene carbonate

EDLCs: Electric double layer capacitors

EDS: Energy-dispersive X-ray spectroscopy

EIS: Electrochemical impedance spectroscopy

EISA: Evaporation induced self-assembly

EMC: Ethylmethyl carbonate

ET: Electron tomography

FD: Freeze drying

FTIR: Fourier transform infrared

FWHM: Full width at half maximum

GO: Graphite oxide

HF: Hydrofluoric acid

HRTEM: High-resolution transmission electron microscopy

LIBs: Lithium-ion batteries

MC: Mesoporous carbon

NMP: N-Methyl-2-pyrrolidone

PPY: Polypyrrole

PTFE: Polytetrafluoroethylene

PVDF: Polyvinylidene fluoride

rGO: Reduced graphene oxide

SAED: Selected area electron diffraction

SAXS: Small-angle x-ray scattering

SD: Spray drying

SEI: Solid electrolyte interphase

SEM: Scanning electron microscopy

STEM: Scanning transmission electron microscopy

TEM: Transmission electron microscopy

TEOS: Tetraethyl orthosilicate

TGA: Thermogravimetric analysis

TMOs: Transition metal oxides

XPS: X-ray photoelectron spectroscopy

XRD: X-ray diffraction

Chapter 1

Introduction

This chapter introduces the background of this project and outlines the research objectives.

1.1 Significance of the project

Metal oxides and carbon-based materials are promising electrode materials for high-efficient energy storage devices. Creating unique nanostructures of metal oxides and carbon materials is essential for the development of electrode with high energy density and power density. Hollow and porous structures have attracted tremendous attention because of their high specific surface area, high chemical stability and good characteristics of electrical and thermal conductivity.[1] The main advantages of hollow-structured electrode materials are list as follows: 1) A high surface area permits high contact area with electrolyte, thus facilitate the rapid diffusion and transport of electrolyte ions; 2) the walls of electrode material in hollow/porous structure are relatively thin, providing short electron/ion diffusion length; 3) the utilization of the electrode material is increased, which enhance the rate performance and cycling stability.

Transition metal oxides (TMOs) have great potential as anode material for lithium-ion battery (LIB) applications.[2] The theoretical capacity of TMOs can reach up to around 1000 mA h g^{-1}, which is approximately two times higher than the commercial graphite (372 mA h g^{-1}).[3] However, TMOs still suffer from large volume variation during lithiation-delithiation and poor electrical conductivity, which limits their cycling stability and rate capability.[4] Constructing hollow structures have been recognized as a promising strategy to address the volume variation issue. The interior void is capable of accommodating the volume variation and alleviating the structural strain during cycling.[5] In addition, the hollow structure is usually composed of nanoparticulate thin shells, which provide short pathways for lithium ion/electron diffusion.[6] Another advantage of the hollow structure is the high surface to volume ratio. The high specific surface area enables a high electrode-electrolyte contact area, facilitating the electrochemical reaction. Furthermore, by employing a second component as the protective coating layer on the surface of hollow TMOs, the integration of hollow structuring and nanocompositing offers the opportunity to address the volume variation and poor conductivity issues of TMOs simultaneously.

Porous carbons are at the frontier of research in materials science. So far, the soft-templating method and hard-templating method are two general methods developed for the preparation of porous carbon materials.[7] The soft-templating method based on the self-assembly between surfactants (*e.g.*, block copolymers) and carbon precursors (*e.g.*, phenolic resins).[8] On the other hand, the hard-templating method involves the coating process of carbon precursors to preformed templates, followed by carbonization and selectively etching to obtain carbon products.[9] However, the synthesis was usually conducted in solutions,[10] resulting in carbon materials with irregular morphology and relatively low packing density, thus unfavorable for the volumetric performance of batteries and EDLCs.[11] Spray drying is not only a facile method for the synthesis of multi-shelled

hollow metal oxides,[12] but also for the synthesis of porous carbons through assembling colloidal silica nanoparticles into microspherical templates.[13] Besides, compared to conventional infiltration and high-temperature chemical vapour deposition (CVD),[14] low-temperature vapour deposition achieves uniform coating and maintains the structural stability of the template.[15] It remains a challenge to synthesize porous carbon with high gravimetric/volumetric performance via spray drying–vapour deposition method. And the structural symmetry of porous carbons synthesized by spray drying–vapour deposition method has not been investigated.

1.2 Research objective and scope

This project aims at developing spray drying-vapour deposition method to fabricate polypyrrole coated transition metal oxides hollow spheres and polypyrrole-derived porous carbon microspheres for energy storage applications. Firstly, polypyrrole coated zinc oxide double-shell hollow microspheres will be synthesized and applied as anode material for LIBs. Next, nitrogen-doped mesoporous carbon microspheres will be synthesized through spray drying-vapour deposition method. The potential of the resultant mesoporous carbon microspheres on EDLCs will be investigated. In addition, the three-dimensional ordered structure of nitrogen-doped macroporous carbon microspheres synthesized via spray drying-vapour deposition method will be demonstrated. The objectives of this project are specified as follows:

1)   Understanding the influence of polypyrrole coating on the electrochemical performance of transition metal oxide (e.g. zinc ferrite) for LIBs applications;

2)   Developing novel method to synthesize nitrogen-doped mesoporous carbon microspheres with high mesopore surface area and increased packing density for EDLCs applications;

3)   Investigating the porous structure of three-dimensionally ordered macroporous carbon microspheres prepared by the spray drying-vapour deposition method.

1.3 Thesis outline

This thesis is written according to the guidelines of the University of Queensland. The chapters in this thesis are presented in the following sequence:

Chapter 1 Introduction

This chapter introduces the background of this project and outlines the research objectives.

Chapter 2 Literature review

This chapter presents an overview of the application of hollow-structured metal oxide and porous carbon materials in batteries and supercapacitors. The synthesis of hollow-structured metal oxide and porous carbon materials are also reviewed in this chapter.

Chapter 3 Research methodology

This chapter summarizes the synthetic methods and characterizations of the materials used in this Ph.D. project. The techniques used for the electrochemical test are also included in this chapter.

Chapter 4 Polypyrrole coated zinc ferrite hollow spheres with improved cycling stability for lithium-ion batteries

This chapter reports the synthesis of polypyrrole (PPY) coated $ZnFe_2O_4$ double-shell hollow microspheres through a facile and efficient vapor-phase polymerization method. The thin PPY coating improves not only the electronic conductivity but also the structural integrity, and thus the cycling stability of the $ZnFe_2O_4$ hollow spheres. This chapter was published in *Small* (2016, 12 (27), 3732-3737).

Chapter 5 Nitrogen-doped mesoporous carbon microspheres by spray drying-vapour deposition for high-performance supercapacitor

This chapter presents a spray drying-vapour deposition method to synthesize nitrogen-doped mesoporous carbon microspheres for EDLCs applications. The nitrogen-doped mesoporous carbon microspheres possess an increased apparent density compared to carbons synthesized using air-drying and freeze-drying methods. The resultant nitrogen-doped mesoporous carbon microspheres show mesopore-dominate high surface area with thin carbon wall thickness and considerable nitrogen doping, exhibiting a superior gravimetric/volumetric capacitance.

Chapter 6 Synthesis of N-doped three-dimensionally ordered macroporous carbon microspheres

Apart from mesoporous carbon microspheres, spray drying-vapour deposition method was also applied in the synthesis of nitrogen-doped three-dimensionally carbon microspheres. A hexagonal-close-packed periodicity of macropores is achieved through the spray drying method. Vapour deposition of polypyrrole followed by carbonization and etching is beneficial for the generation of carbon network with a wall thickness of 3.5 nm. The resultant 3DOM carbon microspheres possess a hexagonal close packing structure with high surface area of 892 m^2/g, ultrahigh pore volume of 7.5 cm^3/g and high nitrogen doping of 8 At%.

Chapter 7 Conclusions and outlook

This chapter presents the conclusions of the work in this thesis and outlook for the future work.

1.4 References

[1]   Rahman, M. A.; Wong,Y. C.; Song, G.; Wen C., *J. Porous Mater.* **2015**, *22*, 1313.

[2]   Poizot, P.; Laruelle, S.; Grugeon, S.; Dupont, L.; Tarascon, J-M., *Nature* **2000,** *407*, 496.

[3]   Taberna, P.L.; Mitra, S.; Poizot, P.; Simon, P; Tarascon, J-M., *Nat. Mater.* **2006,** *5*, 567.

[4]   Jiang, J.; Li, Y.; Liu, J.; Huang, X.; Yuan, C.; Lou X.W., *Adv. Mater.* **2012,** *24*, 5166.

[5]   Choi, S. H.; Kang, Y. C., *Chem.-Eur. J.* **2014**, *20*, 5835.

[6]   Wang, Z.; Zhou, L.; Lou, X. W., *Adv. Mater.* **2012**, *24*, 1903.

[7]   Liang, C.; Li, Z.; Dai, S., *Angew. Chem. Int. Ed.* **2008,** *47*, 3696.

[8]   Yan, Y.; Zhang, F.; Meng, Y.; Tu, B.; Zhao D., *Chem. Comm.* **2007**, 2867.

[9]   Caruso, F.; Caruso, R. A.; Mohwald, H., *Science* **1998,** 282, 1111.

[10]   Han, S.; Hyeon, T.; *Chem. Comm.* **1999**, 1955.

[11]   Wang, Q.; Yan, J.; Fan, Z., *Energy Environ. Sci.* **2016**, *9*, 729.

[12]   Zhou, L.; Xu, H.; Zhang, H.; Yang, J.; Hartono, S. B.; Qian, K.; Zou, J.; Yu, C., *Chem. Comm.* **2013***, 49*, 8695.

[13]   Tan, A.; Martin, A.; Nguyen, T.-H.; Boyd, B. J.; Prestidge, C. A., *Angew. Chem. Int. Ed.* **2012***, 51*, 5475.

[14]   Lin, T.; Chen, I.-W.; Liu, F.; Yang, C.; Bi, H.; Xu, F.; Huang F., *Science* **2015**, *350*, 1508.

[15]   Han, F.; Li, D.; Li, W.-C.; Lei, C.; Sun, Q.; Lu A.-H., *Adv. Funct. Mater.* **2013**, *23*, 1692.

Chapter 2

Literature review

This chapter presents an overview of energy storage techniques, including lithium-ion batteries, supercapacitors and other techniques. In this review, the synthetic methodologies of hollow-structured transition metal oxides are classified and the application of hollow-structured transition metal oxide in lithium-ion batteries is summarised. The synthesis of highly porous carbon materials and their application in supercapacitors are also reviewed in this chapter.

2.1 Overview of energy storage techniques

Electrical energy becomes the primary form of consumed energy since the invention of generators in the 1870s. Electricity is dispensable in our daily lives and easily generated from diverse powers (e.g. fuel-burning, solar power, wind power). The storage techniques are essential for the efficient, versatile, and environmentally friendly uses of electricity. Among the various storage technologies, electrochemical energy storage shows advantages of high efficiency, flexibility, and versatility. Batteries and supercapacitors, as two typical kinds of electrochemical storage techniques, are in high demand for the portable electronic devices and electric vehicles.

In this part, the backgrounds and working principles of LIBs and supercapacitors are introduced. Then the expectations of electrode materials for LIBs and supercapacitors are summarized. Other electrochemical energy storage techniques like Li-S batteries, Al-ion batteries are also briefly mentioned in this section.

2.1.1 Lithium-ion batteries (LIBs)

Lithium-ion battery, also called rocking-chair battery, was discovered to circumvent the safety issues caused by the used of lithium metal at the end of the 1980s. In principle, the dendrite problem was solved by changing the presence of lithium in ionic instead of the metallic state. As lithium is the lightest metal (equivalent weight M=6.94 g/mol, specific gravity ρ=0.53 g/cm^3) and the most electropositive metal (-3.04 V versus standard hydrogen electrode), LIBs show higher energy density compared to other battery techniques.[1] Due to their high energy density and design flexibility, LIBs attract tremendous attention at both fundamental and applied levels.
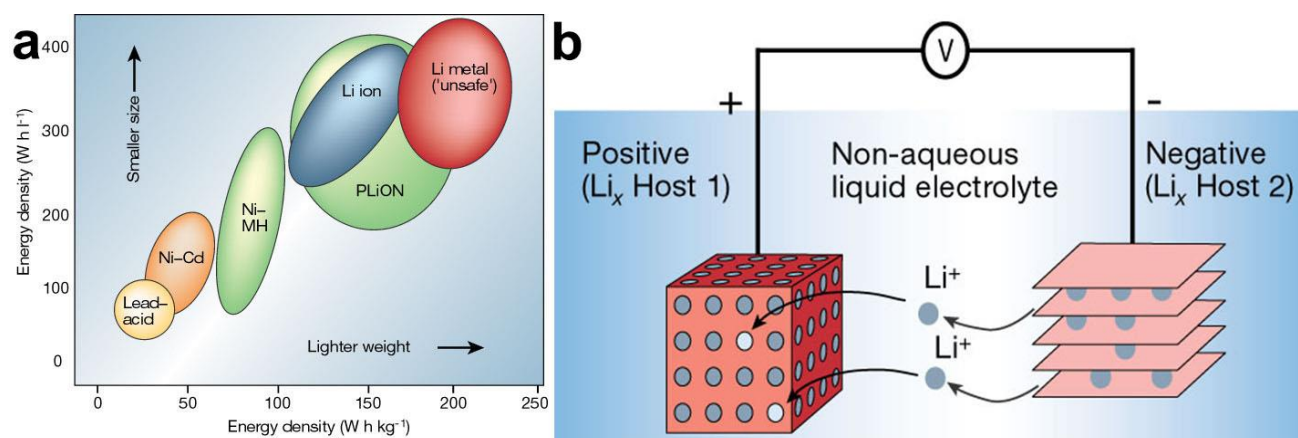
Figure 2.1 a) Comparison of the different battery technologies in terms of volumetric and gravimetric energy density, b) schematic representation and operating principles of the chargeable Li-ion battery. Reprinted with permission from Ref 1. Copyright 2001 Nature Publishing Group.

LIBs is a transducer for two-way conversion between electrical energy and chemical energy. In general, the rechargeable LIBs comprise a negative electrode (anode), a positive electrode (cathode),

and a non-aqueous liquid electrolyte. During charging, lithium ions are deintercalated from layers in the cathode, pass through the electrolyte and then intercalated among the layers of the anode, as shown in Figure 2.1b.[2] The electrolyte provides the transport for lithium ions, while the electrons pass through the external circuit to balance the charge. This process is reversed in discharging.

As noted above, the electrode materials must be good ionic/electronic conductor to allow the flow of lithium ions and electrons.[3] thus makes the cathode and anode materials key components for rechargeable LIBs. An adequate material as a cathode for LIBs requires a readily reducible/oxidizable ion for reaction, a stable structure for intercalation-type reaction, and a rapid, reversible manner during charge-discharge.[4] It is also beneficial for the cathode materials to be low cost and environmentally benign.[5] Moreover, the developments of cathodes focus on materials with high capacity and high voltage (around 4 V), which leads to a high-energy storage.[6]

Besides cathode materials, anode materials for LIBs have been extensively investigated in recent years. The initial anode, metal lithium, has been replaced because of safety considerations.[7] Graphite is used as the current commercialised anode, but the low theoretical capacity (372 mA h/g) of graphite highly restricts its application. Other materials with higher theoretical capacities are considered as promising candidates for anode materials, like carbonaceous materials, tin-based oxides, alloy anodes (Si, Sn, Ge, Sb) and transition metal oxides.[8] Among aforementioned anode materials, alloy anodes and transition metal oxides attract tremendous attentions due to their high capacities. However, the mechanism of lithium storage of these materials is conversion reaction, with inevitable multiple crystallographic phase transitions during lithiation and delithiation.[9] Thus, large volume changes are experienced during charge-discharge, which shortens the cycling life and contributes to cell failure. Hollow-structured metal oxides have been demonstrated to overcome the bottlenecks and provide high specific capacity, improved cycling capability, and superior rate performance.[10] The mechanism and research activities of hollow-structured transition metal oxides are specified in section 2.2.

2.1.2 Supercapacitors

As an alternative to batteries, electrochemical capacitors were firstly reported in U.S. patent by Becker in 1957. It is shown in Ragone plot (Figure 2.2a) that the electrochemical capacitors play an essential role in bridging the gap between dielectric capacitors and batteries. Comparing to batteries, the energy densities of electrochemical capacitors is generally lower (less than 5 Wh/kg), but the power densities of electrochemical capacitors are much improved.[11] Currently, electrochemical capacitors have been applied in portable equipment to supply complementing power[12] and in electric vehicles as the additional function for acceleration or brake energy.[13]
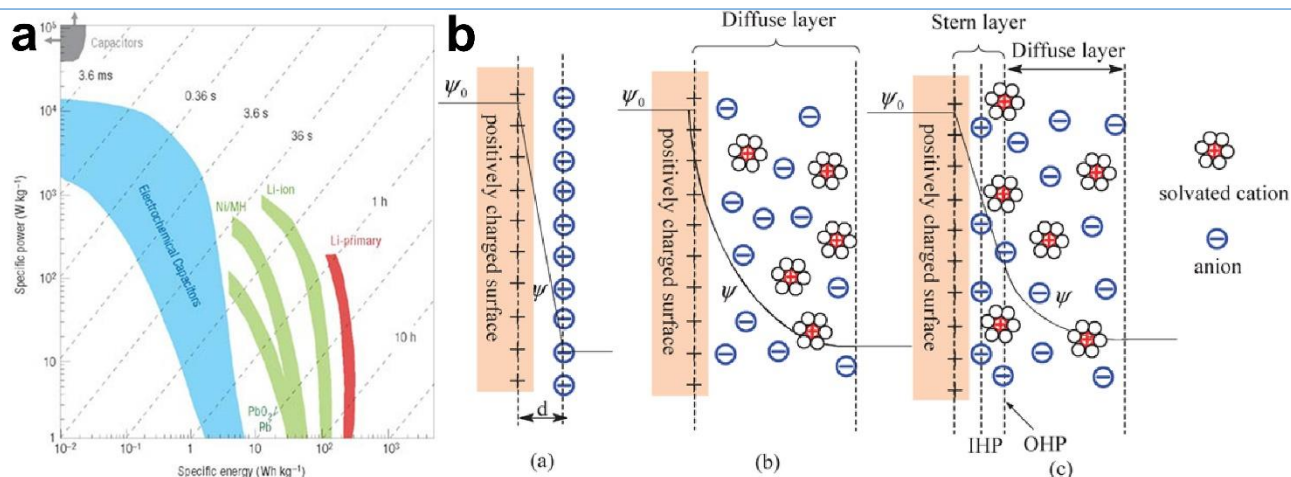
Figure 2.2 a) Specific power against specific energy for various electrical energy storage devices, b) Models of the electrical double layer at a positively charged surface. Reprinted with permission from Ref 11 (Copyright 2001 Nature Publishing Group) and Ref 15 (Copyright 2009 The Royal Society of Chemistry).

Electrochemical capacitors are divided into electrical double-layer capacitors (EDLCs) and pseudocapacitors according to working principles.[14] In EDLCs, the charge was stored by electrostatic adsorption of the ions at the interface between electrode and electrolyte.[15] On the contrary, the energy was stored by fast faradic reactions at the interface between the electrode and electrolyte in pseudocapacitors.[16] We mainly focus on EDLCs and its electrode materials in this thesis.

The adsorption model of EDLCs was first hypothesized according to a conventional two-plate capacitor (Helmholtz model, (a) in Figure 2.2b).[17] However, the Helmholtz model was too over-simplified to consider the factors like the ion diffusion in the electrolyte, the ion adsorption onto the surface of the electrode, and the interactions between electrode and electrolyte. Later, the Helmholtz model was modified to the Gouy-Chapman model ((b) in Figure 2.2b).[18] In this model, a continuous distribution of cation and anion ions in the electrolyte was involved,[19] thus the capacitance of EDLCs was overestimated. By combining the Helmholtz model with the Gouy-Chapman model, a further modified Stern model was proposed ((c) in Figure 2.2b).[15] In the Stern model, the total capacitance of EDLC was the sum of capacitance from the compact layer (Stern layer) and the diffusion layer.

Taking the advantage of aforementioned electrostatic charge adsorption on the interface between electrode and electrolyte, EDLCs are capable of fast energy delivery, which results in excellent power density. Besides, the electrode material of EDLCs shows high stability due to the absence of faradic reactions. Thus, EDLCs could sustain for millions of charge-discharge cycles with high coulombic efficiency.

According to the parallel-plate model, the capacitance of EDLCs can be calculated using the following equation:[20]

$$C = \frac{\varepsilon_r \varepsilon_o}{d} A \qquad\qquad \text{(equation 2.1)}$$

Where ε_r is the electrolyte dielectric constant, ε_o is the vacuum dielectric constant, A stands for the specific surface area of the electrode, and d stands for the effective thickness of the double layer.

It is shown from equation 2.1 that there is a linear relationship between the capacitance of EDLCs and the specific surface area of the electrode material. Porous carbon materials have attracted great attentions as an electrode material for EDLCs because of their high conductivity, high chemical stability, and the most important, high specific surface area with tunable pore size.[21] Numerous literature has been reported on the variable synthesis method of porous carbon for EDLCs.[22] In addition, the influence of pore size distribution[23] and heteroatoms doping[24] of porous carbon on their capacitive behaviours was also been extensively investigated. These factors of porous carbon are specified for discussion in section 2.3.

2.1.3 Other electrochemical energy storage techniques

Except for LIBs and electrochemical capacitors, Li-S batteries is another promising candidate in rechargeable lithium battery systems.[6] Li foil is applied as the anode in Li-S battery, while the cathode is comprised of carbon powder and elemental sulfur. Compared with conventional LIBs, Li-S battery is capable of delivering higher theoretical gravimetric capacity as well as theoretical volumetric capacity.[25] However, the main bottleneck of Li-S battery is the "shuttle-effect" which prevents the possibility of extracting the full capacity of the sulfur cathode.[26] To alleviate the shuttle effect of the sulfur cathode, smaller sulfur molecules (S_2-S_4) were applied during the impregnation process.[27] Dithiothreitol was used as a polysulfide-scission reagent to suppress the shuttle effect of Li-S battery.[28] Titanium monoxide hollow nanospheres were also introduced for the adsorption of lithium polysulfides.[29] In addition, selenium was introduced as the second active material to form selenium-sulfur solid solutions (SeS_2), thus alleviate the shuttle effect of the sulfur and improved the cycling stability of the batteries.[30]

Porous carbon is the most frequently used material as the host for sulfur loading and increase the conductivity of the cathode composite at the same time. Tremendous progress has been made in modifying sulfur-carbon nanohybrids with porous carbon materials with various morphology and structure. One-dimensional carbon structures like indented hierarchically porous carbon spheres,[31] interconnected mesoporous hollow carbon nanospheres,[32] and N-doped hollow carbon bowls[33] are applied to Li-S battery. Two-dimensional bubble-like interconnected carbon fabric[34] and three-dimensional structures like graphitic carbon,[35] carbon nanotube foam[36] and pomegranate-like carbon cluster[26] are also applied in this field. The porous carbon frameworks not only act as hosts

for sulfur loading but also provide mechanical stability to the deposited sulfur for long-lasting cycling life.

The high price of the lithium salt and the requirement of a strictly dry environment during cell assembly are the main issues of LIBs. Thus the post-lithium ion batteries such as Na-ion batteries, Mg-ion batteries, and Al-batteries are investigated.[37] Among these research activities, Al-ion batteries attract more attention due to the abundance (8 wt. % on earth), low atomic weight (26.98 g/mol), high theoretical electrochemical equivalent (2980 mA/g) and environmentally benign.[38] It is reported that fluorinated natural graphite,[39] three-dimensional graphitic foam,[40] and zeolite template carbon[41] were used as anode materials for Al-ion batteries. The advantages of porous carbon as anode material for Al-ion batteries is worth further studying.

2.2 Hollow-structured transition metal oxides

With the significant increase of global population, the energy crisis is considered as one of the biggest challenges today. The production and application of current energy storage systems are facing many drawbacks such as high cost, low efficiency, and environmental damages. To solves above problems, it is desirable to design and engineer materials with novel structures for sustainable energy.[42]

Transition metal oxides (TMOs) have great potential as anode material for LIBs.[43] The theoretical capacities of TMOs are around 1000 mA/g, which is two times higher than that of commercial graphite. However, the main bottleneck of the TMOs as anode materials in LIBs is the large volume variation during lithiation-delithiation. The large volume expansion easily causes the pulverization of the active material and the disintegration of the electrode, leading to rapid decay of capacity. Besides, the repetitive contraction and volume variation may break the solid electrolyte interphase layer. Thus, electrolyte and lithium ions are consumed again to form a new interphase on the surface of the re-exposed electrode to the electrolyte. Besides the volume expansion, the poor electrical conductivity also limits the rate capacity of the TMOs, which is another drawback in the practical application of TMOs anode materials.

Hollow-structured materials have been recognized as a promising strategy to address the aforementioned issues.[44] Firstly, the interior voids in hollow structures are capable of accommodating the volume expansion and alleviating the structural strain during charge-discharge.[45] Secondly, the hollow structure is usually composed of thin shells, which reduces the transport pathway for both electron and ions.[46] Thirdly, the hollow structure is advantageous for its high surface to volume ratio.[47] The high specific surface area ensures a high contact area between electrode and electrolyte, facilitating the electrochemical reaction. However, only single-shelled hollow structures are available for most of the energy storage applications.[48] It is desirable to

synthesize complex hollow structures with multiple shells. Further tune the properties of materials by manipulating the hollow structure is expected as well.

2.2.1 Synthetic methodologies for hollow-structured transition metal oxides

The methodologies for the synthesis of hollow-structured TMOs have usually classified into three categories: hard templating methods, soft templating methods, and template-free methods. The details of synthesize process for each method are specified below.

(1) Hard templating methods

The hard templating method is using rigid materials as templates for the fabrication of hollow-structured materials.[49] It is considered as the best path for the synthesis of the multi-shelled hollow structures due to the advantages of controlled morphology, such as shape, size, and structure. Generally, the hard templating technique involves coating precursor materials onto the surface of a solid sphere to form a core-shell complex. By subsequently removing the solid template particle, a single-shell hollow structure is generated, as shown in Figure 2.3a. In principle, the hard templating method is possible to extend to the synthesis of the multi-shelled hollow structure. For example, partially remove the solid template materials after forming the target shell, the remaining solid materials can be used as a template for the creation of another shell, resulting in a double-shelled hollow structure (Figure 2.3b). Similarly, this procedure can be extended to the synthesis of the multi-shelled hollow structure through a series of sequential solid-template processes (Figure 2.3c). If a single-shelled hollow sphere is applied as the template rather than a solid core, the precursors are coated both inside and outside. Then a double-shelled hollow structure is generated after the removal of the hollow template, as shown in Figure 2.3d. Similarly, the quadruple-shelled hollow structures can be created by using double-shelled hollow spheres as a template (Figure 2.3e). Moreover, combining the solid core with a hollow sphere to form a core-shell hollow template, multi-shelled hollow structures can be generated as well (Figure 2.3f). With this concept, more complex multi-shelled hollow structures can be obtained using templates with specific geometries.
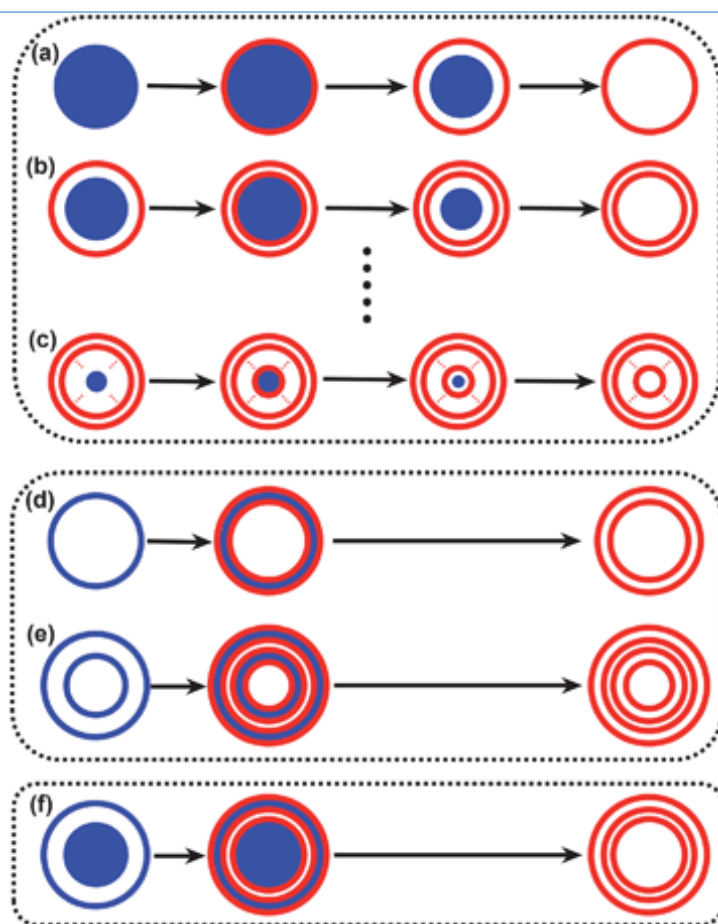
Figure 2.3 Schematic illustration of the formation of the hollow structure via (a), (b), (c) solid templating; (d), (e) hollow templating; and (f) combined solid and hollow templating method. Reprinted with permission from Ref 44. Copyright 2012 The Royal Society of Chemistry.

One typical example using hard templating method for the synthesis of the multi-shelled hollow structure is the VOOH hollow spheres reported by Xie et al.[50] $V(OH)_2NH_2$ solid spheres were used as templates for the synthesis of VOOH hollow spheres via a programmed reaction temperature process. After the first outer shell was formed, the authors chose to decrease the reaction temperature to stop the hollowing process. The hollowing process was restarted again after a short pause to form the second shell. A multi-shelled hollow structure will be generated via a shell-in-shell process if repeat decrease and increase of the reaction temperature, as shown in Figure 2.4a-c-e-g. Qian et al. applied a similar method for the synthesis of double-shelled Mn_2O_3 hollow microspheres using $MnCO_3$ solid spheres as the precursor template.[51] Xie et al. report the synthesis of $LiMn_2O_4$ using double-shelled Mn_2O_3 hollow microspheres as intermediate.[52] Lou et al. reported the synthesis of double-shelled $Fe(OH)_x$ hollow nanoboxes using Cu_2O solid nanotubes as template and precursor,[53] extending the programmed reaction temperature process into the synthesis of nonspherical multi-shelled hollow structures.
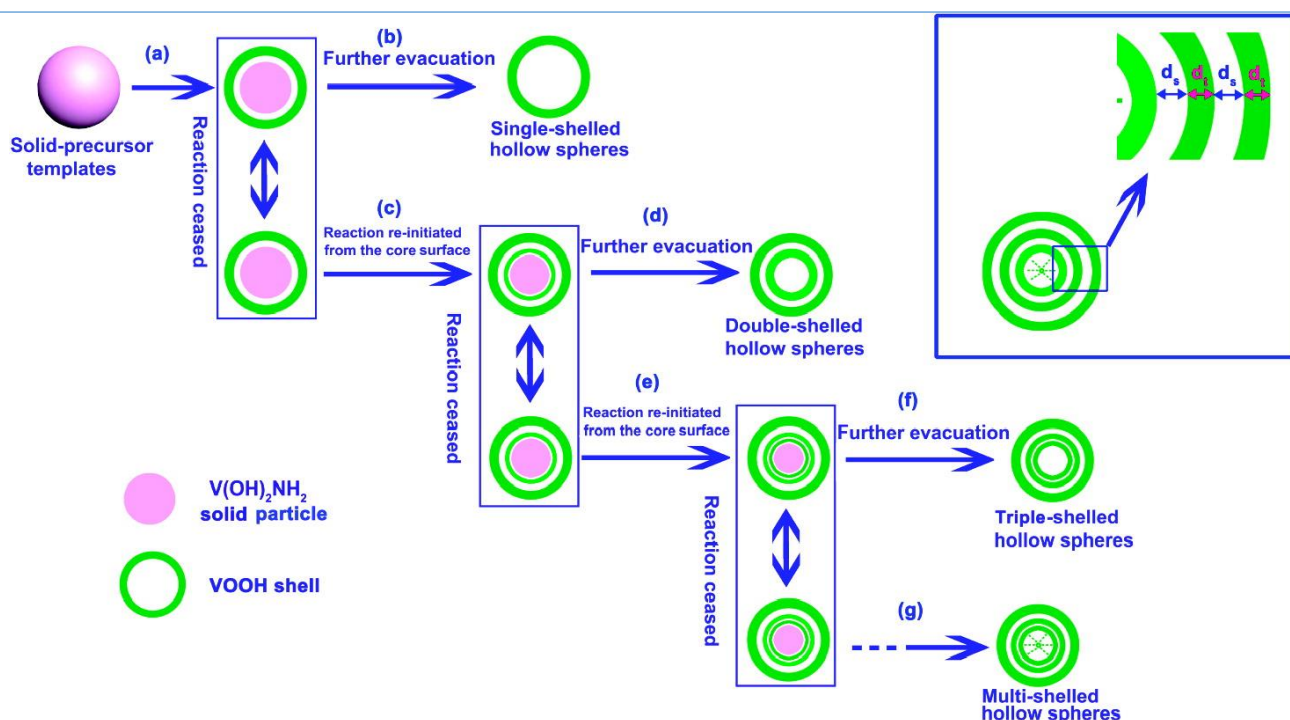
Figure 2.4 The schematic outline of the transformation of solid templates to single-shelled (a−b), double-shelled (a−c−d), triple-shelled (a−c−e−f), and multi-shelled (a−c−e−g) hollow spheres. Inset is the typical multi-shelled hollow spheres, where d_t is the shell thickness size and d_s is the neighboring shell-to-shell distance. Reprinted with permission from Ref 50. Copyright 2009 American Chemical Society.

The programmed reaction temperature process is a facile method for the production of hollow structures. However, this method requires the solid cores act as both the template and precursors, which is not universally applicable for some materials. Carbonaceous microsphere templating process, firstly pioneered by Li[54] and Tomas,[55] was introduced in the synthesis of hollow TMOs spheres. Compared to programmed reaction temperature process, carbonaceous microsphere templating process is more generally applicable since most metal ions can be absorbed by carbonaceous microspheres through electrostatic attraction.[56] One concern is the metal ions were mainly adsorbed on the surface/exterior of the carbonaceous microspheres, results in single-shelled hollow TMOs.[57] In order to improve the utilization of the solid carbonaceous microspheres, Wang et al. reported a general sequential templating approach for the synthesis of the multi-shelled hollow TMOs microspheres, as shown in Figure 2.5.[58] The authors demonstrated that metal ions can penetrate into the interior of the carbonaceous templates when using a high concentration of metal salts for impregnation.[59] During calcination, the metal ions adsorbed on the exterior formed an outer shell, and the interior metal ions created more shells. Thus, carbonaceous microspheres act as sequential and multiple solid templates in the fabrication of multi-shelled hollow TMOs spheres. A series of multi-shelled hollow TMOs microspheres have been synthesized using this method, such as α-Fe$_2$O$_3$, NiO,[60] Mn-doped ZnO,[61] Co$_3$O$_4$, CuO and ZnFe$_2$O$_4$.[58]
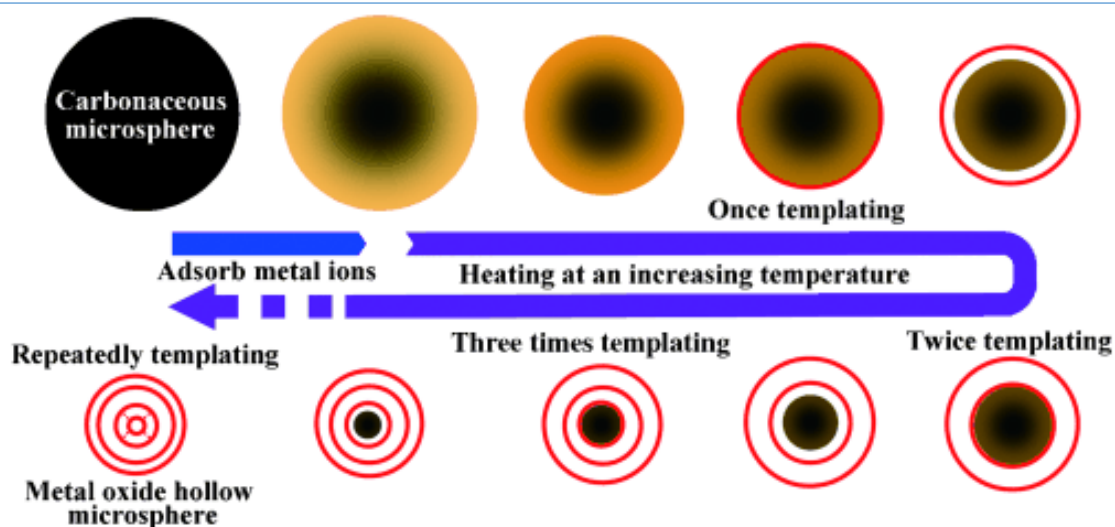
Figure 2.5 Illustration of the sequential templating approach to multiple-shell hollow metal oxide microsphere synthesis. Reprinted with permission from Ref 58. Copyright 2011 Wiley.

Beside carbonaceous microspheres, coordination polymer microspheres are also used as the template to generate multi-shelled hollow TMOs. Cho et al. reported the synthesis of multi-shelled hollow ZnO and Co_3O_4 microspheres using coordination polymer microspheres as the template. Moreover, the composition of the multi-shelled hollow TMOs microspheres is tunable after combining cation exchange to introduce second metal ions before calcination (Figure 2.6).[62] Zeng et al. reported the synthesis of multi-shelled TiO_2 hollow spheres using polystyrene-divinylbenzene spheres as the template.[63] Similarly, Yu et al. reported the fabrication of multi-shelled hollow TMOs microspheres such as α-Fe_2O_3 and $ZnFe_2O_4$ using spray drying method to form citrate-sucrose template.[64] Moreover, non-spherical multi-shelled hollow structures could be achieved if extending the strategy to non-spherical templates.[65]

The choice of template is not limited to solid coordination polymers, hollow coordination polymer is available to be used as a template for the synthesis of multi-shelled hollow TMOs spheres as well. Xu et al. reported the synthesis of double-shelled hollow microspheres of TiO_2[66] and Fe_3O_4[67] using sulfonated polystyrene hollow spheres as the template. The inter-shell distance of the as-synthesized TMOs can be tuned by varying the thickness of the hollow templates. One key for hollow polymer templates is that they possess transverse channels, allowing metal salt precursors to reaching the inner surface of the template. Thus, it may face difficulty to spread the availability of hollow template in the fabrication of multi-shelled hollow TMOs.
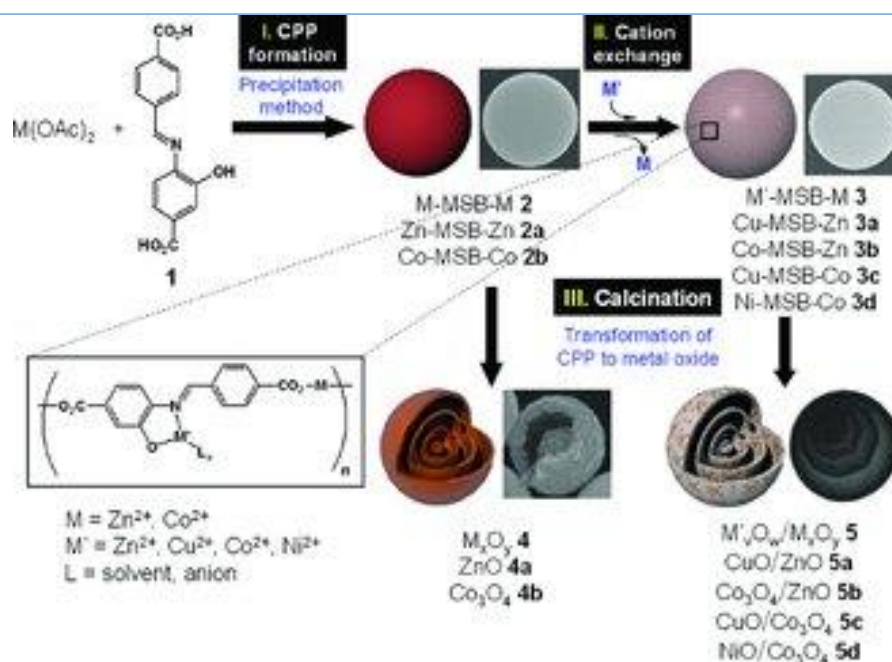
Figure 2.6 Preparation of multi ball-in-ball hybrid metal oxides. Reprinted with permission from Ref 62. Copyright 2011 Wiley.

(2) Soft templating methods

The synthesis of the hollow structures using soft templating method typically involves the formation of flexible structures like supramolecular micelles,[68] emulsion droplets,[69] and polymer aggregates.[70] However, it is still a great challenge to develop a simple method for the synthesis of multi-shelled hollow structures using soft templating route due to the sensitivity to parameters such as pH value, solvent, ionic strength, and temperature. Wang et al. reported multi-shelled Cu_2O hollow spheres using cetyltrimethylammonium bromide as the template in aqueous solution.[71] Xie et al. reported the fabrication of the double-shelled ferrihydrite hollow spheres through a twice-gas-bubble template method.[72] The aforementioned approaches have demonstrated the success of synthesizing multi-shelled hollow TMOs via soft templating method, but generally apply this soft templating method for the synthesis of multi-shelled hollow TMOs is still worth studying.

(3) Template-free methods

Although template-assisted methods are relatively versatile and effective for the fabrication of multi-shelled hollow TMOs, the bottleneck of high cost[73] and complex synthetic procedures[74] highly restrict the application of the template-assisted method. The template-free method is considered as the simplest approach to synthesize multi-shelled hollow TMOs. Yet, the generalized and scalable production via template-free method is the least unlikely due to the high demand of target material for self-assembly.

2.2.2 Application of hollow-structured transition metal oxides in lithium-ion batteries

LIBs are widely used in portable electronics and considered as one of the most promising energy storage techniques for electric and hybrid vehicles.[75] However, it is still required to develop mew electrode materials to meet the increasing demand for batteries with higher energy density and performance.[76] Hollow structured materials have received most attention among the promising candidates because of their high specific surface area and short lithium transport length. The short lithium path length is beneficial for the reaction kinetics at the electrode surface, while hollow void is capable of buffering the volume variation during charge-discharge.[44] For the aforementioned reasons, multi-shelled hollow structures will provide greater performance improvements.

Tremendous efforts have been made to improve the performance of LIBs using multi-shelled hollow TMOs as anodes. Lou et al. reported the double-shelled SnO_2 hollow spheres via shell-by-shell hydrothermal deposition using silica nanosphere template.[77] Compared to single-shelled counterparts, the double-shelled hollow structures enhance the gravimetric energy densities as well as the volumetric energy densities. Xue et al. reported the double-shelled SnO_2-V_2O_5 hollow nanospheres using a combination of outward and inward Ostwald ripening.[78] The tiny SnO_2 nanocrystals were uniformly distributed in the V_2O_5 shells to improve the reversible discharge capacity and cycling stability. Triple-shelled SnO_2 hollow microspheres were reported by Yang et al. using chemically induced self-assembly for high capacity retention anode material.[79] Wang et al. reported the synthesis of single-, double-, and triple-shelled Co_3O_4 hollow structures using the soft template method.[80] Kang et al. reported a spray drying method in the synthesis of $ZnFe_2O_4$ yolk-shell structures with superior electrochemical performance.[81]

All above reports show the suitability of multi-shelled hollow TMOs as anode materials for LIBs application. However, the cycling stability of the as-synthesized multi-shelled hollow TMOs remains unsatisfactory due to the insufficient structural stability and conductivity. These issues can be addressed simultaneously by applying the second component with high electrical conductivity, such as carbon. Take $ZnFe_2O_4$ as an example, $ZnFe_2O_4$/C hollow composites have been successfully synthesized by solvothermal synthesis[82] and thermal decomposition of metal organic frameworks.[83] Yet the synthesis of carbon-coated TMOs hollow structures usually requires high-temperature carbonization, thus TMOs tend to reduce by carbon and form residues. It is still worth studying the novel synthesis method with proper coating component for hollow TMOs structures to maintain the structural integrity and improve the electrical conductivity, especially for delicate multi-shelled hollow structures.

2.3 Porous carbon materials

2.3.1 Classification of porous carbon

Carbon and carbon-based materials have attracted intense interests as electrode materials for energy storage techniques due to their intrinsic advantages of high electrical conductivity, high chemical stability and low cost.[21] Creating porosity of the carbon materials is one of the straightforward strategies to increase the accessible area of the electrode with the electrolyte. According to the recommendation of the International Union of Pure and Applied Chemistry (IUPAC), pores can be classified as micropores, mesopores and macropores.[84] Microporous carbon materials contain pores that are predominately less than 2 nm; mesoporous carbon materials is consist of pores with sizes from 2 nm to 50 nm; whereas macroporous carbon materials contain pores larger than 50 nm. Recently, the development of energy storage techniques requests high demand on the precise control over the type of porosity present in the electrode materials.[85] It is noted that the calculation model of theoretical capacities for the electrode materials can be influenced by pore size distribution. Taking EDLCs as an example, the traditional parallel-plate capacitor model is applicable for macroporous carbon materials with pore size above 50 nm.[20] However, the influence of pore curvature should be considered when the pore size is less than 50 nm. Huang et al. reported the Heuristic model by taking pore curvatures into account, proposing the electric double-cylinder capacitor (EDCC) model for mesoporous carbon and the electric wire-in-cylinder capacitor (EWCC) model for microporous carbon, shown in Figure 2.7.
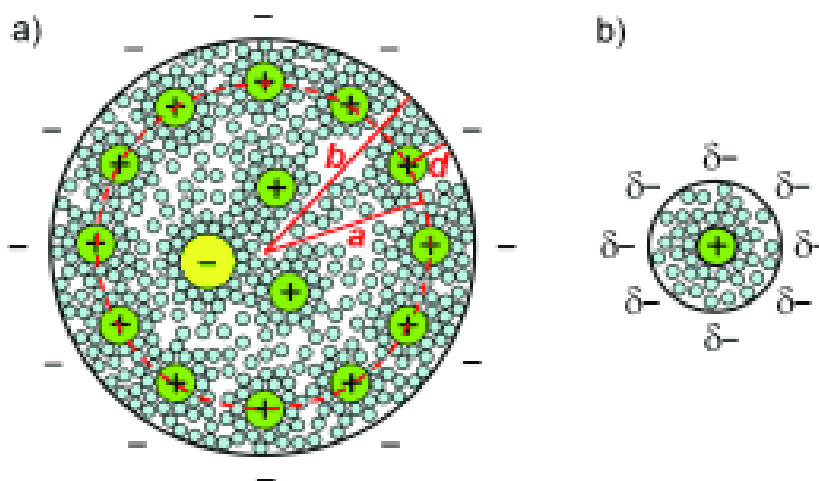
Figure 2.7 Schematic diagrams (top views) of a) a negatively charged mesopore with solvated cations approaching the pore wall to form an EDCC with radius b and a for the outer and inner cylinders, respectively, separated by a distance d, and b) a negatively charged micropore of radius b with solvated cations of radius a_0 lining up to form an EWCC. Reprinted with permission from Ref 20. Copyright 2008 Wiley.

The capacitance of EDCC and EWCC are calculated according to the following equations respectively:

$$C = \frac{\varepsilon_r \varepsilon_o}{b \ln[b/(b-d)]} A \qquad \text{(equation 2.2)}$$

$$C = \frac{\varepsilon_r \varepsilon_o}{b \ln(b/a_o)} A \qquad \text{(equation 2.3)}$$

Where b stands for the pore radius of the outer cylinders, a_o is the effective size of the counterions (radius of the inner cylinder), and d is the distance between outer and inner cylinders.

It is shown that the porosity and pore size distribution of have great influence on the capacity of the carbon materials. Therefore, the synthesis of porous carbon materials is summarized in the following section, classified according to pore size of the materials.

2.3.2 Synthetic methodologies for porous carbon materials

(1) Microporous carbon materials

Microporous carbon materials show great potential as absorbent and electrode material for energy storage due to their abundant micropores and high specific surface area. Activation is one of the conventional strategies to increase the specific surface area of microporous carbon materials through introducing a large amount of micropores. During the activation process, the activation agent contacts and etches the carbon walls at high temperature, leaving microporous fissures on the surface of carbon materials.[86] The commonly used activating agents are base (such as KOH, NaOH), $ZnCl_2$, H_3PO_4, CO_2 and steam. Among activating agents, base and acidic activating agents require an additional neutralization and washing to move the excess agents out of the pores of carbon. The inorganic salt $ZnCl_2$ also requires post-activation washing in acid to remove the residual. Steam is the most advantageous and environmentally benign of the activating agents as it requires no post-treatment.[87] The only concern for steam activation is the functional oxygen groups attached to the surface, which decreases the electrical conductivity of the carbon materials.

As a special form of activated carbon, molecular sieving carbons possess uniform micropores of several angstroms in diameter.[88] The representative synthetic method for the fabrication of molecular sieving carbons is the pyrolysis of carbon precursors.[89] The carbon precursors used during pyrolysis varies from pitch, phenol, formaldehyde,[89] polystyrene based resins[90] and other polymeric resins.[91] The synthesized molecular sieving carbons and carbon membranes possess disordered micropores, which shows great potential for gas separation.

In order to make microporous carbon materials with uniform pores and ordered regular pore arrays, rigid inorganic templates such as zeolites[92] and metal carbides[93] are required. Zeolites are aluminosilicate materials with ordered and uniform sub-nanometer sized pores. Because zeolites

possess uniform walls with a thickness less than 1 nm, zeolites have been applied as inorganic templates for the synthesis of microporous carbon with uniform pore size and periodic structures.[94] The zeolite template carbons are synthesized by firstly filling zeolite Y or zeolite X13 with carbon sources, followed by carbonization and removal of the zeolite template. Poly(acrylonitrile),[92] poly(furfuryl alcohol),[94] phenol-formaldehyde[95] and were employed as the carbon precursor during synthesis. As for carbide derived carbons which use SiC or TiC as templates, the synthetic process starts from high-temperature chlorination of silicon and titanium carbides, followed by an additional carbonization.[96] By precisely selecting the template carbide material, the chlorination and the carbonization temperatures, the pore size of the resultant carbide derived carbons can be tuned from 0.6 to 1.1 nm.[97]

(2) Mesoporous carbon materials

Mesoporous carbon materials have been widely investigated in energy storage application due to their outstanding properties such as high surface area, high pore volume, controllable morphologies, tunable pore size, and low cost.[98] The synthesis of mesoporous carbon materials with designed morphology and controllable structural parameter is of importance in both fundamental research and practical application. Thus, the synthetic methodologies of fabricating mesoporous carbon materials are summarized and classified as follows.

a. Hard-templating method

Hard-templating method, also called nanocasting, is one of the straightforward strategies for the synthesis of mesoporous carbon materials. The synthesis using hard-templating strategy usually involves the infiltration of carbon precursors into the micropores or mesopores of the porous template, followed by carbonization of the carbon precursors and the selective removal of the template using etchants like HF or NaOH. One typical hard-templating synthesis is the fabrication of CMK-3 using SBA-15 silica as a template, as shown in Figure 2.8.[99] Sucrose is used as carbon precursor to infiltrate into the channel of SBA-15 during hydrothermal treatment. The sucrose adsorbed is gradually decomposed and polymerized to form continuous frameworks inside the mesopores of SBA-15. Then the synthesized SBA-15/sucrose composite are carbonized to SBA-15/carbon composite under an inert atmosphere at elevated temperature. Since the carbon networks are continuous and interlinked, the mesoporous structure is well duplicated after etching the silica template. Besides of 2D-hexagonal templates, 3D-cubic silica like KIT-6 is also applied as a template for the synthesis of carbon replica (like CMK-8).[100] Moreover, a wide variety of non-ordered templates like activated carbons, silica nanospheres[101] and silica monoliths[102] may be used as a template for hard-template synthesis as well, exhibiting the generally applicable of the hard-templating method.
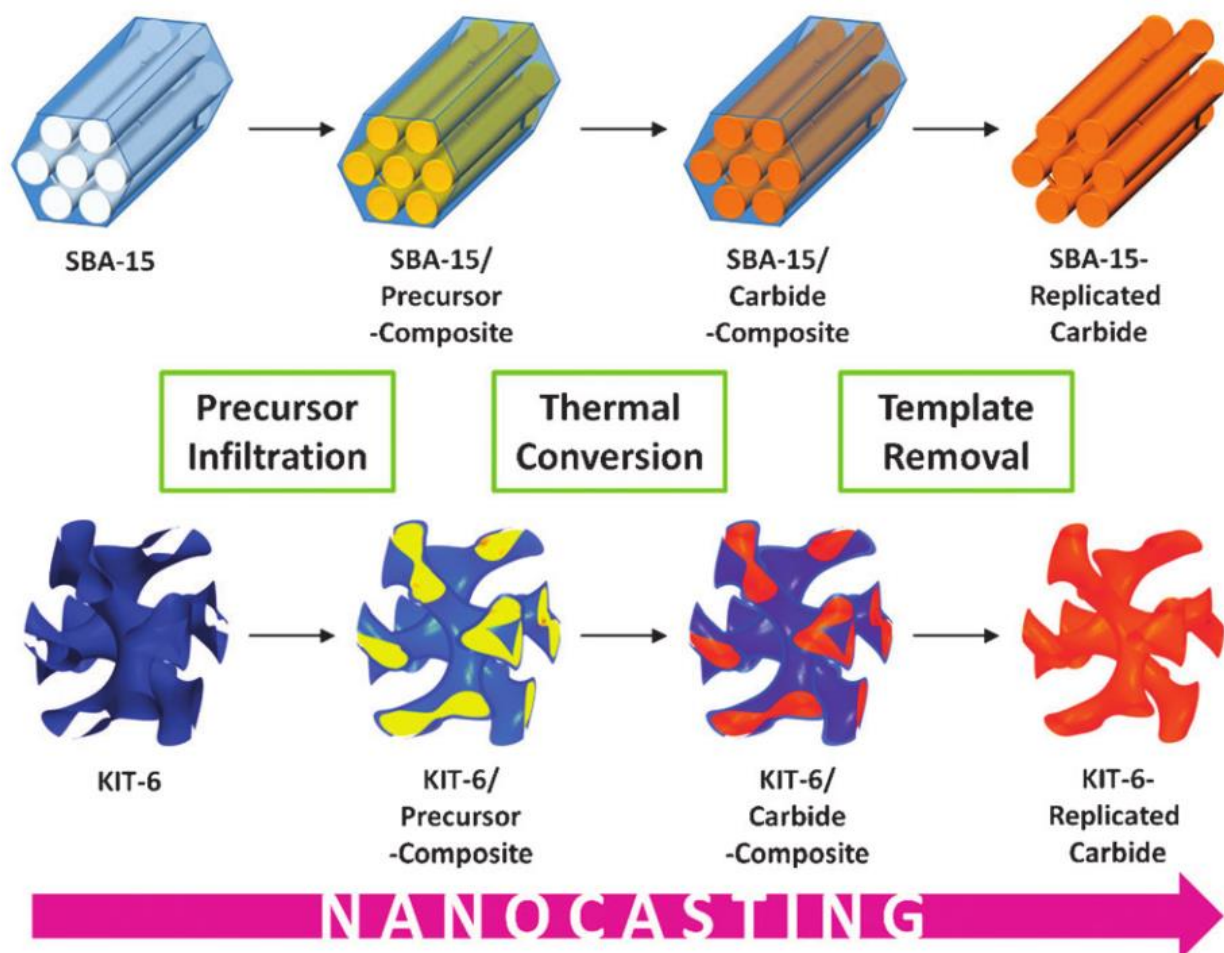
Figure 2.8 Hard templating approaches (nanocasting) exemplified for hexagonal and cubic silica templates. Reprinted with permission from Ref 99. Copyright 2012 The Royal Society of Chemistry.

Similar to bulk mesoporous carbon materials, mesoporous carbon nanospheres[103] and mesoporous carbon microspheres[104] can also synthesize via hard-template method using mesoporous silica spheres as the templates. Kim and co-authors first reported an ordered mesoporous carbon nanospheres using MCM-48 as hard template and furfuryl alcohol as carbon precursors.[105] The typical synthetic process starts from the preparation of mesoporous silica spheres as hard templates, followed by infiltration of carbon precursors into the mesopores of silica and/or the voids among mesoporous silica template. The resultant mesoporous carbon nanospheres/microspheres were obtained after high-temperature carbonization and selective removal of the silica template. This hard-templating strategy is easily extended to the synthesis of hollow structured nanospheres using silica Stöber spheres as the templates as well.[106] In this context, chemical vapour deposition[107] and sol-gel strategy[108] have been widely investigated to replace the conventional infiltration process.

Although the hard-templating strategy is straightforward, there are still limitations for the large-scale fabrication of mesoporous carbon materials. The reasons focus on the volume shrinkage of carbon precursors, the volatility of precursor or intermediates, and the difficulty of preserving the

ordering of template during thermal treatments. In additions, melt infiltration or dissolution in solvents is required in order to complete infiltrate template with solid precursors. And the structural parameters of the resultant carbon replica are highly limited to the parent materials. Therefore, the synthesis of mesoporous carbon material using hard-templating method for wide applications should overcome aforementioned drawbacks.

b. Soft-templating method

Differ from hard-templating routes described above, soft-templating approaches usually involves the precipitation and self-assembly of structure directing agents and carbon precursors. Firstly, the assembly is caused by the interplay of the attractive, non-covalent and repulsive force among the structure directing agent molecules. Then the self-assembled structures are used as templates for the construction of the desired materials through polymerization of the carbon precursors (shown in Figure 2.9). These structure directing agents used during soft-templating method are mainly amphiphilic molecules like block copolymers (e.g. P123, F127 and F108).
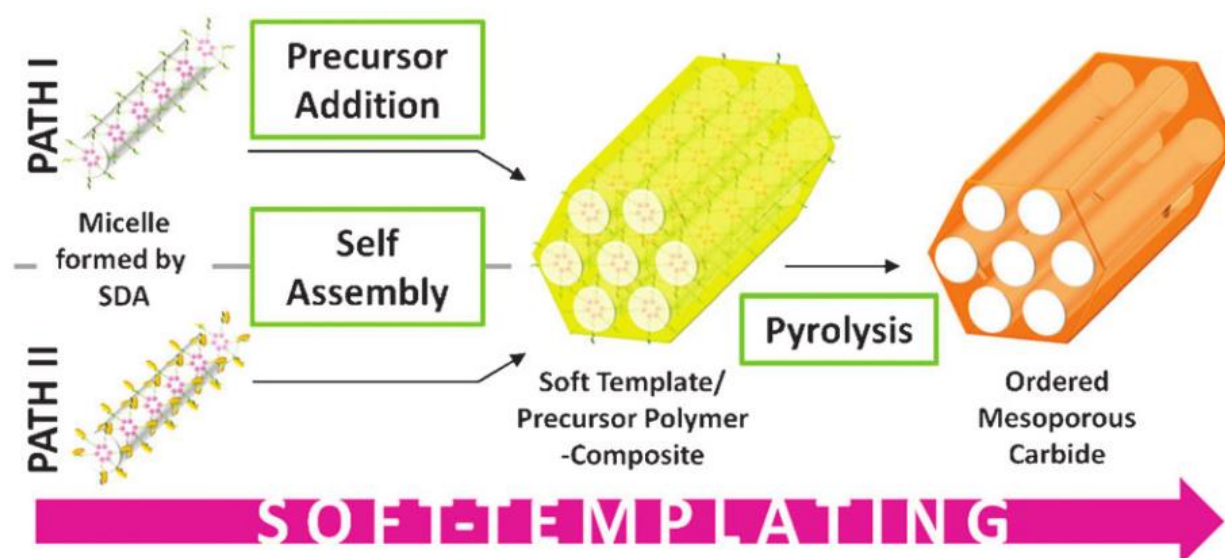
Figure 2.9 Ordered mesoporous carbides synthesized by soft templating approaches. Reprinted with permission from Ref 99. Copyright 2012 The Royal Society of Chemistry.

Over the past decades, the soft-templating method has shown great potential in the fabrication of mesoporous carbon materials. Dai et al. first reported the synthesis of highly ordered mesoporous carbon films via a stepwise assembly approach, using polystyrene-blockpoly(4-vinylpyridine) (PS-P4VP) as the structure directing agents and resorcinol-formaldehyde as the carbon precursor.[109] The soft-templating approach is further subdivided into aqueous solution synthesis and evaporation induced self-assemblies. Aqueous solution synthesis is widely applied in the fabrication of mesoporous carbon materials. The synthesis of mesoporous carbon materials with ordered structures like 2-dimentional hexagonal structure (*p6mm*), 3-dimentional bicontinuous cubic

structure (*Ia*3*d*),[110] and body-centered cubic structure (Im3m)[111] have been reported, using an aqueous pathway with P123 or F127 as the template. In the other hand, evaporation induced self-assembly is a liquid-deposition coating technique for preparing mesoporous carbon materials, especially ordered mesoporous carbon.[21] Zhao et al. reported the synthesis of highly ordered mesoporous carbon materials via evaporation induced self-assembly strategy.[112] As shown in Figure 2.10, the low-molecular-weight and water-soluble phenolic resins (resols) were mixed with the Pluronic PEO-PPO-PEO in ethanol. The homogeneous solution was poured into dishes for solvent evaporation. It induces the organic-organic self-assembly of resols with block copolymers by hydrogen bonds to form the ordered mesoporous structures. Besides the carbon precursor mentioned above, phloroglucinol-formaldehyde,[113] resorcinol-formaldehyde,[114] or phloroglucinol-glyoxal[115] are polymerized in the presence of Pluronic triblock copolymers to synthesize mesoporous carbon.
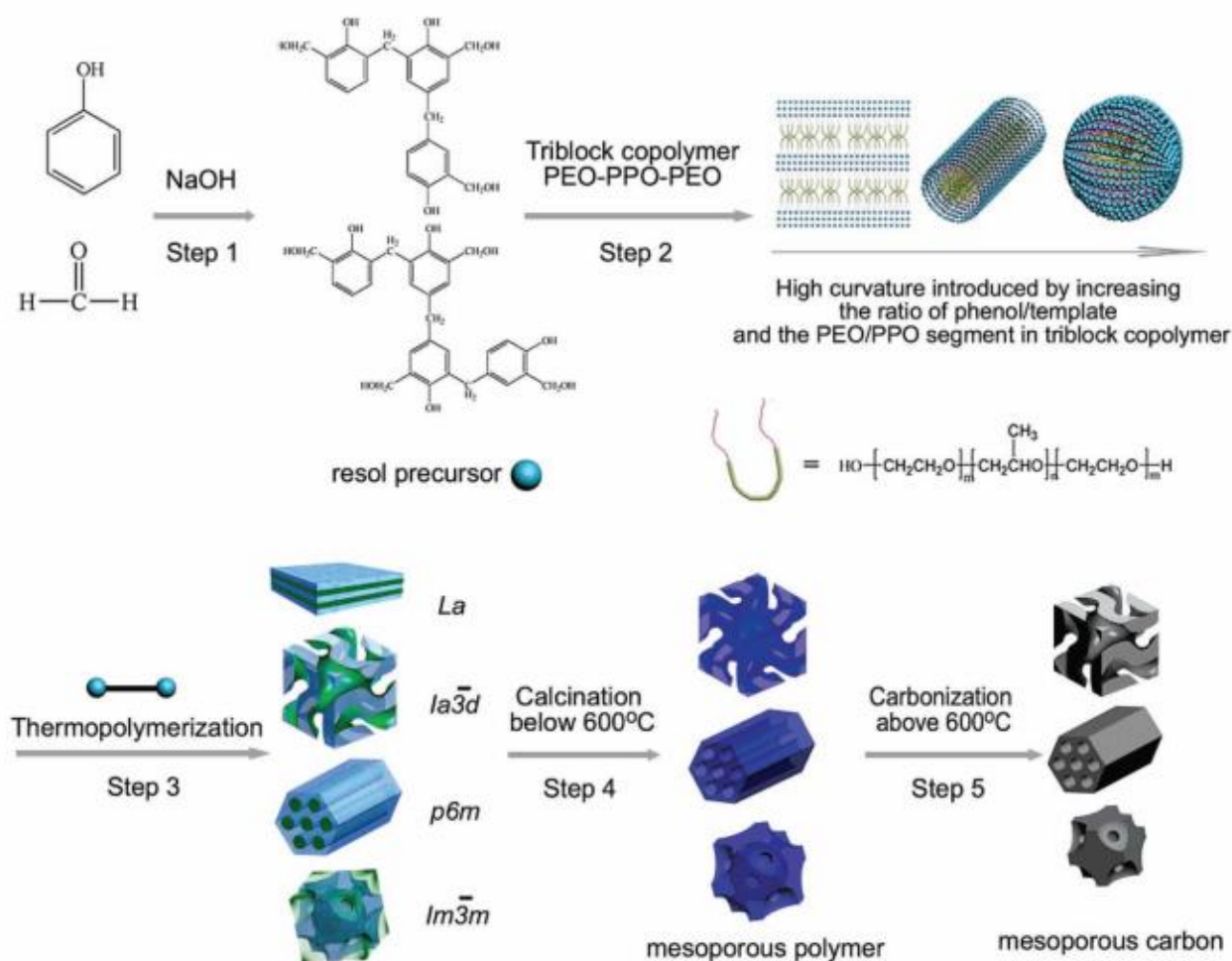
Figure 2.10 Ordered mesoporous carbides synthesized by soft templating approaches. Reprinted with permission from Ref 112. Copyright 2006 American Chemical Society.

c. Other methods

Apart from the conventional hard-templating method and soft-templating approach, many efforts have been made to fabricate mesoporous carbon materials, such as hydrothermal carbonization and the extended Stöber method.

Pioneered by Berguis,[116] the process of hydrothermal carbonization has been concentrated on the fabrication of porous carbon under low-temperature carbonization using biomass derivatives as precursors. The direct hydrothermal carbonization of carbohydrates leads to microporous carbonaceous spheres with limited porosity. By expanding the pore size through adding additives to the synthetic system, kubo et al. reported the synthesis of mesostructured carbon particles.[117] However, it is still challenging to control the porosity, morphology and monodispersity of the resultant carbon synthesized by hydrothermal carbonization.

The Stöber method is a famous route for the preparation of monodispersed colloidal silica nanospheres. This strategy can be further extended to the synthesis of porous carbon materials with different morphologies and tunable structures.[118] Dai et al. reported the synthesis of mesoporous hollow carbon spheres, using the polymerization of resorcinol-formaldehyde (RF) resin and tetraethyl orthosilicate (TEOS) in the presence of cetyltrimethylammonium chloride under Stöber conditions.[119] The extended Stöber method is also applicable for the synthesis of hollow,[120] core-shell,[121] and yolk-shell structures,[122] when adding reformed cores in the reaction system before the polymerisation of resorcinol-formaldehyde resins. Besides resorcinol-formaldehyde precursors, other precursors such as 3-aminophenol,[123] melamine,[124] and dopamine[125] can be used for the preparation of corresponding mesoporous carbon materials with tailored structures.

(3) Macroporous carbon materials

Templating with submicrometer-sized silica or other colloidal crystals composed of monodisperse spheres is the convenient chemical strategy to obtain macroporous carbon materials with hollow structures and interconnected pore systems.[126] The three-dimensionally ordered macroporous (3DOM) carbon products, also called inverse opals, are of interest due to their continuous nanostructured skeleton with the high interfacial area and three-dimensionally interconnected pore system with low tortuosity. The pore size of the resultant inverse opals could be easily tuned by controlling the particle size for the template colloidal particles.
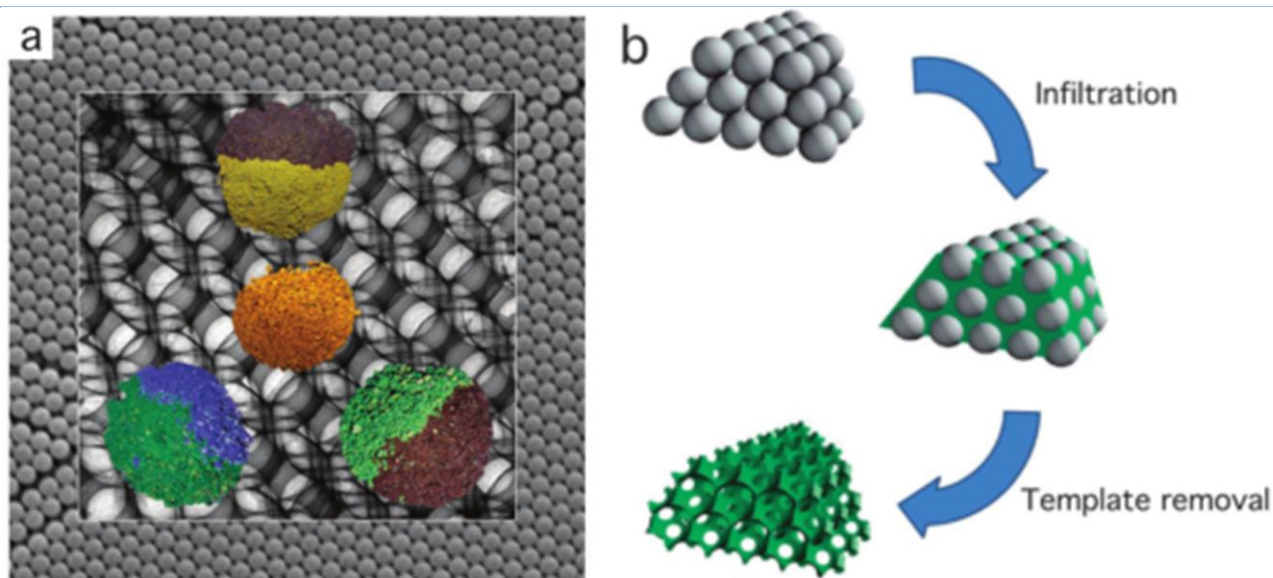
Figure 2.11 a) Color and symmetry in 3DOM materials. The different colors arise from different repeat lengths in the periodic structures and from the presence or absence of methanol in the macropores, b) Schematic of the colloidal crystal templating process. The template with the structure of an opal is infiltrated with precursor material. Processing and template removal produce the inverted structure. Reprinted with permission from Ref 126. Copyright 2013 The Royal Society of Chemistry.

As the visible light with wavelengths on a specific scale is diffracted by the periodic structure of the opal template, the templated structures can possess similar structural colours, as shown in Figure 2.11. The general scheme of synthesis 3DOM carbon materials by crystal templating is relatively straightforward (Figure 2.11b): firstly the dispersion of monodisperse colloidal particles, then assembly these colloidal particles into close-packed arrays, followed by infiltration of the empty volume among template with carbon precursor fluid, then conversion the carbon precursors into an interconnected solid skeleton, finally removal of the original template.

The most common colloidal particles used as a template for the synthesis of 3DOM carbons are uniformly sized Stöber silica spheres[127] and monodisperse polymer spheres, such as polystyrene,[128] poly(methyl methacrylate),[129] and poly(styrene-methylmethacrylate-acrylic acid).[130] Generally, colloidal crystals are assembled using sedimentation,[131] centrifugation,[132] physical confinement,[133] or formation on a patterned substrate.[134] Several infiltration methods are applied in the colloidal crystal templating, such as liquid-phase infiltration,[135] electrochemical deposition,[136] vapour phase deposition,[137] and atomic layer deposition.[138]

The colloidal crystal templating has become a powerful tool for the synthesis of periodic macroporous carbon materials in two and three dimensions. This technique is highly versatile and applicable to many different compositions. Yet, there are numerous concerns to overcome for

practical applications, such as reduce the cost of the colloidal template and increase the assembly rate.

2.3.3 Heteroatoms-doping in porous carbon materials

Heteroatom doped porous carbon materials have shown great potential in the family of porous carbons because of their high electronic conductivity and improved hydrophilic properties.[24] Some heteroatoms (e.g. nitrogen) is also capable of improving the capacity of the porous carbon materials via surface faradic reactions without sacrificing the rate capacity and long cycle life.[139] Several heteroatoms (such as nitrogen, boron, sulfur, and phosphorus) used for carbon doping are briefly summarized in below.

Nitrogen is the most investigated doped heteroatoms for carbonaceous electrode materials over the past decades. As the neighbour of carbon, it is chemically relatively easy to bring nitrogen together with carbon. The concept of nitrogen-doped carbon is pioneered by Jasinski et al in 1964 when applied metal-phthalocyanine-complexes to catalyse the reduction of oxygen in the cathode.[140] Generally, there are four types of doped nitrogen in the nitrogen-doped carbon materials depending on the bonding environments, including pyrrolic N, pyridinic-N, quaternary N (also called graphitic N), and pyridinic-N-oxide, as shown in Figure 2.12.[141] It is shown that the quaternary N species is favourable for the improvement of the electrical conductivity and hydrophilicity.[142] On the other hand, Frackowiak et al. reported the pseudocapacity from doped nitrogen atoms, especially relying on the protonation if pyridinic nitrogen atoms at the graphitic edges.[143]
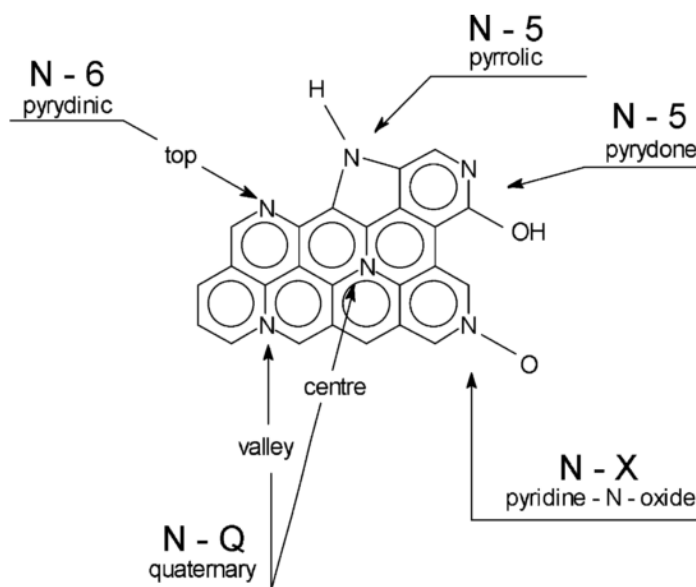
Figure 2.12 Distribution of nitrogen atoms in carbon graphene structure. Reprinted with permission from Ref 141. Copyright 2003 Elsevier.

Boron is an interesting candidate for the doping of carbon materials as an element with unique and incomparable properties in the periodic table. Bartlett et al. reported the synthesis of $B_{0.35}N_{0.35}C_{0.3}$

via chemical vapour deposition method using boron trichloride, ammonia, and acetylene as the precursor mixture.[144] Besides chemical vapour deposition, Ajayan et al. reported the synthesis of boron-doped carbon structures (like thin graphitic sheets, tubes and filaments) using electric arc discharge base synthetic procedure, in which amorphous boron and graphite powder served as precursors.[145] It is demonstrated that the boron-doping also achieves pseudocapacitance effects like nitrogen doping.[146]

Compared to boron, sulfur is less investigated until a few years ago. The concept of sulfur-doped carbon material was discovered by Schmidt in 2011, in which a microporous polymer network containing thienyl building blocks is applied as precursors for the synthesis of sulfur-doped carbon with variable sulfur contents.[147] The sulfur-doping is supposed to increase the interlayer distances in the stacking of carbon sheets, and increase the amount of nanopore at the same time.[148]

Due to a same number of valence electrons, phosphorus shows similar properties as nitrogen. Yet the phosphorus atoms have larger atomic size and lower electronegativity compared to nitrogen atoms. Thus, the phosphorus-doping leads to more structural distortion and more defect-induced active surfaces.[149] In addition, computational studies have predicted a more pronounced influence of phosphorus doping on the bandgap of graphene than that of sulfur.[150] Phosphorus-doping is calculated to improve the electron-donor properties of carbon materials as well.[151]

2.3.4 Application of porous carbon materials in energy storage

(1) Electrical double-layer capacitors

Carbon materials have been widely investigated as the electrode materials in the application of EDLCs due to their superior properties such as high conductivity, high temperature resistance, good corrosion resistance, low cost and excellent compatibility in composites.[152] Porous carbons, including activated carbons, templated carbon, carbon aerogel, carbon nanotube, and graphene, have attracted tremendous attention among carbon materials because of the high specific surface area and controllable pore structure.[153] The porous carbon materials used for electrochemical capacitors are briefly reviewed as follows by paying attentions to their pore characteristics.

According to the principle of the adsorption in EDLCs, the surface area of porous carbon was thought to be the primary requirement to achieve high capacitance. Thus, activated carbons were firstly tested as the electrode material for EDLCs. It is noted that the commercial activated carbons were also used as the reference materials when another novel porous carbon material was reported. The specific surface area of porous carbon materials after physical and chemical activation can reach around 3000 m^2/g.[154]

Like activated carbons, microporous carbon materials with the high specific surface area and abundant pores those sizes less than 2 nm are widely utilized for EDLCs. Huang et al. proposed a

theoretical analysis to split the capacitive behaviour depends on the pore size.[155] The authors found that the specific surface area normalized capacitance is higher in microporous carbons compared to those in mesoporous carbon materials when tested using organic electrolyte (shown in Figure 2.13a). Simon et al. also reported that the carbide-derived carbon with 0.7 nm pore size shows the maximum capacitance in a solvent-free electrolyte, as shown in Figure 2.13b.[156] Although previous reports demonstrated that the highest capacitance is achieved when the pore size is matched with the ion size, the capacitance of microporous carbon does not increase linearly with the specific surface area. Barbieri et al. found that the linear increase of capacitance occurs at the low specific surface area, while a plateau shows when the BET surface area above 1500 m^2/g.[157] One of the possible explanations is considering carbon electrode as a metallic conductor. The wall thickness of the carbon material decreases with the rising of surface area, while the electric potential within the pore wall no longer decays to zero. This incomplete charge screening generated by space constriction greatly limits the gravimetric capacitance of microporous carbons.[158] Moreover, microporous dominated carbon particles also suffer from the electrochemical accessibility problem in the electrolyte solution, which dramatically decreases the rate capacitance of electrode materials.[15] Due to aforementioned reasons, the high capacitive properties of microporous carbons are notably restricted.
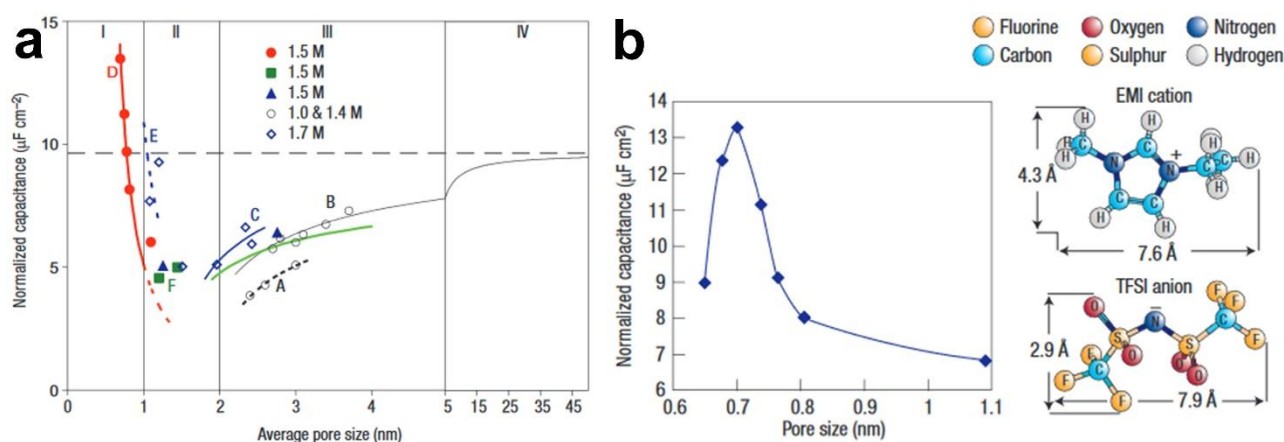
Fig 2.13 a) Experimental data of references fit by equations; the extrapolation of the curve in region III into region IV approaches the broken line calculated by equation using the same parameters as obtained from region III, b) normalized capacitance change vs the pore size of the CDC samples prepared at different temperatures; normalized capacitance is obtained by dividing the specific capacitance by the SSA. HyperChem models of the structure of EMI and TFSI ions show a size correlation. Reprinted with permission from Ref 155 (Copyright 2008 Wiley) and Ref 156 (Copyright 2008 American Chemical Society).

In the past decades, mesoporous carbon materials with pore sizes of 2-50 nm have become promising candidates for EDLC applications. Huang et al. reported the capacitance normalized by

surface area was higher in mesoporous carbon compared to microporous carbon in aqueous condition, either in H_2SO_4 or KOH solutions.[20] Qian et al. reported the synthesis of mesoporous carbon with a high BET surface area of 1300 m^2/g and a high percentage of mesopore surface area (1200 m^2/g). This material showed a high capacitance of 340 F/g at 1 A/g and 66% capacity retention at 10 A/g due to the small pore size of 2-3 nm.[159] Li et al. reported the fabrication of protein-derived carbons with a high mesopore surface area percentage of ~93% but a relatively small total surface area of 810 m^2/g.[160] It is still worth studying the synthesis of mesoporous carbons with large mesopores and high mesopore surface areas (>1400 m^2/g) for EDLCs.

(2) Aluminium-ion batteries

Compared to LIBs, rechargeable aluminium-based batteries offer lower cost and higher safety for energy storage. Jiao et. al reported a new kind of AIBs with carbon paper as the cathode, demonstrating a high average voltage plateau of 1.8V vs. Al^{3+}/Al.[161] Apart from carbon papers, it is shown that the porous carbon materials are promising candidates as electrode materials for AIBs.[162] Dai et al. firstly proposed the configuration of AIBs using three-dimensional graphitic foam as a cathode, aluminum metal as an anode and non-flammable ionic liquid as electrolyte.[40] The authors further applied pristine natural graphite flakes as a cathode material to achieve a high capacity of 110 mAh/g with coulombic efficiency of 98%.[163] Lu et al. reported the synthesis of graphene nanoribbons on highly porous three-dimensional graphene foam as the cathode material for AIBs, reaching the high capacity of 148 mAh/g.[164] However, the graphene foams reported in literatures possess macropores with hundreds of microns, results in low volumetric capacity. It still remains challenging for the facial synthesis of porous carbon material with high tap density and small macropores for AIBs.

2.4 Conclusion and Outlook

Hollow-structured materials have shown great potential in energy storage applications due to their high specific surface area, flexible structures and tunable pore size. The electrode materials with hollowed structures possess the higher capacity and better utility of the material. One sample is the transition metal oxides which have the theoretical capacity twice higher than that of commercialised graphite anodes. Unfortunately, the large volume variation during lithiation and the poor conductivity of material restrict the further application of transition metal oxide in the LIBs, results in capacity decay and unsatisfied rate performance. The synthesis of hollow-structured TMOs is one of the pathways to address aforementioned issues. However, the structural stability and the cycling stability of the hollow-structured TMOs remains challenging during charge-discharge. Therefore, efforts should be made for the fabrication of hollow-structured TMOs with high structural stability and excellent cling stability.

In another aspect, highly porous carbon materials have received tremendous attention as electrode materials for EDLCs. In general, soft-templating method and hard-templating approach are used for the preparation of porous carbon materials. The soft-templating method based on the self-assembly between surfactants (*e.g.*, block copolymers) and carbon precursors (*e.g.*, phenolic resins), while the hard-templating method involves the coating process of carbon precursors to preformed templates, followed by carbonization and selectively etching to obtain carbon products. However, surfactants are both involved in soft-templating method and the synthesis of silica templates used in hard-templating approach. Moreover, the synthesis was usually conducted in solutions, resulting in carbon materials with irregular morphology and relatively low packing density, thus unfavorable for the volumetric performance of batteries and EDLCs. It remains challenging to synthesize highly porous carbon materials with high gravimetric/volumetric performance in the absence of surfactants. Thus, the chapters below will include the design and synthesis of hollow-structured TMOs for LIBs, as well as highly porous carbon microspheres for EDLCs. Polypyrrole-coated double-shelled hollow $ZnFe_2O_4$ microspheres will be synthesized and its electrochemical properties will be evaluated. Nitrogen-doped mesoporous carbon microspheres will be fabricated and its electrochemical performance will be tested. Besides, the structural parameters of porous carbon synthesized by spray drying–vapour deposition method will be investigated.

2.5 References

[1]   Tarascon, J. M.; Armand, M., *Nature* **2001,** *414*, 359.

[2]   Bruce, P. G.; Scrosati, B.; Tarascon, J.-M., *Angew. Chem. Int. Ed.* **2008,** *47*, 2930.

[3]   Whittingham, M. S., *Chem. Rev.* **2004,** *104*, 4271.

[4]   Ellis, B. L.; Lee, K. T.; Nazar, L. F., *Chem. Mater.* **2010,** *22*, 691.

[5]   Wang, Y.; He, P.; Zhou, H., *Energy Environ. Sci.* **2011,** *4*, 805.

[6]   Etacheri, V.; Marom, R.; Elazari, R.; Salitra, G.; Aurbach, D., *Energy Environ. Sci.* **2011,** *4*, 3243.

[7]   Nishi, Y., *The Chemical Record* **2001,** *1*, 406.

[8]   Li, H.; Wang, Z.; Chen, L.; Huang, X., *Adv. Mater.* **2009,** *21*, 4593.

[9]   Reddy, M. V.; Subba Rao, G. V.; Chowdari, B. V. R., *Chem. Rev.* **2013,** *113*, 5364.

[10]   Wang, Z.; Zhou, L.; Lou, X. W., *Adv. Mater.* **2012,** *24* , 1903.

[11]   Simon, P.; Gogotsi, Y., *Nat. Mater.* **2008,** *7*, 845.

[12]   Simon, P.; Gogotsi, Y.; Dunn, B., *Science* **2014,** *343*, 1210.

[13]   Wang, G.; Zhang, L.; Zhang, J., *Chem. Soc. Rev.* **2012,** *41*, 797.

[14]   Kötz, R.; Carlen, M., *Electrochim. Acta* **2000,** *45*, 2483.

[15]   Zhang, L. L.; Zhao, X. S., *Chem. Soc. Rev.* **2009,** *38*, 2520.

[16]   Zhang, K.; Han, X.; Hu, Z.; Zhang, X.; Tao, Z.; Chen, J., *Chem. Soc. Rev.* **2015,** *44*, 699.

[17]   Helmholtz, H., *Ann. Phys.* **1853,** *165*, 211.

[18]   Gouy, M., *J. Phys. Theor. Appl.* **1910,** *9*, 457.

[19]   Chapman, D. L., *The London, Edinburgh, and Dublin philosophical magazine and journal of science* **1913,** *25*, 475.

[20]   Huang, J.; Sumpter, B. G.; Meunier, V., *Chem. Eur. J.* **2008,** *14*, 6614.

[21]   Zhai, Y.; Dou, Y.; Zhao, D.; Fulvio, P. F.; Mayes, R. T.; Dai, S., *Adv. Mater.* **2011,** *23*, 4828.

[22]   Li, W.; Liu, J.; Zhao, D. Y., *Nat. Rev. Mater.* **2016,** *1*, 16023.

[23]   Wang, D.-W.; Li, F.; Liu, M.; Lu, G. Q.; Cheng, H.-M., *Angew. Chem. Int. Ed.* **2008,** *47*, 373.

[24]   Paraknowitsch, J. P.; Thomas, A., *Energy Environ. Sci.* **2013,** *6*, 2839.

[25]   Seh, Z. W.; Sun, Y.; Zhang, Q.; Cui, Y., *Chem. Soc. Rev.* **2016,** *45*, 5605.

[26]   Li, W. Y.; Liang, Z.; Lu, Z. D.; Yao, H. B.; Seh, Z. W.; Yan, K.; Zheng, G. Y.; Cui, Y., *Adv. Energy Mater.* **2015,** *5*, 1500211.

[27]   Xin, S.; Gu, L.; Zhao, N.-H.; Yin, Y.-X.; Zhou, L.-J.; Guo, Y.-G.; Wan, L.-J., *J. Am. Chem. Soc.* **2012,** *134*, 18510.

[28]   Hua, W.; Yang, Z.; Nie, H.; Li, Z.; Yang, J.; Guo, Z.; Ruan, C.; Chen, X.; Huang, S., *Acs Nano* **2017,** *11*, 2209.

[29]   Li, Z.; Zhang, J.; Guan, B.; Wang, D.; Liu, L.-M.; Lou, X. W., *Nat. Commun.* **2016,** *7*, 13065.

[30]   Zhang, H.; Zhou, L.; Huang, X.; Song, H.; Yu, C., *Nano Research* **2016,** *9*, 3725.

[31]   Zhong, Y.; Wang, S.; Sha, Y.; Liu, M.; Cai, R.; Li, L.; Shao, Z., *J. Mater. Chem. A* **2016,** *4*, 9526.

[32]   Wang, Y.-X.; Yang, J.; Lai, W.; Chou, S.-L.; Gu, Q.; Liu, H. K.; Zhao, D.; Dou, S. X., *J. Am. Chem. Soc.* **2016,** *138*, 16576.

[33]   Pei, F.; An, T. H.; Zang, J.; Zhao, X. J.; Fang, X. L.; Zheng, M. S.; Dong, Q. F.; Zheng, N. F., *Adv. Energy Mater.* **2016,** *6*, 1502539.

[34]   Wu, F.; Ye, Y.-S.; Huang, J.-Q.; Zhao, T.; Qian, J.; Zhao, Y.-Y.; Li, L.; Wei, L.; Luo, R.; Huang, Y.-X.; Xing, Y.; Chen, R.-J., *Acs Nano* **2017,** *11*, 4694.

[35]   Li, G.; Sun, J.; Hou, W.; Jiang, S.; Huang, Y.; Geng, J., *Nat. Commun.* **2016,** *7*, 10601.

[36]   Li, M.; Carter, R. E.; Douglas, A.; Oakes, L.; Pint, C. L., *Acs Nano* **2017,** *11*, 4877.

[37]   Wang, F.; Wu, X.; Li, C.; Zhu, Y.; Fu, L.; Wu, Y.; Liu, X., *Energy Environ. Sci.* **2016,** *9*, 3570.

[38]   Li, Q.; Bjerrum, N. J., *J. Power Sources* **2002,** *110*, 1.

[39]   Rani, J. V.; Kanakaiah, V.; Dadmal, T.; Rao, M. S.; Bhavanarushi, S., *J. Electrochem. Soc.* **2013,** *160*, A1781.

[40]   Lin, M.-C.; Gong, M.; Lu, B.; Wu, Y.; Wang, D.-Y.; Guan, M.; Angell, M.; Chen, C.; Yang, J.; Hwang, B.-J.; Dai, H., *Nature* **2015,** *520*, 324.

[41]   Stadie, N. P.; Wang, S.; Kravchyk, K. V.; Kovalenko, M. V., *Acs Nano* **2017,** *11*, 1911.

[42]   Allen, D., *Mater. World* **2008,** *16*, 28.

[43]   Poizot, P.; Laruelle, S.; Grugeon, S.; Dupont, L.; Tarascon, J. M., *Nature* **2000,** *407*, 496.

[44]   Lai, X.; Halpert, J. E.; Wang, D., *Energy Environ. Sci.* **2012,** *5*, 5604.

[45]   Park, G. D.; Lee, J.-H.; Lee, J.-K.; Kang, Y. C., *Nano Research* **2014,** *7*, 1738.

[46]   Yao, L.; Hou, X.; Hu, S.; Ru, Q.; Tang, X.; Zhao, L.; Sun, D., *J. Solid State Electrochem.* **2013,** *17*, 2055.

[47]   Guo, X.; Lu, X.; Fang, X.; Mao, Y.; Wang, Z.; Chen, L.; Xu, X.; Yang, H.; Liu, Y., *Electrochem. Commun.* **2010,** *12*, 847.

[48]   Liu, J.; Xue, D., *Nanoscale Res. Lett.* **2010,** *5*, 1525.

[49]   Zhong, Z.; Yin, Y.; Gates, B.; Xia, Y., *Adv. Mater.* **2000,** *12*, 206.

[50]   Wu, C.; Zhang, X.; Ning, B.; Yang, J.; Xie, Y., *Inorg. Chem.* **2009,** *48*, 6044.

[51]   Cao, J.; Zhu, Y.; Shi, L.; Zhu, L.; Bao, K.; Liu, S.; Qian, Y., *Eur. J. Inorg. Chem.* **2010,** *2010*, 1172.

[52]   Ding, Y.-L.; Zhao, X.-B.; Xie, J.; Cao, G.-S.; Zhu, T.-J.; Yu, H.-M.; Sun, C.-Y., *J. Mater. Chem.* **2011,** *21*, 9475.

[53]   Wang, Z.; Luan, D.; Li, C. M.; Su, F.; Madhavi, S.; Boey, F. Y. C.; Lou, X. W., *J. Am. Chem. Soc.* **2010,** *132*, 16271.

[54]   Sun, X.; Li, Y., *Angew. Chem. Int. Ed.* **2004,** *43*, 3827.

[55]   Titirici, M.-M.; Antonietti, M.; Thomas, A., *Chem. Mater.* **2006,** *18*, 3808.

[56]   Sun, X.; Liu, J.; Li, Y., *Chem. Eur. J.* **2006,** *12*, 2039.

[57]   Nor, Y. A.; Zhou, L.; Meka, A. K.; Xu, C.; Niu, Y.; Zhang, H.; Mitter, N.; Mahony, D.; Yu, C., *Adv. Funct. Mater.* **2016,** *26*, 5408.

[58]   Lai, X.; Li, J.; Korgel, B. A.; Dong, Z.; Li, Z.; Su, F.; Du, J.; Wang, D., *Angew. Chem. Int. Ed.* **2011,** *50*, 2738.

[59]   Li, Z.; Lai, X.; Wang, H.; Mao, D.; Xing, C.; Wang, D., *J. Phys. Chem. C* **2009,** *113*, 2792.

[60]   Haisheng, Q.; Guofeng, L.; Yunxia, Z.; Poernomo, G.; Rong, X., *Nanotechnology* **2007,** *18*, 355602.

[61]   Yelamanchili, R. S.; Lu, Y.; Lunkenbein, T.; Miyajima, N.; Yan, L.-T.; Ballauff, M.; Breu, J., *Small* **2009,** *5*, 1326.

[62]   Cho, W.; Lee, Y. H.; Lee, H. J.; Oh, M., *Adv. Mater.* **2011,** *23*, 1720.

[63]   Zeng, Y.; Wang, X.; Wang, H.; Dong, Y.; Ma, Y.; Yao, J., *Chem. Commun.* **2010,** *46*, 4312.

[64]   Zhou, L.; Xu, H.; Zhang, H.; Yang, J.; B. Hartono, S.; Qian, K.; Zou, J.; Yu, C., *Chem. Commun.* **2013,** *49*, 8695.

[65]   Mou, F.; Guan, J.-g.; Shi, W.; Sun, Z.; Wang, S., *Langmuir* **2010,** *26*, 15580.

[66]   Yang, M.; Ma, J.; Niu, Z.; Dong, X.; Xu, H.; Meng, Z.; Jin, Z.; Lu, Y.; Hu, Z.; Yang, Z., *Adv. Funct. Mater.* **2005,** *15*, 1523.

[67] Yang, M.; Ma, J.; Zhang, C.; Yang, Z.; Lu, Y., *Angew. Chem. Int. Ed.* **2005,** *44*, 6727.

[68] Buchold, D. H. M.; Feldmann, C., *Nano Lett.* **2007,** *7*, 3489.

[69] Zimmermann, C.; Feldmann, C.; Wanner, M.; Gerthsen, D., *Small* **2007,** *3*, 1347.

[70] Ding, Y.; Hu, Y.; Jiang, X.; Zhang, L.; Yang, C., *Angew. Chem. Int. Ed.* **2004,** *43*, 6369.

[71] Xu, H.; Wang, W., *Angew. Chem. Int. Ed.* **2007,** *46*, 1489.

[72] Wu, Z.; Zhang, M.; Yu, K.; Zhang, S.; Xie, Y., *Chem. Eur. J.* **2008,** *14*, 5346.

[73] Li, J.; Zeng, H. C., *J. Am. Chem. Soc.* **2007,** *129*, 15839.

[74] Liu, B.; Zeng, H. C., *Small* **2005,** *1*, 566.

[75] Wang, Y.; Cao, G., *Adv. Mater.* **2008,** *20*, 2251.

[76] Ning, J.; Dai, Q.; Jiang, T.; Men, K.; Liu, D.; Xiao, N.; Li, C.; Li, D.; Liu, B.; Zou, B.; Zou, G.; Yu, W. W., *Langmuir* **2009,** *25*, 1818.

[77] Lou, X. W.; Yuan, C.; Archer, L. A., *Small* **2007,** *3*, 261.

[78] Liu, J.; Xia, H.; Xue, D.; Lu, L., *J. Am. Chem. Soc.* **2009,** *131*, 12086.

[79] Yang, H. X.; Qian, J. F.; Chen, Z. X.; Ai, X. P.; Cao, Y. L., *J. Phys. Chem. C* **2007,** *111*, 14067.

[80] Wang, X.; Wu, X.-L.; Guo, Y.-G.; Zhong, Y.; Cao, X.; Ma, Y.; Yao, J., *Adv. Funct. Mater.* **2010,** *20*, 1680.

[81] Won, J. M.; Choi, S. H.; Hong, Y. J.; Ko, Y. N.; Kang, Y. C., *Sci. rep.* **2014,** *4*, 5857.

[82] Deng, Y.; Zhang, Q.; Tang, S.; Zhang, L.; Deng, S.; Shi, Z.; Chen, G., *Chem Commun (Camb)* **2011,** *47*, 6828.

[83] Zou, F.; Hu, X.; Li, Z.; Qie, L.; Hu, C.; Zeng, R.; Jiang, Y.; Huang, Y., *Adv. Mater.* **2014,** *26*, 6622.

[84] Sing, K. S. W.; Everett, D. H.; Haul, R. A. W.; Moscou, L.; Pierotti, R. A.; Rouquerol, J.; Siemieniewska, T., *Pure Appl. Chem.* **1985,** *57*, 603.

[85] Frackowiak, E.; Béguin, F., *Carbon* **2001,** *39*, 937.

[86] Ioannidou, O.; Zabaniotou, A., *Renewable Sustainable Energy Rev.* **2007,** *11*, 1966.

[87]   Shen, G.; Sun, X.; Zhang, H.; Liu, Y.; Zhang, J.; Meka, A.; Zhou, L.; Yu, C., *J. Mater. Chem. A* **2015,** *3*, 24041.

[88]   Lee, J.; Kim, J.; Hyeon, T., *Adv. Mater.* **2006,** *18*, 2073.

[89]   Miura, K.; Hayashi, J.; Hashimoto, K., *Carbon* **1991,** *29*, 653.

[90]   Nakagawa, H.; Watanabe, K.; Harada, Y.; Miura, K., *Carbon* **1999,** *37*, 1455.

[91]   Jones, C. W.; Koros, W. J., *Carbon* **1994,** *32*, 1419.

[92]   Kyotani, T.; Nagai, T.; Inoue, S.; Tomita, A., *Chem. Mater.* **1997,** *9*, 609.

[93]   Gogotsi, Y.; Dash, R. K.; Yushin, G.; Yildirim, T.; Laudisio, G.; Fischer, J. E., *J. Am. Chem. Soc.* **2005,** *127*, 16006.

[94]   Ma, Z.; Kyotani, T.; Tomita, A., *Chem. Commun.* **2000,** 2365.

[95]   Johnson, S. A.; Brigham, E. S.; Ollivier, P. J.; Mallouk, T. E., *Chem. Mater.* **1997,** *9*, 2448.

[96]   Chmiola, J.; Yushin, G.; Dash, R. K.; Hoffman, E. N.; Fischer, J. E.; Barsoum, M. W.; Gogotsi, Y., *Electrochem. Solid-State Lett.* **2005,** *8*, A357.

[97]   J änes, A.; Permann, L.; Arulepp, M.; Lust, E., *Electrochem. Commun.* **2004,** *6*, 313.

[98]   Liu, C.; Li, F.; Ma, L.-P.; Cheng, H.-M., *Adv. Mater.* **2010,** *22*, E28.

[99]   Borchardt, L.; Hoffmann, C.; Oschatz, M.; Mammitzsch, L.; Petasch, U.; Herrmann, M.; Kaskel, S., *Chem. Soc. Rev.* **2012,** *41*, 5053.

[100]   Lezanska, M.; Wloch, J.; Szymański, G.; Szpakowska, I.; Kornatowski, J., *Catal. Today* **2010,** *150*, 77.

[101]   Han, S.; Lee, K. T.; Oh, S. M.; Hyeon, T., *Carbon* **2003,** *41*, 1049.

[102]   Yang, H.; Shi, Q.; Liu, X.; Xie, S.; Jiang, D.; Zhang, F.; Yu, C.; Tu, B.; Zhao, D., *Chem. Commun.* **2002,** 2842.

[103]   Schuster, J.; He, G.; Mandlmeier, B.; Yim, T.; Lee, K. T.; Bein, T.; Nazar, L. F., *Angew. Chem. Int. Ed.* **2012,** *124*, 3651.

[104]   Sun, Z.; Liu, Y.; Li, B.; Wei, J.; Wang, M.; Yue, Q.; Deng, Y.; Kaliaguine, S.; Zhao, D., *Acs Nano* **2013,** *7*, 8706.

[105]   Kim, T.-W.; Chung, P.-W.; Slowing, I. I.; Tsunoda, M.; Yeung, E. S.; Lin, V. S.-Y., *Nano Lett.* **2008,** *8*, 3724.

[106]   Liu, R.; Mahurin, S. M.; Li, C.; Unocic, R. R.; Idrobo, J. C.; Gao, H.; Pennycook, S. J.; Dai, S., *Angew. Chem. Int. Ed.* **2011,** *50*, 6799.

[107]   Chen, X.; Kierzek, K.; Jiang, Z.; Chen, H.; Tang, T.; Wojtoniszak, M.; Kalenczuk, R. J.; Chu, P. K.; Borowiak-Palen, E., *J. Phy. Chem. C* **2011,** *115*, 17717.

[108]   Lu, A. H.; Sun, T.; Li, W. C.; Sun, Q.; Han, F.; Liu, D. H.; Guo, Y., *Angew. Chem. Int. Ed.* **2011,** *50*, 11765.

[109]   Liang, C.; Hong, K.; Guiochon, G. A.; Mays, J. W.; Dai, S., *Angew. Chem. Int. Ed.* **2004,** *43*, 5785.

[110]   Zhang, F.; Meng, Y.; Gu, D.; Yan, Y.; Yu, C.; Tu, B.; Zhao, D., *J. Am. Chem. Soc.* **2005,** *127*, 13508.

[111]   Zhang, F.; Meng, Y.; Gu, D.; Yan, Y.; Chen, Z.; Tu, B.; Zhao, D., *Chem. Mater.* **2006,** *18*, 5279.

[112]   Meng, Y.; Gu, D.; Zhang, F.; Shi, Y.; Cheng, L.; Feng, D.; Wu, Z.; Chen, Z.; Wan, Y.; Stein, A.; Zhao, D., *Chem. Mater.* **2006,** *18*, 4447.

[113]   Liang, C.; Dai, S., *J. Am. Chem. Soc.* **2006,** *128*, 5316.

[114]   Wang, X.; Liang, C.; Dai, S., *Langmuir* **2008,** *24*, 7500.

[115]   Mayes, R. T.; Tsouris, C.; Kiggans Jr, J. O.; Mahurin, S. M.; DePaoli, D. W.; Dai, S., *J. Mater. Chem.* **2010,** *20*, 8674.

[116]   Bergius, F., *Die Anwendung hoger durcke bei chemischen Vorgängen und eine Nachbildung des Entstehungsprozesses der Steinkohle*. W. Knapp: **1913**.

[117]   Kubo, S.; White, R. J.; Yoshizawa, N.; Antonietti, M.; Titirici, M.-M., *Chem. Mater.* **2011,** *23*, 4882.

[118]   Zhang, X.; Li, Y.; Cao, C., *J. Mater. Chem.* **2012,** *22*, 13918.

[119]   Qiao, Z.-A.; Guo, B.; Binder, A. J.; Chen, J.; Veith, G. M.; Dai, S., *Nano Lett.* **2012,** *13*, 207.

[120]   Fuertes, A. B.; Valle-Vigón, P.; Sevilla, M., *Chem. Commun.* **2012,** *48*, 6124.

[121] Li, N.; Zhang, Q.; Liu, J.; Joo, J.; Lee, A.; Gan, Y.; Yin, Y., *Chem. Commun.* **2013,** *49*, 5135.

[122] Liu, R.; Qu, F.; Guo, Y.; Yao, N.; Priestley, R. D., *Chem. Commun.* **2014,** *50*, 478.

[123] Yang, T.; Liu, J.; Zhou, R.; Chen, Z.; Xu, H.; Qiao, S. Z.; Monteiro, M. J., *J. Mater. Chem. A* **2014,** *2*, 18139.

[124] Zhou, H.; Xu, S.; Su, H.; Wang, M.; Qiao, W.; Ling, L.; Long, D., *Chem. Commun.* **2013,** *49*, 3763.

[125] Noonan, O.; Zhang, H.; Song, H.; Xu, C.; Huang, X.; Yu, C., *J. Mater. Chem. A* **2016,** *4*, 9063.

[126] Stein, A.; Wilson, B. E.; Rudisill, S. G., *Chem. Soc. Rev.* **2013,** *42*, 2763.

[127] Stöber, W.; Fink, A.; Bohn, E., *J. Colloid Interface Sci.* **1968,** *26*, 62.

[128] Holland, B. T.; Blanford, C. F.; Do, T.; Stein, A., *Chem. Mater.* **1999,** *11*, 795.

[129] Schroden, R. C.; Al-Daous, M.; Sokolov, S.; Melde, B. J.; Lytle, J. C.; Stein, A.; Carbajo, M. C.; Fernández, J. T.; Rodríguez, E. E., *J. Mater. Chem.* **2002,** *12*, 3261.

[130] Wang, J.; Wen, Y.; Ge, H.; Sun, Z.; Zheng, Y.; Song, Y.; Jiang, L., *Macromol. Chem. Phys.* **2006,** *207*, 596.

[131] Mayoral, R.; Requena, J.; Moya, J. S.; López, C.; Cintas, A.; Miguez, H.; Meseguer, F.; Vázquez, L.; Holgado, M.; Blanco, Á., *Adv. Mater.* **1997,** *9*, 257.

[132] Waterhouse, G. I.; Waterland, M. R., *Polyhedron* **2007,** *26*, 356.

[133] Park, S. H.; Qin, D.; Xia, Y., *Adv. Mater.* **1998,** *10*, 1028.

[134] Van Blaaderen, A.; Ruel, R.; Wiltzius, P., *Nature* **1997,** *385*, 321.

[135] Zhang, Z.; Shen, W.; Ye, C.; Luo, Y.; Li, S.; Li, M.; Xu, C.; Song, Y., *J. Mater. Chem.* **2012,** *22*, 5300.

[136] Tian, S.; Wang, J.; Jonas, U.; Knoll, W., *Chem. Mater.* **2005,** *17*, 5726.

[137] Zhang, X.; Yan, W.; Yang, H.; Liu, B.; Li, H., *Polymer* **2008,** *49*, 5446.

[138] Graugnard, E.; Chawla, V.; Lorang, D.; Summers, C., *Appl. Phys. Lett.* **2006,** *89*, 211102.

[139] Deng, Y.; Xie, Y.; Zou, K.; Ji, X., *J. Mater. Chem. A* **2016,** *4*, 1144.

[140] Jasinski, R., *Nature* **1964,** *201*, 1212.

[141] Jurewicz, K.; Babeł, K.; Źiółkowski, A.; Wachowska, H., *Electrochim. Acta* **2003,** *48*, 1491.

[142] Hou, J.; Cao, C.; Idrees, F.; Ma, X., *Acs Nano* **2015,** *9*, 2556.

[143] Lota, G.; Lota, K.; Frackowiak, E., *Electrochem. Commun.* **2007,** *9*, 1828.

[144] Kaner, R.; Kouvetakis, J.; Warble, C.; Sattler, M.; Bartlett, N., *Mater. Res. Bull.* **1987,** *22*, 399.

[145] Stephan, O.; Ajayan, P.; Colliex, C.; Redlich, P., *Science* **1994,** *266*, 1683.

[146] Guo, H.; Gao, Q., *J. Power Sources* **2009,** *186*, 551.

[147] Thomas, A., *Angew. Chem. Int. Ed.* **2010,** *49*, 8328.

[148] Yan, Y.; Yin, Y.-X.; Xin, S.; Guo, Y.-G.; Wan, L.-J., *Chem. Commun.* **2012,** *48*, 10663.

[149] Kumar, N. A.; Baek, J.-B., *Nanotechnology* **2015,** *26*, 492001.

[150] Denis, P. A., *Comput. Mater. Sci.* **2013,** *67*, 203.

[151] Strelko, V.; Kuts, V.; Thrower, P., *Carbon* **2000,** *38*, 1499.

[152] Inagaki, M.; Konno, H.; Tanaike, O., *J. Power Sources* **2010,** *195*, 7880.

[153] Pandolfo, A. G.; Hollenkamp, A. F., *J. Power Sources* **2006,** *157*, 11.

[154] Wang, J.; Kaskel, S., *J. Mater. Chem.* **2012,** *22*, 23710.

[155] Huang, J.; Sumpter, B. G.; Meunier, V., *Angew. Chem. Int. Ed.* **2008,** *47*, 520.

[156] Largeot, C.; Portet, C.; Chmiola, J.; Taberna, P.-L.; Gogotsi, Y.; Simon, P., *J. Am. Chem. Soc.* **2008,** *130*, 2730.

[157] Barbieri, O.; Hahn, M.; Herzog, A.; Kötz, R., *Carbon* **2005,** *43*, 1303.

[158] Weingarth, D.; Zeiger, M.; Jackel, N.; Aslan, M.; Feng, G.; Presser, V., *Adv. Energy Mater.* **2014,** *4*, 1400316.

[159] Qian, W.; Sun, F.; Xu, Y.; Qiu, L.; Liu, C.; Wang, S.; Yan, F., *Energy Environ. Sci.* **2014,** *7*, 379.

[160]   Li, Z.; Xu, Z.; Tan, X.; Wang, H.; Holt, C. M. B.; Stephenson, T.; Olsen, B. C.; Mitlin, D., *Energy Environ. Sci.* **2013,** *6*, 871.

[161]   Sun, H.; Wang, W.; Yu, Z.; Yuan, Y.; Wang, S.; Jiao, S., *Chem. Commun.* **2015,** *51*, 11892.

[162]   Wu, Y.; Gong, M.; Lin, M. C.; Yuan, C.; Angell, M.; Huang, L.; Wang, D. Y.; Zhang, X.; Yang, J.; Hwang, B. J., *Adv. Mater.* **2016,** *28*, 9218.

[163]   Wang, D.-Y.; Wei, C.-Y.; Lin, M.-C.; Pan, C.-J.; Chou, H.-L.; Chen, H.-A.; Gong, M.; Wu, Y.; Yuan, C.; Angell, M.; Hsieh, Y.-J.; Chen, Y.-H.; Wen, C.-Y.; Chen, C.-W.; Hwang, B.-J.; Chen, C.-C.; Dai, H., *Nat. Commun.* **2017,** *8*, 14283.

[164]   Yu, X.; Wang, B.; Gong, D.; Xu, Z.; Lu, B., *Adv. Mater.* **2017,** *29*, DOI: 10.1002/adma.201604118.

Chapter 3

Research methodology

This chapter summarizes the synthetic methods and characterizations of the materials used in this Ph.D. project. The techniques used for the electrochemical test are also included in this chapter.

3.1 Materials synthesis

3.1.1 Spray drying

Spray drying is a method of producing dry powders from a liquid or slurry by rapidly drying under hot gas. It has been widely applied in food, pharmaceuticals, and nanotechnology. Reproducible powder production with consistent particle size distribution is a feature for spray drying. Air is the heated drying medium; however, nitrogen is used if the liquid is a flammable solvent or the product is oxygen-sensitive.

The digital image of spray dryer used in the project is shown in Figure 3.1a. Figure 3.1b shows the functional principle of this spray dryer. The feeding solution or suspension is pumped into the spray nozzle through a peristaltic pump then sprayed into a hot drying medium in the chamber to form controlled droplets. The solvent of the droplet is evaporated due to the high specific surface area, existing temperature, and moisture gradients. Drying chamber design and air flow rate ensure the completed moisture removal and the solid products are collected in the collection vessel by cyclone technology.
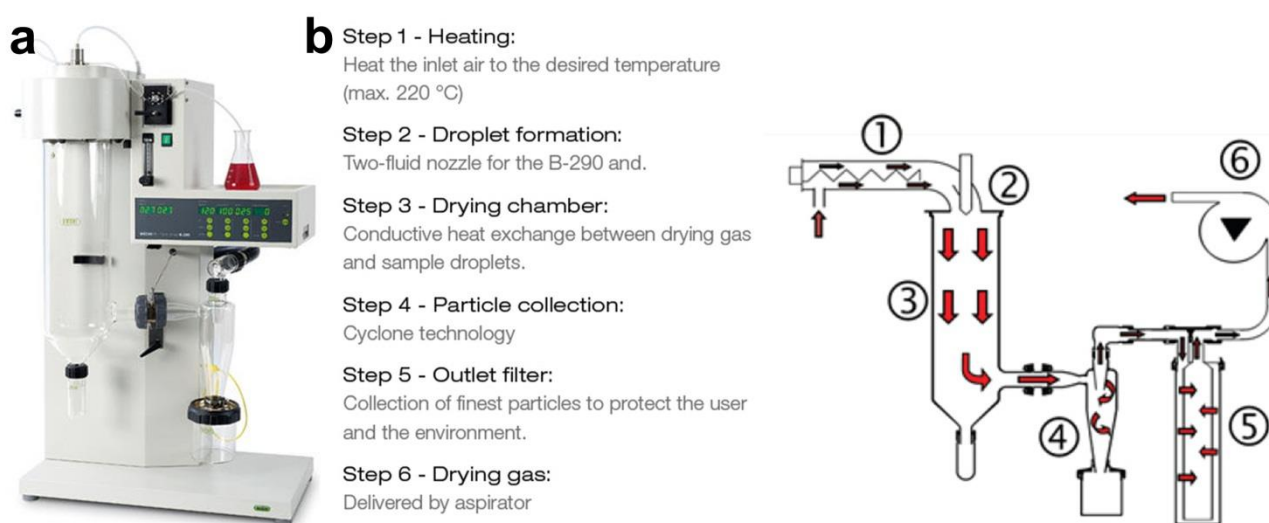
Figure 3.1 a) Digital image and b) functional principle of Buchi mini spray dryer B-290.

In this thesis, the $ZnFe_2O_4$ double shell hollow sphere in $ZnFe_2O_4$-PPY composite is produced in a Buchi mini spray dryer B-290 followed by calcination. Spray drying method is used for rapid spherical intermediate production with a homogenous distribution of precursors. The micro-spherical silica templates for porous carbon materials are produced using spray drying method as well. Taking the advantage of volume reduction, a spray dryer is used for micro-sized assembly of primary nanoparticles. The $FeCl_3$ catalyst is homogeneously attached on the surface of the template microspheres at the same time.

3.1.2 Vapour deposition

A thin coating of polypyrrole in the $ZnFe_2O_4$-PPY composite was synthesized via vapour deposition of pyrrole. Nitrogen-doped porous carbon materials were fabricated by carbonizing the vapour-deposited PPY layer, followed by removing the sacrificial template. Due to the high vapour pressure of pyrrole, the vapour monomer is easily oxidized and attached when to expose the oxidizer, forming layers of PPY.[2] The thickness of the PPY coating is precisely controlled by tuning oxidizer amount and/or reaction time.[3] In our experiment, the glass bottle was used for a closed apparatus for the generation sufficient pyrrole vapour. $FeCl_3$ was used as the oxidizer.

3.2 Characterization

3.2.1 Electron microscopy

(1) The scanning electron microscope (SEM) images were obtained using field emission JSM JEOL 7001F and JEOL 7800. The sample was dispersed in ethanol and then dropped on aluminum foil attached on conductive carbon tape.

(2) Transmission electron microscopy (TEM) images were performed on JEOL 1010 (accelerating voltage of 100 kV) and Tecnai F20 (accelerating voltage of 200 kV). Elemental mapping was conducted on a JEOL 2100 equipped with a JEOL thin-window energy dispersive x-ray detector operated at 200 kV. Samples were dispersing in ethanol before coating on Cu grids.

(3) Cross-section TEM images were conducted on JEOL 1010 (accelerating voltage of 100 kV). The sample was dispersed in melted epoxy resin and embedded for 48 h. The epoxy resin was cut into 60 nm thickness slice with a diamond knife and then transferred on hollow Cu grids.

3.2.2 X-ray diffraction

Wide-angle X-ray diffraction (XRD) patterns were collected on Rigaku Miniflex X-ray Diffractometer with Co Kα radiation (λ=0.179 nm). The signal was collected from 20° to 80° at a scanning rate of 2 °min^{-1}.

The corresponding interplanar spacing is calculated based on the Bragg equation:

$$2d_{hkl} \sin\theta = n\lambda \qquad\qquad (3.1)$$

where d_{hkl} is the interplanar spacing between a set of parallel planes (nm), λ is the wavelength of Co Kα ray (nm), θ is the diffraction angle (°), and n is integer determined by a given order.[4]

3.2.3 Nitrogen sorption

Nitrogen adsorption/desorption isotherms were performed at 77 K by using a Micromeritics ASAP Tristar II 3020 system. Before measurements, 50 mg of each sample was weighted and degassed at 453 K under vacuum for at least 8 h. The pore size distribution was calculated from the adsorption branch of the isotherm using the Barrett–Joyner–Halanda (BJH) method. The Brunauer–Emmett–Teller (BET) method was used to calculate the specific surface areas in a relative pressure (P/P_0) range from 0.05 to 0.30. Total pore volume was calculated from the amount of liquid nitrogen adsorbed at a P/P_0 of 0.99.

3.2.4 Dynamic light scattering

Dynamic Light Scattering (DLS) measurements were conducted at 25 ℃ on a Malvern Zetasizer Nano-ZS. The samples were dispersed in deionized water or ethanol by ultra-sonication before analysis.

3.2.5 Fourier transform infrared (FTIR) spectroscopy

Fourier transform infrared (FTIR) spectra were carried out on ThermoNicolet Nexus 6700 FTIR spectrometer equipped with diamond crystal. For each spectrum, 128 scans were collected at a resolution of 4 cm^{-1} over the range 700–2000 cm^{-1}.

3.2.6 Thermogravimetric analysis

Thermogravimetric analysis (TGA) was performed using METTLER TOLEDO TGA/DSC1 STAR^e System from 25 to 900 ℃ under air flow with a rate of 5 ℃ min^{-1}.

3.2.7 X-ray photoelectron spectroscopy

The X-ray photoelectron spectroscopy (XPS) survey was performed with a Kratos Axis Ultra X-ray photoelectron spectrometer (Perkin-Elmer). All spectra were acquired at a basic pressure of 2×10^{-7} Torr with Mg Kα excitation at 15 kV. The results were analysed using the CasaXPS software and calibrated with the reference of C 1s peak at 284.8 eV.[5]

3.2.8 Elemental analysis

Elemental analysis (EA) was carried out using a CHNS-O Analyzer (Flash EA1112 Series, Thermo Electron Corporation) to determine the proportion of carbon (C) and nitrogen (N), according to the dynamic flash combustion (modified Dumas method). Cysteine with 29.99 wt. % of carbon and 11.66 wt. % of nitrogen was used as the standard control sample.

When the sample enters the, inserted into the reactor and heated in the furnace at 950 ℃, a small volume of pure oxygen (250mL/min) is added to the system to burn the material, converting the

sample into simple elemental gases. A separation column and TCD detector is used to determine the concentration of each element without using other complex splitting systems.

3.2.9 Electron tomography

Electron tomography (ET) was performed on an FEI Tecnai F30 electron microscope operating at 300 kV. The ET specimens were prepared by dispersing the samples in ethanol followed by ultrasonication and then depositing the suspension directly onto copper grids (2000×1000 slot, Proscitech) with Formvar supporting films. Colloidal gold particles (10 nm) were deposited on both surfaces of the grid as fiducial markers for the subsequent image alignment procedures. The tomographic tilt series were carried out by tilting the specimen inside the microscope around the double axis from $+70°$ to $-70°$ at an increment of $1°$ under the electron beam. Alignment and 3D reconstructions were carried out on IMOD software.[6]

3.3 Electrochemical measurements

3.3.1 Electrode preparation and device assembly of LIBs

The working electrodes were comprised of 70 wt. % active material, 20 wt. % conductive acetylene black (carbon black), and 10 wt. % polyvinylidene fluoride (PVDF). N-Methyl-2-pyrrolidone (NMP) was used as the solvent for the mixture. The mixture was continuously stirred until a homogeneous slurry was formed at room temperature. The slurry was cast onto Cu foil and dried under vacuum at 120 ℃ overnight. The electrodes were punched into small disks with a diameter of 7 mm.

Two-electrode Swagelok-type cells were assembled in the Ar-filled glovebox with oxygen and moisture concentration below 0.1 ppm. Metallic lithium chips were used as both the counter electrode and reference electrode, 1 M $LiPF_6$ solution in ethylene carbonate (EC)/ethylmethyl carbonate (EMC)/dimethyl carbonate (DEC) (1:1:1 in volume) was used as the electrolyte.

3.3.2 Evaluation of LIBs

The cells were galvanostatically charged/discharged under different current densities using an MTI 8 Channels Battery Analyzer. The specific capacity is calculated based on the total mass of the active materials. Electrochemical Impedance Spectroscopy (EIS) measurements were performed on Solartron 1480 MultiStat instrument in the frequency range of 100 kHz to 0.01 Hz. All measurements were carried out at room temperature. After cycling, the cell was disassembled and the electrode was dispersed in ethanol by sonication and washed with ethanol for three times.

3.3.3 Electrode preparation and device assembly of EDLCs

A slurry composing of active material (80 wt. %), carbon black (10 wt. %), and polytetrafluoroethylene (PTFE, Sigma-Aldrich, 60 wt. % dispersion in H_2O) (10 wt. %) was mixed with ethanol. The working electrode was prepared by encapsulating mixture into Ni foam and dried at 100 ℃ overnight. A three-electrode system was used to measure the electrochemical performance in 6 M KOH solution. Ni foam and Hg/HgO electrode were served as the counter and reference electrode, respectively.

3.3.4 Evaluation of EDLCs

Electrochemical measurements were carried out over a 1 V potential window (-1~0 V vs. Hg/HgO) using Solartron Multistat 1480.

3.3.5 Electrode preparation and device assembly of AIBs

The working electrodes were comprised of 70 wt. % active material, 15 wt. % conductive acetylene black (carbon black), and 15 wt. % polyvinylidene fluoride (PVDF). N-Methyl-2-pyrrolidone (NMP) was used as the solvent for the mixture. The mixture was continuously stirred until a homogeneous slurry was formed at room temperature. The slurry was cast onto carbon cloth and dried under vacuum at 120 ℃ overnight. Then the electrodes were punched into small disks for cell assembly.

Standard CR2032-type coin cells were assembled in the Ar-filled glovebox with oxygen and moisture concentration below 0.1 ppm. Aluminum foil was used as an anode, glass fiber (Filtech) was used as the separator and carbon felt (Sigma-Aldrich) pellet as a spacer. 1-Ethyl-3-methylimidazolium chloride-aluminum chloride (EMImCl-AlCl$_3$, 1:1.3 by mole) was used as the electrolyte (~150 μL per cell). The coin cells were modified with PEDOT coating before battery assembling. Typically, PEDOT aqueous solution (1.1 wt. %) (10 mL) was blended with ethanol (30 mL) to form a homogeneous coating solution. For each coin cell case, 160 μL coating solution was dropped onto its inner surface by pipette. Then the cell cases were transferred into 50 ℃ vacuum oven and dried overnight.

3.3.6 Evaluation of AIBs

Galvanostatic charge/discharge measurements were conducted on Land battery testers. The voltage range for both CV and galvanostatic charge/discharge measurements is 0.5-2.45 V. All measurements were carried out at room temperature.

3.4 References

[1]   Han, F.; Li, D.; Li, W.-C.; Lei, C.; Sun, Q.; Lu, A.-H., *Adv. Funct. Mater.* **2013,** *23*, 1692.

[2]   Lovett, J. R.; Fielding, L. A.; Armes, S. P.; Buxton, R., *Adv. Funct. Mater.* **2014,** *24*, 1290.

[3]   Weidenthaler, C., *Nanoscale* **2011,** *3*, 792.

[4]   Pels, J. R.; Kapteijn, F.; Moulijn, J. A.; Zhu, Q.; Thomas, K. M., *Carbon* **1995,** *33*, 1641.

[5]   Kremer, J. R.; Mastronarde, D. N.; McIntosh, J. R., *J. Struct. Biol.* **1996,** *116*, 71.

Chapter 4

Polypyrrole Coated Zinc Ferrite Hollow Spheres with Improved Cycling Stability for Lithium-ion Batteries
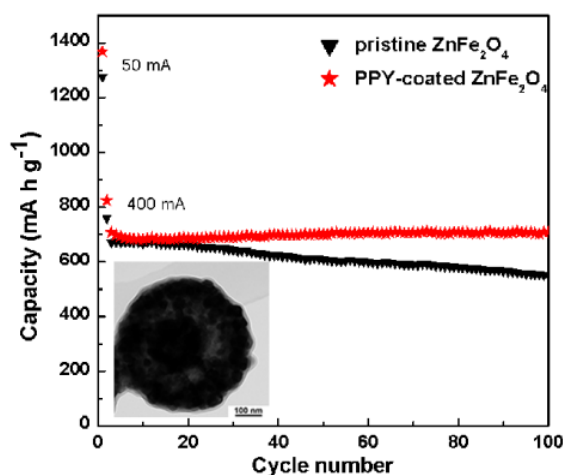
This chapter reports the development of $ZnFe_2O_4$ double-shell hollow microspheres for the accommodation of the large volume expansion during lithiation. A facile and efficient vapor-phase polymerization method has been developed to coat the $ZnFe_2O_4$ hollow spheres with polypyrrole (PPY). The thin PPY coating improves not only the electronic conductivity but also the structural integrity, and thus the cycling stability of the $ZnFe_2O_4$ hollow spheres. Our work sheds light on how to enhance the electrochemical performance of transition metal oxide based anode materials by designing delicate nanostructures. **This work has been published in *Small* (2016, 12 (27), 3732-3737).**

4.1 Introduction

Transition metal oxides (TMOs) have great potential as anode material for lithium-ion battery (LIB) applications.[1] The theoretical capacity of TMOs can reach up to around 1000 mA h g^{-1}, which is approximately two times higher than the commercial graphite (372 mA h g^{-1}). Among the TMOs, iron-based oxides have received particular attention due to high abundance of iron resource, environmentally benign, and low cost. Therefore, α-Fe$_2$O$_3$,[2] Fe$_3$O$_4$,[3] FeO$_x$[4] and spinel ferrite [5] are widely investigated. Zinc ferrite, ZnFe$_2$O$_4$, is a normal "spinel" with Zn ions occupying the tetrahedral sites and Fe ions occupying the octahedral sites. Interestingly, the ZnFe$_2$O$_4$ offers a combination of conversion reaction and alloying-dealloying reaction mechanisms. As a result, each unit formula of ZnFe$_2$O$_4$ is capable of hosting 9 equivalents of Li, leading to a high theoretical capacity of over 1000 mAh g^{-1}. However, like other TMOs, ZnFe$_2$O$_4$ still faces large volume variation during lithiation-delithiation. The large volume variation may cause the notorious problems of active material pulverization and electrode disintegration, leading to rapid capacity decay. In addition, the repetitive volume expansion and contraction may broke the passivating solid electrolyte interphase (SEI) layer and re-expose the fresh electrode surface to the electrolyte, resulting in new SEI formation. During continuous SEI formation, the electrolyte and lithium ions are consumed. Besides the volume variation, the ZnFe$_2$O$_4$ also suffer from poor electrical conductivity, which limits its rate capability. Before practical application in LIBs, the above-mentioned bottlenecks of ZnFe$_2$O$_4$ should be overcome.

Constructing hollow structures have been recognized as a promising strategy to address the volume variation issue. One key feature of the hollow structure is the interior void.[6] The extra space is capable of accommodating the volume variation and alleviating the structural strain during cycling. In addition, the hollow structure is usually composed of nanoparticulate thin shells, which provide short pathways for lithium ion/electron diffusion.[7] Another advantage of the hollow structure is the high surface to volume ratio. The high specific surface area enables a high electrode-electrolyte contact area, facilitating the electrochemical reaction. Guo et al. reported the hydrothermal synthesis of hollow spherical ZnFe$_2$O$_4$ with enhanced specific capacity and capacity retention.[8] Hollow ZnFe$_2$O$_4$ microcubes were reported by Yu et al. via metal organic framework self-sacrificial strategy for lithium storage application.[9] Recently, we reported a facile spray drying method for the low-cost and large-scale synthesis of α-Fe$_2$O$_3$ and ZnFe$_2$O$_4$ multi-shelled hollow spheres.[2] Kang et al. extended this method to the synthesis of ZnFe$_2$O$_4$ yolk-shell structures by replacing the sucrose with dextrin or other carbon sources.[10] The resultant ZnFe$_2$O$_4$ yolk-shell structures show superior structural stability and electrochemical performance than the solid counterparts. Despite

these advances, the cycling performance of $ZnFe_2O_4$ hollow structures remain unsatisfactory, mainly due to their insufficient structural stability and conductivity.

Nanocompositing is known as a promising approach for structural stabilization. By employing a second component as the protective coating layer or matrix, the volume variation of the TMOs can be alleviated, and thus the structural stability can be effectively enhanced. Carbon is the most frequently employed coating layer or matrix due to its high conductivity, easy synthesis, and low cost. Passerini et al. reported the synthesis of $ZnFe_2O_4$/C composites with excellent electrochemical performance in both half cells and full cells.[11] Jiang et al. reported in situ crafting $ZnFe_2O_4$/carbon nanocomposites for anode materials in lithium ion battery.[12] Besides amorphous carbon, carbon nanotube, carbon nanofiber, graphite and graphene have also been used to couple with $ZnFe_2O_4$.[13]

The integration of hollow structuring and nanocompositing offers the opportunity to address the volume variation and poor conductivity issues of TMOs simultaneously. Deng et al. reported the solvothermal synthesis of $ZnFe_2O_4$/C hollow spheres with improved capacity.[14] Huang et al. reported the fabrication of $ZnO/ZnFe_2O_4$/C hollow octahedra by thermal decomposition of Zn and Fe containing metal organic frameworks.[15] However, the synthesis of $ZnFe_2O_4$/C composites usually requires high temperature treatment to achieve carbonization, during which the $ZnFe_2O_4$ tend to react with carbon and form residues. Considering this drawback, conductive polymers (such as PPY), have been considered as alternative coating layers or matrices to couple with $ZnFe_2O_4$.[16] Nevertheless, to the best of our knowledge, there is no report on the synthesis or electrochemical performances of hollow structured $ZnFe_2O_4$-PPY composites.

Herein, $ZnFe_2O_4$ double-shelled hollow spheres have been synthesized by a spray drying method; a vapor phase polymerization method has been developed to coat the $ZnFe_2O_4$ hollow spheres with PPY. The PPY coating improves not only the electronic conductivity but also the structural integrity of $ZnFe_2O_4$. When evaluated as the anode in LIBs, the PPY coated $ZnFe_2O_4$ hollow spheres ($ZnFe_2O_4$-PPY) manifest significantly improved cycling stability and rate capability than the pristine $ZnFe_2O_4$ hollow spheres.

4.2 Results and discussion

4.2.1 Structure Characterization

Figure 4.1 shows the schematic illustration for the synthesis of $ZnFe_2O_4$ double-shelled hollow spheres and the $ZnFe_2O_4$-PPY. First, micrometer-sized precursor spheres were prepared by spray drying the zinc nitrate, iron nitrate and sucrose solution. The as-obtained microspheres were annealing in air, during which the temperature gradient along the radial direction leads to the formation of $ZnFe_2O_4$ double-shelled hollow spheres as we reported previously.[2] The $ZnFe_2O_4$

hollow spheres were then subjected to vapor phase PPY coating. Taking advantage of the low vapor pressure of pyrrole, the pyrrole molecules evaporate and reach the surface of $ZnFe_2O_4$ hollow spheres. In the presence of catalyst ($FeCl_3$), the pyrrole monomers in situ polymerize into PPY, leading to the formation of $ZnFe_2O_4$-PPY. During the vapor phase polymerization, the color of the $ZnFe_2O_4$ hollow spheres gradually changes from orange to black (Figure 4.S1, supporting information), indicating the successful coating of PPY on the surface.
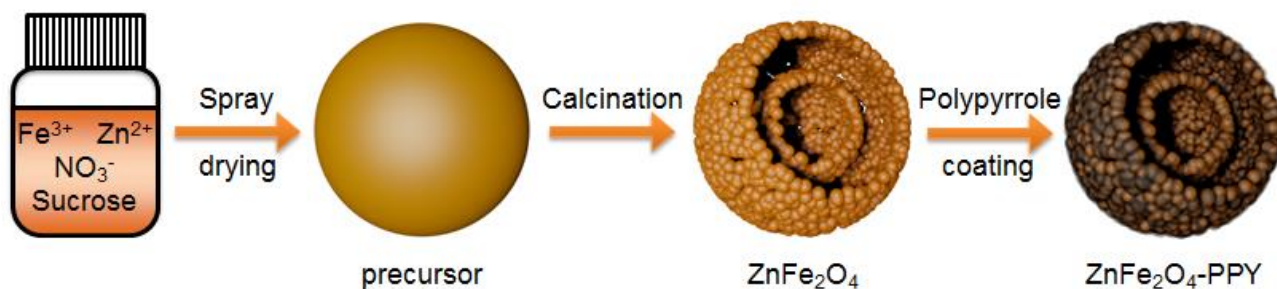
Figure 4.1 Schematic illustration for the synthesis of pristine $ZnFe_2O_4$ and $ZnFe_2O_4$-PPY.

The morphology and structure of pristine $ZnFe_2O_4$ and $ZnFe_2O_4$-PPY are characterized using SEM and TEM. The pristine $ZnFe_2O_4$ are composed of microspheres with sizes of 500 – 2000 nm (Figure 4.S2a and 4.S2b). Most of the microspheres have a double-shelled hollow structure and each shell is constructed by numerous nanosized primary particles (Figure 4.S2c and 4.S2d). The randomly stack of the primary particles leaves a considerable amount of interparticle voids and gives rise to a BET surface area of 17.8 m^2/g (Figure 4.S3). Such a nanoporous feature makes the entire surface accessible to pyrrole, facilitating the subsequent vapor phase polymerization process.

After PPY coating, the $ZnFe_2O_4$-PPY composites well inherit the microspherical morphology of the pristine $ZnFe_2O_4$ (Figure 4.2a and 4.2b). A thin, uniform, and conformal PPY coating with a thickness of 5 – 10 nm can be clearly observed on the surface of $ZnFe_2O_4$ (Figure 4.2c and 4.2d). Energy dispersive X-ray spectroscopy element mapping results (Figure 4.S4) show that C and N are homogeneously distributed throughout the whole particle, further demonstrating the uniform coating of PPY over the yolk-shell structure. The selected area electron diffraction (SAED) of the $ZnFe_2O_4$-PPY shows a series of discontinuous concentric rings, indicating the polycrystalline characteristic of the sample (Figure 4.2d inset). From inside to outside, the diffraction rings can be indexed to the (220), (311), (400), (511) and (440) diffractions of $ZnFe_2O_4$, respectively.[17] Under high resolution TEM (HRTEM) image (Figure 4.2e), the {111} atomic spacings of $ZnFe_2O_4$ (0.48 nm) can be clearly distinguished. In addition, the accurate thickness of the PPY coating layer is measured to be 6 nm. For conventional TEM observation, it is difficult to tell whether the inner sphere of $ZnFe_2O_4$-PPY is hollow or solid. To clarify this point, cross-sectional TEM is employed.

From the cross-sectional TEM image as shown in Figure 4.2f, it is unambiguously demonstrated that the inner core of $ZnFe_2O_4$-PPY do has a hollow interior. The thickness of shells is determined to be around 100 nm and the sizes of the primary particles are in the range of 20 – 50 nm.
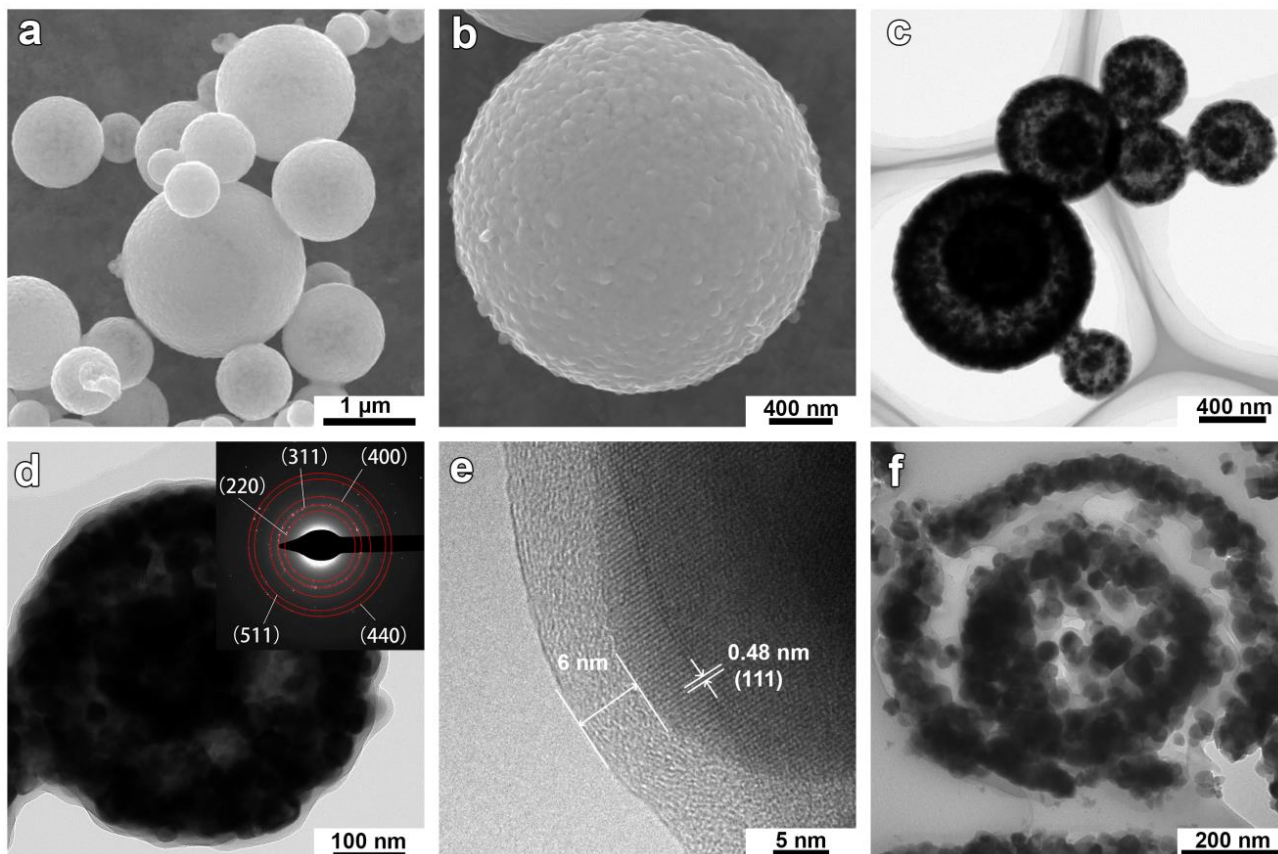
Figure 4.2 a, b) SEM, c, d) TEM, e) HRTEM, and f) cross-sectional TEM images of $ZnFe_2O_4$-PPY.

Wide-angle XRD is utilized to study the crystallographic structure of the samples. The pristine and PPY coated $ZnFe_2O_4$ show quite similar XRD patterns (Figure 4.3 and Figure 4.S5), both of which can be well indexed to the franklinite phase $ZnFe_2O_4$ (JCPDS No.: 22-1012) with cubic spinel structure and $Fd\bar{3}m$ space group. No other peaks can be detected, suggesting the high purity of the products. Despite the nanosized feature, the diffraction peaks show high intensity, indicating the high crystallinity of the $ZnFe_2O_4$ primary particles. The FWHM (full width at half maximum) of the diffraction peaks provides information on the crystallite size. By applying Scherrer's equation to the (311) diffraction peak, the average crystallite size is determined to be 26 nm, in good agreement with the TEM observations.
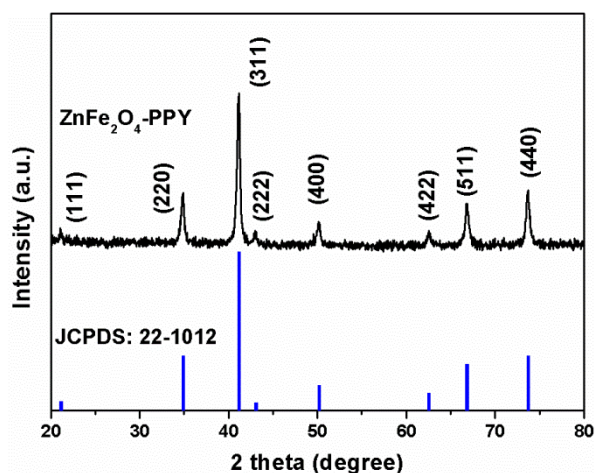
Figure 4.3 XRD pattern of the $ZnFe_2O_4$-PPY.

The presence of PPY in the products is confirmed by Fourier transform infrared (FTIR) spectra (Figure 4.4a). A featureless FTIR spectra without obvious absorption peaks in the range of 800 to 2000 cm^{-1} is obtained for $ZnFe_2O_4$.[18] After PPY coating, the characteristic peaks for PPY can be clearly observed. The peak at 1561 cm^{-1} is due to the C=C vibration of the fundamental pyrrole ring; the peak at 1203 cm^{-1} is attributed to the C-N stretching vibration; the one at 1043 cm^{-1} is ascribed to the =C-H in-plane vibrations; and the bands at 917 and 781 cm^{-1} are resulted from the C-H out-of-plane deformation vibrations of the ring, respectively. All these peaks are in good agreement with the literature results.[19] With the evidence of presence of PPY in the composites, TG analysis in air is employed to quantify the PPY content (Figure 4.4b). The TGA curve of pristine $ZnFe_2O_4$ shows almost no weight loss from room temperature to 600 ℃; however, the $ZnFe_2O_4$-PPY shows two weigh losses. The slight weight loss below 200 ℃ is due to the loss of residual moisture in the sample, while the major weight loss from 250 ℃ to 450 ℃ can be attributed to the combustion of PPY in air. From TGA, the PPY content in the composites is determined to be 10.3 wt. %.
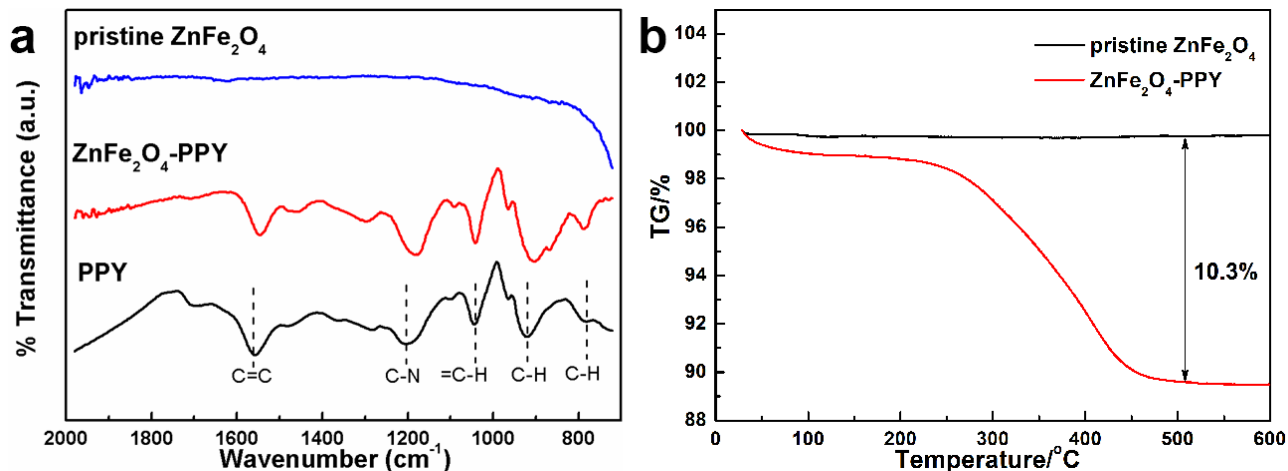
Figure 4.4 a) FTIR spectra and b) TGA curves of $ZnFe_2O_4$ and $ZnFe_2O_4$-PPY.

4.2.2 Electrochemical Performance

The cycling performances of the pristine $ZnFe_2O_4$ and PPY coated $ZnFe_2O_4$ are shown in Figure 4.5a. The half-cells are first activated at the current density of 50 mA g^{-1} for one cycle, followed by galvanostatic charge/discharge at 400 mA g^{-1}. The pristine $ZnFe_2O_4$ delivers an initial discharge capacity of 1275 mA h g^{-1} at 50 mA g^{-1} and a discharge capacity of around 700 mA g^{-1} at 400 mA g^{-1} (Figure 4.S6a). The capacity remains stable in the first 20 cycles and begins to decay after 20 cycles. After 100 discharge-charge cycles, a capacity of 547 mA h g^{-1} is retained, corresponding to a capacity retention of 81% against the third cycle. The $ZnFe_2O_4$-PPY delivers an initial discharge capacity of 1369 mA h g^{-1}. After activation, a stable discharge capacity of around 700 mA h g^{-1} can be achieved at the current density of 400 mA g^{-1}. A discharge capacity of 698 mA h g^{-1} can be maintained after 100 cycles at 400 mA g^{-1}, corresponding to a capacity retention of 98.7% against the third cycle. After 140 cycles, 95% of the third capacity can be retained for $ZnFe_2O_4$-PPY (Figure 4.S7). Besides, the Coulombic efficiency is as high as 99% from the 6th cycle onward (Figure 4.S6b). The improved cycling stability of $ZnFe_2O_4$-PPY can be attributed to the PPY coating, which enhances not only the conductivity but also the structural stability. The morphology of the anode materials before and after cycling is monitored by SEM obervations (Figure 4.S8). Cracked morphology can be observed in the pristine $ZnFe_2O_4$ sample, due to the high volume expansion caused by the valence state change of Fe and Zn during cycling. Comparing with uncoated sample, the $ZnFe_2O_4$-PPY manefests better structural integrity during cycling.
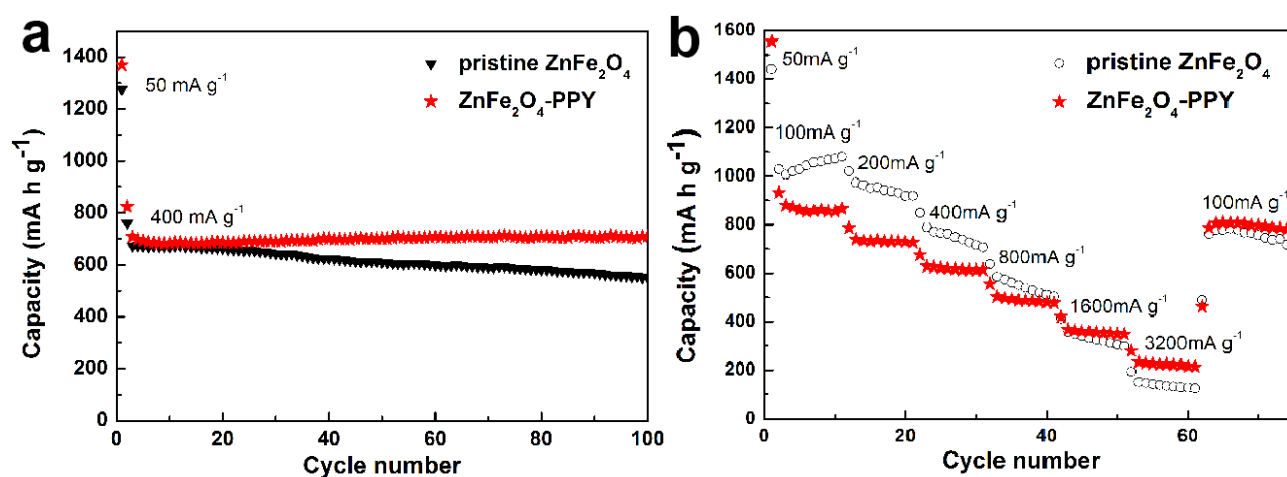
Figure 4.5 a) Cycling performances and b) rate performances of $ZnFe_2O_4$ and $ZnFe_2O_4$-PPY.

The rate performance of $ZnFe_2O_4$-PPY is further evaluated by varying the discharge/charge current density from 100 to 3200 mA g^{-1}. With the increase of current density, the discharge capacity decreases gradually (shown in Figure 4.5b). At the current densities of 100, 200, 400, 800, 1600, and 3200 mA g^{-1}, the specific capacities are 879, 738, 627, 501, 367, and 233 mA h g^{-1}, respectively.

After cycling at various currents, the current density is reduced to 100 mA g^{-1}. A capacity of 805 mA h g^{-1} can be attained, which is 91.6 % of the capacity at the same current before high current test. Comparing with pristine $ZnFe_2O_4$, the $ZnFe_2O_4$-PPY delivers higher specific capacities at high current densities, indicating its better rate capability. The results suggest that the PPY coated $ZnFe_2O_4$ hollow spheres are able to survive the high rate discharge and charge, demonstrating the good structural stability.

EIS measurement is employed to gain further insight into the electrochemical performance (Figure 4.6). Both cells were measured before and after cycling test for 10 times (in the full de-lithiated state). The spectra compose of a semicircle in mid-frequency region and a straight line in low-frequency region. The intercept at x axis represents the ohmic resistance. The depressed semicircle corresponds to the charge transfer resistance. The oblique line relates to the Warburg impedance. Figure 4.6a displays the EIS spectra of the cells before cycling test. The obvious smaller semicircle diameter in Nyquist plots of $ZnFe_2O_4$-PPY indicates a better lithium-ion/electron diffusion in the material because of the higher electric conductivity. From the EIS spectra after cycling test (Figure 4.6b), one can also find that the ohmic resistance is slightly reduced after PPY coating, suggesting the improved electric conductivity. Smaller radius is observed for $ZnFe_2O_4$-PPY, indicating the greatly decreased charge transfer resistance after PPY coating. The decreased ohmic resistance and charge transfer resistance significantly enhances the electrochemical reactions.
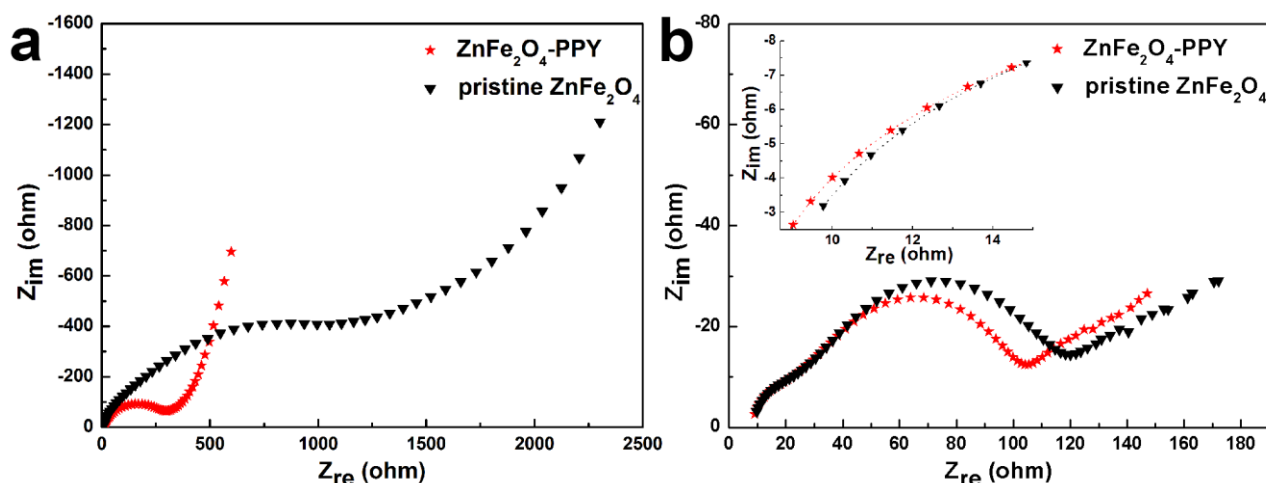
Figure 4.6 EIS spectra a) before cycling and b) after cycling of $ZnFe_2O_4$ and $ZnFe_2O_4$-PPY.

4.3 Conclusions

In conclusion, PPY coated $ZnFe_2O_4$ double-shelled hollow spheres have been successfully synthesized. The resultant $ZnFe_2O_4$-PPY composite uniquely combines the advantages of hollow structuring and nanocompositing. The hollow interior buffers the volume change during charge/discharge, while the PPY coating enhances the structural stability and conductivity.

Compared with pristine $ZnFe_2O_4$ with double-shelled hollow structure, the $ZnFe_2O_4$-PPY composite manifests significantly improved electrochemical performance. Our work demonstrates that the integration of hollow structuring and nanocompositing is an effective strategy to boost the electrochemical performance of TMO based anode materials. This strategy might be generally applied to other high capacity anode materials such as Si, which suffer from large volume change and low conductivity.

4.4 Experimental section

4.4.1 Material Synthesis

$ZnFe_2O_4$ double-shelled hollow spheres were synthesized by a spray drying method followed by calcination in air. Typically, $Fe(NO_3)_3 \cdot 9H_2O$ (6.7 mmol), $Zn(NO_3)_2 \cdot 6H_2O$ (3.3 mmol) and sucrose (10 mmol) were dissolved in water (100 ml). The resulting solution was then spray dried at an inlet temperature of 220 ℃, a pump rate of 1.5 ml/min, and a N_2 gas flow of 60 ml/min. Afterwards, the obtained dry powder was calcined at 400 ℃ for 5h in air with a heating rate of 2 ℃/min to obtain the $ZnFe_2O_4$ hollow spheres.

For the synthesis of $ZnFe_2O_4$-PPY, the $ZnFe_2O_4$ hollow spheres (0.15 g) were immersed in $FeCl_3$ catalyst solution (0.1 ml, 0.3 M) and dried. For PPY coating, a vial containing pyrrole monomer (2 ml) and another vial containing $ZnFe_2O_4$ hollow spheres (0.15 g) were sealed in a blue cap bottle and heated at 50 ℃ for 48h.

4.4.2 Characterization

Fourier transform infrared (FTIR) spectra were carried out on ThermoNicolet Nexus 6700 FTIR spectrometer equipped with diamond crystal. Thermogravimetric (TG) analysis was performed using METTLER TOLEDO TGA/DSC1 STAR^e System from 25 to 600 ℃ in air with a heating rate of 5 ℃/min. Field emission scanning electron microscopy (SEM) images were taken using JEOL 7001. Transmission electron microscopy (HRTEM) images were obtained by Philips Tecnai F20. Cross-section TEM image was taken using JEOL 1010 after embedding the sample in epoxy resin for 48 h and cut into 60 nm thickness slice with a diamond knife. X-ray diffraction (XRD) patterns were carried out using Rigaku Miniflex X-ray Diffractmeter with Co Kα radiation (λ=0.179 nm). Nitrogen sorption isotherm was measured by Tristar II Surface Area and Porosity analyser (Micromeritics). The samples were degassed at 180 ℃ overnight under vacuum.

4.4.3 Electrochemical Measurements

The slurry is comprised of 70 wt. % active material ($ZnFe_2O_4$-PPY or pristine $ZnFe_2O_4$), 20 wt. % carbon black, and 10 wt.% polyvinylidene fluoride (PVDF) binder. The slurry was cast onto Cu foil and dried under vacuum at 120 ℃ overnight. Electrochemical measurements were tested in two-electrode Swagelok type cells. Metallic lithium chips were used as both the counter electrode and reference electrode, 1 M $LiPF_6$ solution in ethylene carbonate (EC)/ethylmethyl carbonate (EMC)/dimethyl carbonate (DEC) (1:1:1 in volume) was used as the electrolyte. The cells were galvanostatically charged/discharged under different current densities using a MTI 8 Channels Battery Analyzer. The specific capacity is calculated based on the total mass of the active materials. Electrochemical Impedance Spectroscopy (EIS) measurements were performed on Solartron 1480 MultiStat instrument in the frequency range of 100 kHz to 0.01 Hz. All measurements were carried out at room temperature.

4.5 Supplementary information
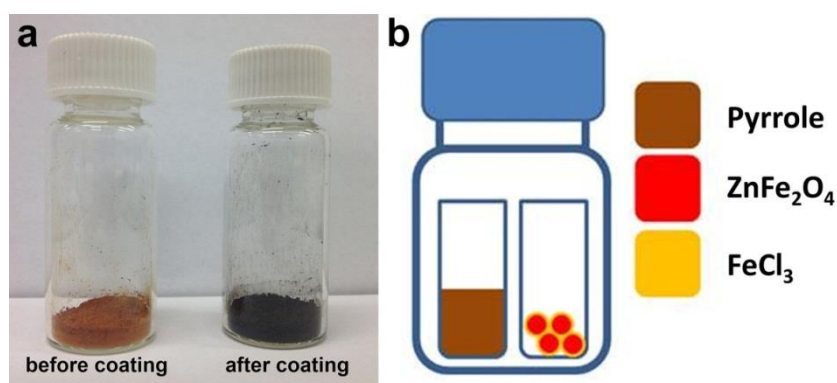
Figure 4.S1 a) Digital photographs of $ZnFe_2O_4$ before and after polypyrrole coating and b) schematic illustration of the device during pyrrole coating process.
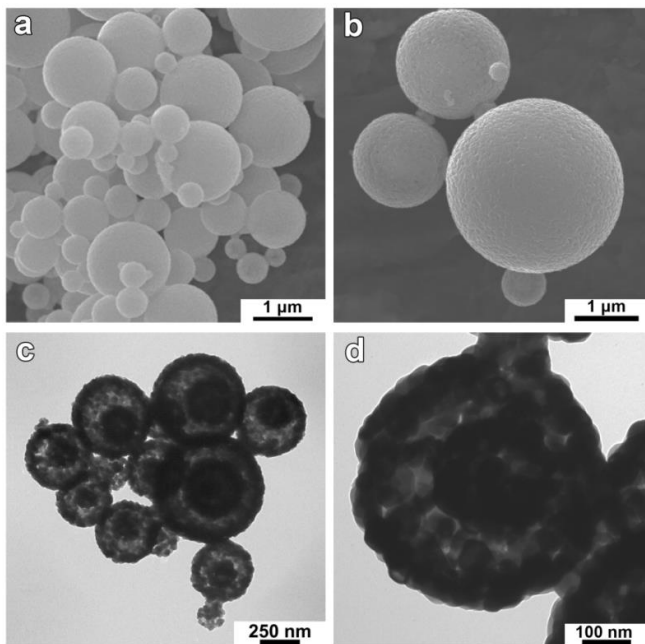
Figure 4.S2 a, b) SEM, c, d) TEM images of pristine $ZnFe_2O_4$ sample.
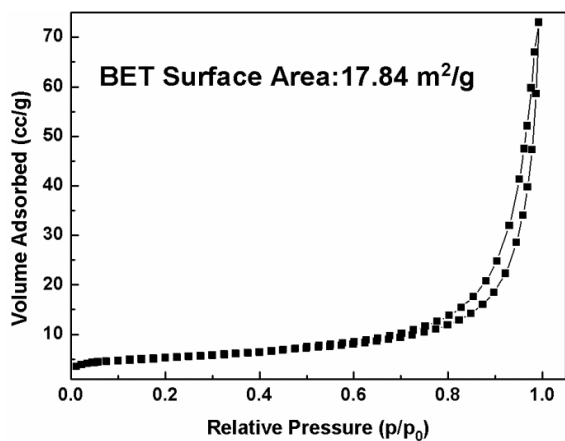
Figure 4.S3 Nitrogen adsorption isotherm of pristine $ZnFe_2O_4$ sample.
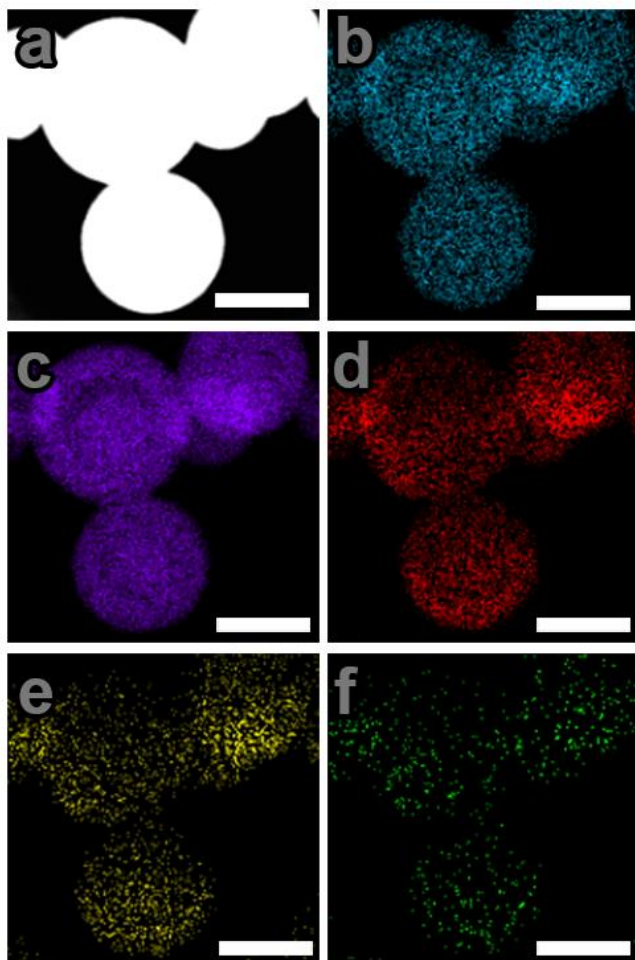
Figure 4.S4 a) STEM image of $ZnFe_2O_4$-PPY spheres and the corresponding b) Zn, c) Fe, d) O, e) C and f) N element maps. The scale bars are 1 μm.
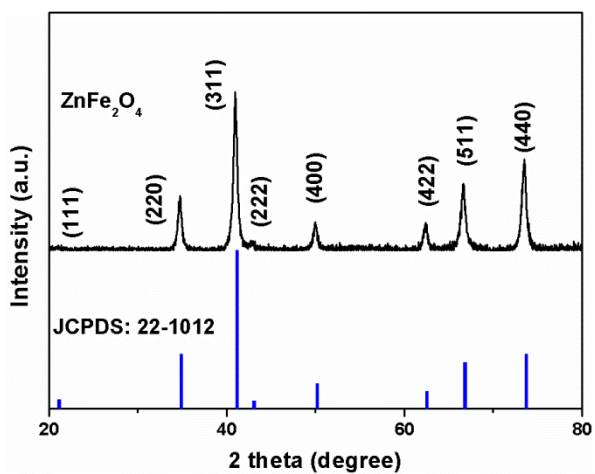
Figure 4.S5 XRD pattern of pristine $ZnFe_2O_4$ sample.
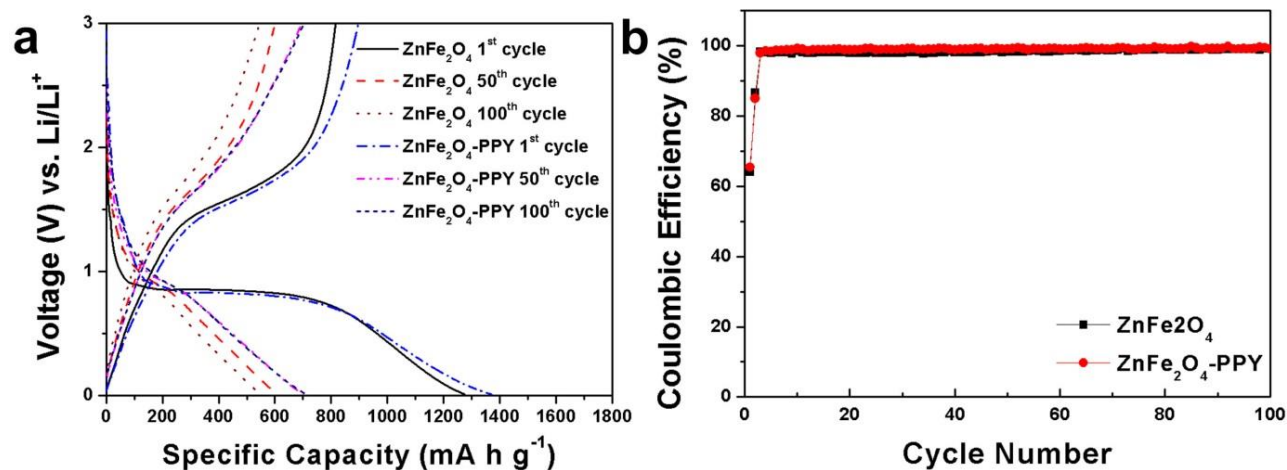
Figure 4.S6 a) Representative charge-discharge profiles of $ZnFe_2O_4$ and $ZnFe_2O_4$-PPY sample and

b) Coulombic Efficiency of $ZnFe_2O_4$ and $ZnFe_2O_4$-PPY sample.
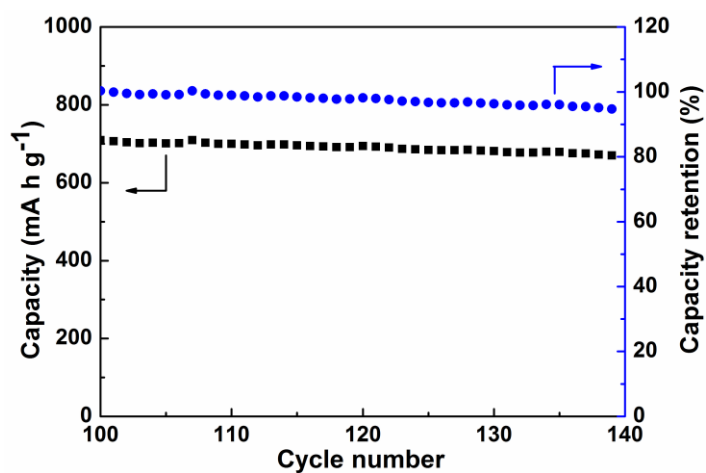
Figure 4.S7 Cycling performance and capacity retention after 100 cycles of $ZnFe_2O_4$-PPY sample.
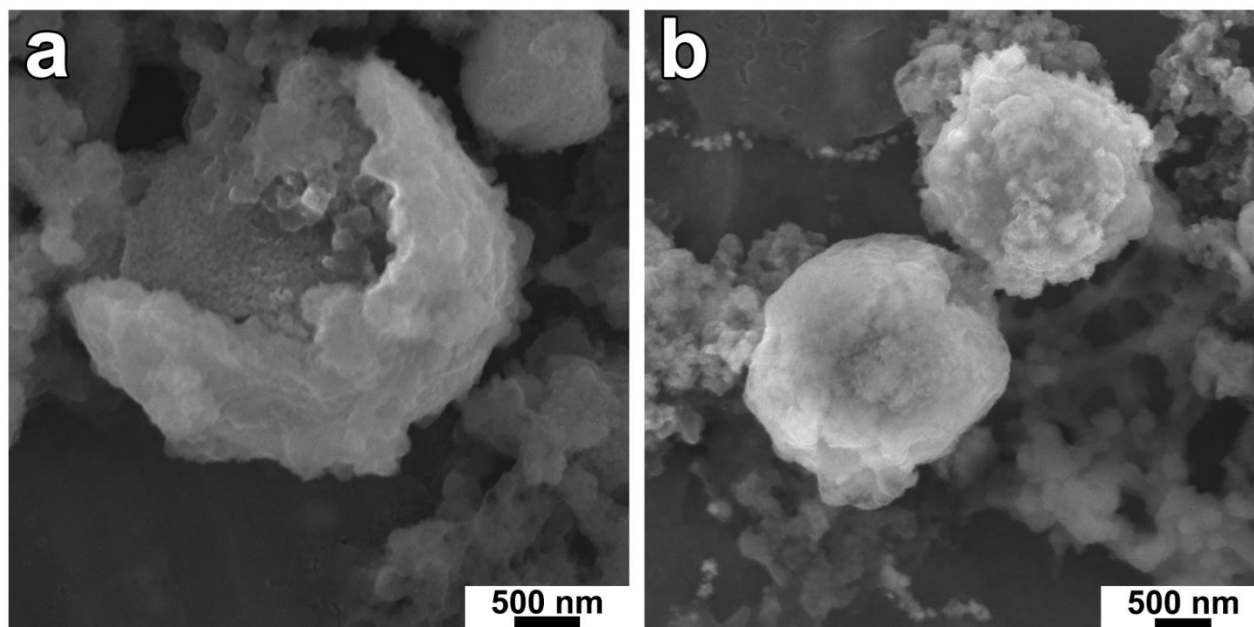
Figure 4.S8 SEM images of a) $ZnFe_2O_4$ and b) $ZnFe_2O_4$-PPY anode material after cycling.

4.6 References

[1]   Poizot, P.; Laruelle, S.; Grugeon, S.; Dupont, L.; Tarascon, J. M., *Nature* **2000**, *407*, 496.

[2]   Zhou, L.; Xu, H.; Zhang, H.; Yang, J.; B. Hartono, S.; Qian, K.; Zou, J.; Yu, C., *Chem. Commun.* **2013**, *49*, 8695.

[3]   a) He, C.; Wu, S.; Zhao, N.; Shi, C.; Liu, E.; Li, J., *Acs Nano* **2013**, *7*, 4459; b) Zhou, G.; Wang, D.-W.; Li, F.; Zhang, L.; Li, N.; Wu, Z.-S.; Wen, L.; Lu, G. Q.; Cheng, H.-M., *Chem. Mater.* **2010**, *22*, 5306.

[4]   Zhang, H.; Zhou, L.; Noonan, O.; Martin, D. J.; Whittaker, A. K.; Yu, C., *Adv. Funct. Mater.* **2014**, *24*, 4337.

[5]   a) Wang, N.; Xu, H.; Chen, L.; Gu, X.; Yang, J.; Qian, Y., *J. Power Sources* **2014**, *247*, 163; b) Xing, Z.; Ju, Z.; Yang, J.; Xu, H.; Qian, Y., *Nano Res.* **2012**, *5*, 477.

[6]   a) Choi, S. H.; Kang, Y. C., *Chem. Eur. J.* **2014**, *20*, 5835; b) Park, G. D.; Lee, J.-H.; Lee, J.-K.; Kang, Y. C., *Nano Res.* **2014**, *7*, 1738.

[7]   a) Wang, Z.; Zhou, L.; Lou, X. W., *Adv. Mater.* **2012**, *24*, 1903; b) Yao, L.; Hou, X.; Hu, S.; Ru, Q.; Tang, X.; Zhao, L.; Sun, D., *J. Solid State Electrochem.* **2013**, *17*, 2055.

[8]   Guo, X.; Lu, X.; Fang, X.; Mao, Y.; Wang, Z.; Chen, L.; Xu, X.; Yang, H.; Liu, Y., *Electrochem. Commun.* **2010**, *12*, 847.

[9]   Yu, H.; Fan, H.; Yadian, B.; Tan, H.; Liu, W.; Hng, H. H.; Huang, Y.; Yan, Q., *ACS Appl. Mater. Interfaces* **2015**, *7*, 26751.

[10]   Won, J. M.; Choi, S. H.; Hong, Y. J.; Ko, Y. N.; Kang, Y. C., *Sci. Rep.* **2014**, *4*, 5857.

[11]   a) Bresser, D.; Paillard, E.; Kloepsch, R.; Krueger, S.; Fiedler, M.; Schmitz, R.; Baither, D.; Winter, M.; Passerini, S., *Adv. Energy Mater.* **2013**, *3*, 513; b) Varzi, A.; Bresser, D.; von Zamory, J.; Muller, F.; Passerini, S., *Adv. Energy Mater.* **2014**, *4*, 1.

[12]   Jiang, B.; Han, C.; Li, B.; He, Y.; Lin, Z., *Acs Nano* **2016**, *10*, 2728.

[13]   a) Sui, J.; Zhang, C.; Hong, D.; Li, J.; Cheng, Q.; Li, Z.; Cai, W., *J. Mater. Chem.* **2012**, *22*, 13674; b) Kong, J.; Yao, X.; Wei, Y.; Zhao, C.; Ang, J. M.; Lu, X., *RSC Adv.* **2015**, *5*, 13315; c) Yao, L.; Hou, X.; Hu, S.; Tang, X.; Liu, X.; Ru, Q., *J. Alloys Compd.* **2014**, *585*, 398; d) Xie, J.; Song, W.; Cao, G.; Zhu, T.; Zhao, X.; Zhang, S., *RSC Adv.* **2014**, *4*, 7703; e) Chen, X.; Cheng, B.; Xu, H.; Yang, J.; Qian, Y., *Chem. Lett.* **2012**, *41*, 639; f) Liu, L.; Gao, R.; Sun, L.; Han, S.; Chen, D.; Hu, Z.; Liu, X., *New J. Chem.* **2016**, *40*, 3139; g) Xia, H.; Qian, Y.; Fu, Y.; Wang, X., *Solid State Sci.* **2013**, *17*, 67.

[14]   Deng, Y.; Zhang, Q.; Tang, S.; Zhang, L.; Deng, S.; Shi, Z.; Chen, G., *Chem Commun (Camb)* **2011**, *47*, 6828.

[15]   Zou, F.; Hu, X.; Li, Z.; Qie, L.; Hu, C.; Zeng, R.; Jiang, Y.; Huang, Y., *Adv. Mater.* **2014**, *26*, 6622.

[16]   Li, Y.; Yi, R.; Yan, A.; Deng, L.; Zhou, K.; Liu, X., *Solid State Sci.* **2009**, *11*, 1319.

[17]   Darshane, S. L.; Deshmukh, R. G.; Suryavanshi, S. S.; Mulla, I. S., *J. Am. Ceram. Soc.* **2008**, *91*, 2724.

[18]   Laokul, P.; Amornkitbamrung, V.; Seraphin, S.; Maensiri, S., *Curr. Appl Phys.* **2011**, *11*, 101.

[19]   a) Han, F.; Li, D.; Li, W.-C.; Lei, C.; Sun, Q.; Lu, A.-H., *Adv. Funct. Mater.* **2013**, *23*, 1692; b) Sevilla, M.; Valle-Vigón, P.; Fuertes, A. B., *Adv. Funct. Mater.* **2011**, *21*, 2781; c) Li, X.-G.; Wei, F.; Huang, M.-R.; Xie, Y.-B., *J. Phys. Chem. B* **2007**, *111*, 5829.

Chapter 5

Nitrogen-Doped Mesoporous Carbon Microspheres by Spray Drying-Vapour Deposition for High-Performance Supercapacitor
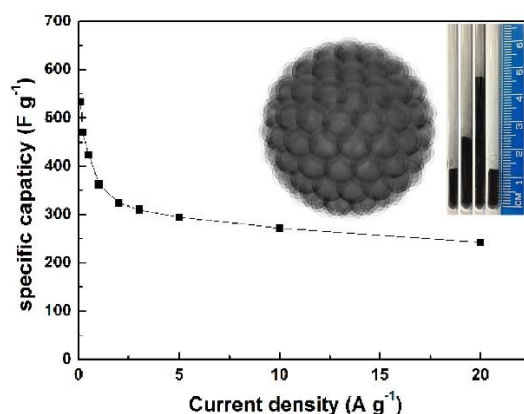
In this chapter, N-doped mesoporous carbon microspheres have been synthesized via a spray drying-vapour deposition method. The resultant mesoporous carbon microspheres possess a mesopore-dominate high surface area, an increased apparent density, thin walls with high nitrogen content, and superior gravimetric/volumetric capacitance. This work is the first report via spray drying-vapour deposition method using commercial Ludox silica nanoparticles as hard templates for EDLCs.

5.1 Introduction

Electric double layer capacitors (EDLCs), also known as supercapacitors, are appealing power sources for consumer electronics and uninterruptible power supplies owing to their high power density, rapid charge/discharge, environmental friendliness, and long cycling life.[1] Porous carbon materials have attracted tremendous attention as electrode materials for supercapacitors because of their high specific surface area, high conductivity, high chemical stability and tunable porous structures.[2] Microporous carbons with pore sizes smaller than 2 nm and high surface areas have been widely utilized in EDLCs.[3] It was found that the capacitance reached a plateau when the microporous surface area went above 1500 m^2/g,[4] indicating that the total surface area measured by gas sorption methods is not fully electrochemically accessible. The partially inaccessible small micropores also decreased the rate performance of microporous carbon.[5] In the past decades, mesoporous carbon materials with pore sizes of 2-50 nm have become promising candidates for EDLC applications. Huang et al. demonstrated that the capacitance normalized by surface area was higher in mesoporous carbon compared to microporous carbon in aqueous solutions, suggesting a high capacitance can be achieved in carbon materials with high mesoporous surface area.[6] Qian et al. reported the synthesis of mesoporous carbon with a high BET surface area of 1300 m^2/g and a high percentage of mesopore surface area (1200 m^2/g). This material showed a high capacitance of 340 F/g at 1 A/g and 66% capacity retention at 10 A/g due to the small pore size of 2-3 nm.[7] Li et al. reported the fabrication of protein-derived carbons with a high mesopore surface area percentage of ~93% but a relatively small total surface area of 810 m^2/g.[8] There are few reports on the synthesis of mesoporous carbons with large mesopores and high mesopore surface areas (>1400 m^2/g) for supercapacitor applications.

In general, mesoporous carbons can be synthesized through soft-templating or hard-templating methods.[9] Surfactant molecules are generally used in the soft-templating method[10] and in the synthesis of mesoporous silicas as templates in the hard-templating approach.[11] Instead of surfactants, using commercial Ludox silica nanoparticles as porogens is a convenient approach for the surfactant-free synthesis of mesoporous carbon.[12] However, the synthesis was usually conducted in solutions,[13] resulting in carbon materials with undefined morphology and relatively low packing density, unfavorable for the volumetric performance of EDLCs.[14] The packing density can be improved by controlling the morphology. Cui et al. reported the synthesis of porous carbon microspheres with increased packing density because small-sized spheres can be accommodated into the packing voids of large-sized spheres.[15] However, oil/water microemulsion was applied in the morphology control, not suitable for scalable synthesis. Spray drying, on the other hand, is a facile method for the synthesis of multi-shelled metal oxides[16] and the assembly of colloidal silica

nanoparticles into microspheres.[17] When Ludox silica templates, resorcinol and formaldehyde as carbon precursors were used via the spray drying method, silica/polymer microspheres and subsequently mesoporous carbon microspheres were synthesized,[18] with a surface area below 1200 m^2/g. Wang et. al reported the synthesis of a partially graphitized porous carbon by spray drying Ludox silica with sucrose.[19] However, the capacitance of the obtained carbon microspheres is only 91 F/g at 10 mV/s due to the presence of a high proportion of micropores.

The choice of carbon precursors is crucial for replicating the template morphology with a homogenous carbon layer. Compared to resorcinol/formaldehyde or sucrose used in conventional infiltration and polyfurfuryl alcohol used in high-temperature chemical vapour deposition (CVD),[20] volatile precursors such as pyrrole applied in low-temperature vapour deposition achieved a uniform coating and maintained the structural stability of the template.[21] The high nitrogen content coming from carbonized polypyrrole contributed further to pseudo-capacitance and improved the overall capacitance of carbon materials.[22] Ferrero and co-workers reported the preparation of N-doped hollow carbon nanospheres using vapour deposition of pyrrole on preformed silica nanoparticles, which have a faithfully replicated morphology of the silica template but a low packing density.[23] It remains a challenge to use a convenient approach and synthesize mesoporous carbon microspheres with a high packing density, large mesopores and high mesopore surface areas for supercapacitors.

Herein, we report the preparation of nitrogen-doped mesoporous carbon microspheres by a spray drying-vapour deposition method for the first time, using commercial Ludox colloidal silica nanoparticles as porogens. The resultant mesoporous carbon microspheres have a mesopore-dominant (95%) high surface area (1528 m^2/g) with 8 At% nitrogen doping, an increased apparent density, and consequently excellent gravimetric/volumetric performance as an electrode material in EDLCs.

5.2 Results and discussion

Nitrogen-doped mesoporous carbon microspheres were synthesized by a spray drying - vapour deposition process (Figure 5.1a). Typically, commercially available colloidal silica nanoparticles (Ludox SM) with a diameter of around 7 nm (Figure 5.S1a, 1b) were dispersed in water. The suspension was atomized in the chamber of a spray drier, forming microspheres under contraction force. As a catalyst, iron chloride was added to the silica/water suspension and embedded in microspheres after spray drying for the oxidative polymerization of pyrrole. Then, pyrrole vapour was introduced to form a thin layer of polypyrrole coating on silica nanoparticles. After carbonization at 800 ℃ in a nitrogen atmosphere and removing sacrificial silica template, N-doped

mesoporous carbon microspheres were obtained (named as MC-7-SD). In order to highlight the advantage of spray drying method, silica aggregates were also synthesized using air-drying[24] and freeze-drying[25] methods as reported in the literature for comparison. The resultant mesoporous carbons after 800 ℃ carbonization and etching were denoted as MC-7-AD and MC-7-FD, respectively.
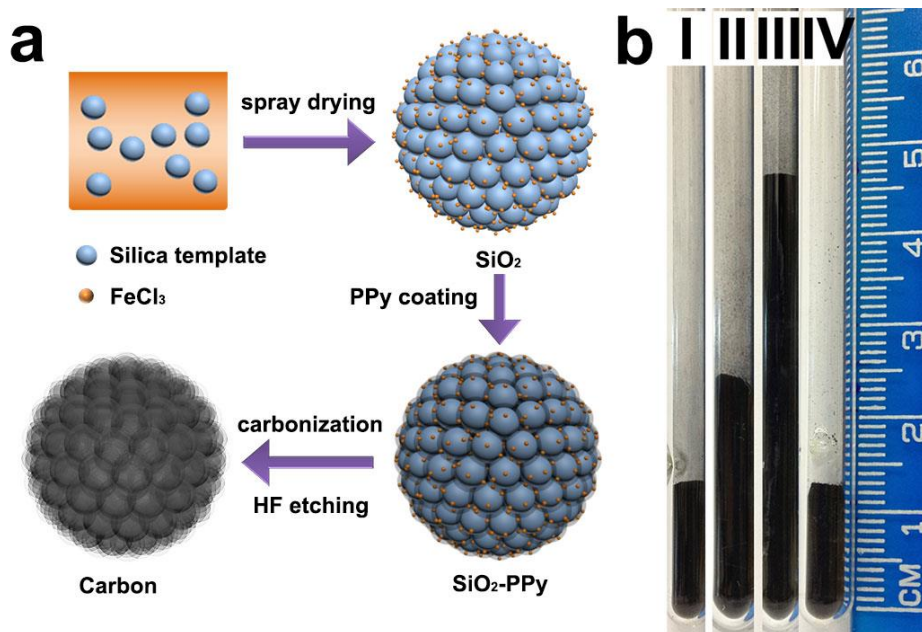
Figure 5.1 a) Illustration of the synthesis approach of MC-7-SD, b) the apparent density of I) MC-7-SD, II) MC-7-AD, III) MC-7-FD and IV) activated carbon materials. The mass of each material is 50 mg.

The apparent densities of MC-7-SD, MC-7-AD and MC-7-FD were measured as reported in the literature[26] and are shown in Figure 5.1b. MC-7-SD shows a higher apparent density (0.50 g/cm^3) compared to MC-7-AD (0.31 g/cm^3) and MC-7-FD (0.15 g/cm^3), slightly lower than that of a commercial activated carbon (0.54 g/cm^3). The obvious difference in apparent densities is explained in scanning electron microscopy (SEM) observations. The low magnification SEM image (Figure 5.2a) reveals that MC-7-SD has a micro-sized spherical morphology with a particle size of 700-5000 nm (Figure 5.S1c). The invagination zones on the granules are probably caused by temperature[27] and/or the polydispersity of constituent nanoparticles[28] during rapid spray drying. It is reported that the spherical morphology exhibits a higher packing density compared to other morphologies because the packing voids from large spheres accommodate smaller ones.[29] For comparison, MC-7-AD and MC-7-FD show fragmented morphologies with random particle packing (Figure 5.2b and Figure 5.2c), leading to lower packing densities.

Transmission electron microscopy (TEM) was used to reveal the mesostructure of MC-7-SD, MC-7-AD, and MC-7-FD. TEM image of MC-7-SD (Figure 5.2d) shows a mesoporous micro-spherical

morphology. As shown in Figure 5.2d inset, the thickness of the mesoporous carbon wall is around 1.8 nm. Different from MC-7-SD, the morphologies of MC-7-AD and MC-7-FD samples are monoliths with rich mesopores (Figure 5.2e and Figure 5.2f). After measurement from the inset high magnification TEM images, the mesopore sizes in MC-7-AD and MC-7-FD are 7-8 nm, and the thicknesses of carbon layers are 3.0 and 3.1 nm, respectively.
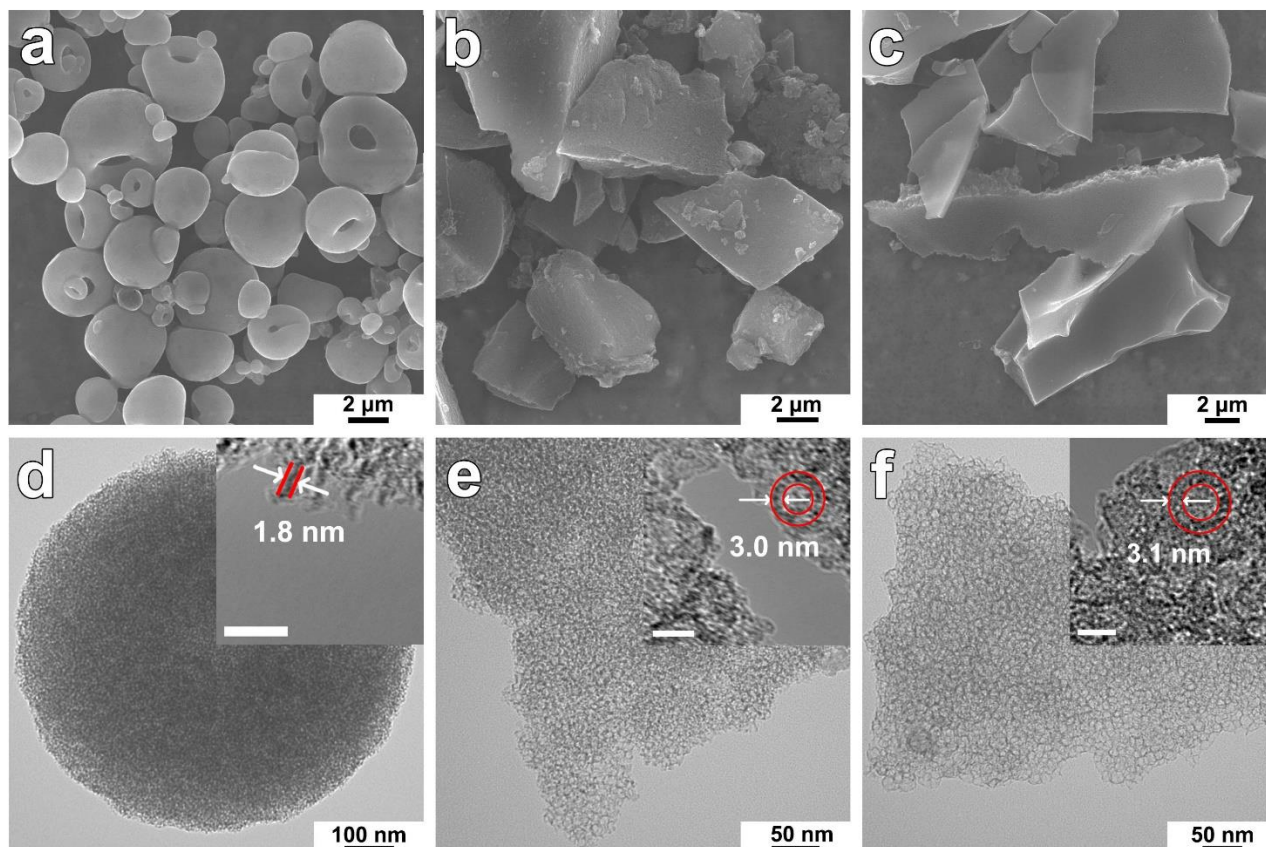
Figure 5.2 a-c) SEM and d-f) TEM images of MC-7-SD, MC-7-AD, and MC-7-FD, respectively. d-f) insets are HRTEM images of the edge of MC-7-SD, MC-7-AD, and MC-7-FD, respectively. The scale bars in insets are 10 nm.

To fully characterize the porous structure of mesoporous carbon materials, nitrogen sorption analysis was employed. As shown in Figure 5.3a, all three samples show typical IV isotherms with H2 hysteresis loops. The adsorption branches of MC-7-AD and MC-7-FD show major capillary condensation steps in relative pressure (P/P_0) range of 0.7-0.8 and > 0.9, indicating the existence of large mesopores and packing voids. The adsorption isotherm of MC-7-SD shows a capillary condensation step at a relatively lower P/P_0 of 0.6-0.75, indicating a relatively small pore size. No capillary condensation is observed at $P/P_0 > 0.9$, suggesting small-sized spheres accommodates into the packing voids of large-sized spheres. The pore size distributions (PSD) calculated by Barrett–Joyner–Halanda (BJH) model from adsorption branches are shown in Figure 5.3b. The PSD of MC-7-AD and MC-7-FD show a peak centred at 7 nm, which is close to the size of Ludox silica

templates (Figure 5.S1a, 1b). A shoulder peak at 2-5 nm can also be observed. Unlike MC-7-AD and MC-7-FD, MC-7-SD shows a wide PSD in the range of 2-9 nm.
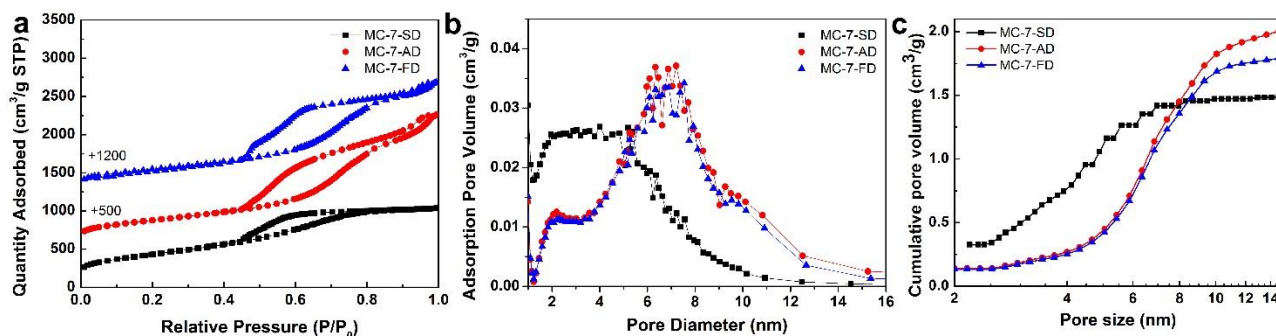
Figure 5.3 a) Nitrogen adsorption/desorption isotherm, b) pore size distribution curves and c) cumulative pore volume-pore size plots of MC-7-SD, MC-7-AD, and MC-7-FD.

As summarized in Table. 5.1, the total pore volume of MC-7-AD, MC-7-FD and MC-7-SD are 2.7, 2.3 and 1.6 cm^3/g, respectively. MC-7-SD shows the lowest total pore volume because all pore volume is attributed by mesopores, while the total pore volumes of MC-7-AD and MC-7-FD are combinations of mesopores and packing voids. In order to differentiate the contribution of pore volume from mesopores with different sizes, the pore volume of specific pore size range is calculated from the cumulative pore volume-pore size plots (Figure 5.3c). In MC-7-SD sample, 55% of total pore volume (0.8 cm^3/g) was attributed to mesopores with sizes of 2-5 nm, while only 20% of pore volume (0.3 cm^3/g) came from mesopores with sizes of 5-9 nm (Table. 5.1). On the contrary, 0.3 cm^3/g of pore volume of MC-7-AD and MC-7-FD was attributed to 2-5 nm mesopores (12% and 14%, respectively), and the majority of pore volume come from mesopores with sizes of 5-9 nm (1.3 cm^3/g (52%) and 1.2 cm^3/g (59%), respectively). MC-7-SD also shows the highest Brunauer-Emmett-Teller (BET) surface area (1528 m^2/g, Table. 5.1) with an extraordinary mesoporous surface ratio (95%) compared to MC-7-AD and MC-7-FD (1338 m^2/g and 1229 m^2/g, respectively).

Table. 5.1 Textural properties of MC-7-SD, MC-7-AD, MC-7-FD and activated carbon.

Sample	S_{BET} (m^2/g)	S_{micro} (m^2/g)	S_{meso} (m^2/g)	V_t (cm^3/g)	$V_{2-5\,nm}$ (cm^3/g)	$V_{5-9\,nm}$ (cm^3/g)
MC-7-SD	1528	69	1459	1.6	0.8	0.3
MC-7-AD	1338	55	1338	2.7	0.3	1.3
MC-7-FD	1229	66	1229	2.3	0.3	1.2
Activated carbon	840	498	342	0.8	-	-

Note: S_{BET} is BET surface area calculated from P/P_0=0.05-0.3, S_{micro} is t-plot micropore area, S_{meso} is mesopore area calculated from equation $S_{meso}=S_{BET}-S_{micro}$, V_t is total pore volume at P/P_0=0.995, $V_{a-b\ nm}$ is the pore volume in the range of a-b nm, which is calculated from the cumulative pore volume.

To investigate the formation of mesopores with sizes of 2-5 nm in MC-7-SD, MC-7-AD, and MC-7-FD, X-ray photoelectron spectroscopy (XPS) was conducted to analyze the Fe concentration on the surface of as-dried microspheres/aggregates. XPS spectra (Figure 5.S2) show the Fe/SiO$_2$ molar ratios of the as-dried aggregates are 3.4% and 3.6% after air-drying and freeze-drying method, respectively, similar to the feeding ratio in silica/water suspension (3.7%). However, the Fe/SiO$_2$ molar ratio of the as-dried microspheres after spray drying reduces to 1.1 %, which is caused by the loss of Fe catalyst carried by inlet gas during spray drying.[30] As previously reported, the reduction of Fe catalyst results in less polypyrrole coated on the surface of spray-dried microspheres.[31] The thermal gravimetric (TG) analysis of SiO$_2$/C composites after carbonization (Figure 5.S3) further supported our conclusion. The composite after spray-drying method shows 9.5 wt.% carbon, lower than those after air-drying (12.9 wt.%) and freeze-drying methods (13.0 wt.%). The smaller carbon coating amount is in accordance with the thinner carbon layer observed from HRTEM. It is reported that thin carbon layer ends up in an invaginated morphology with reduced pore size after etching.[32] The nitrogen sorption results show that the size-reduced mesopores exist in MC-7-SD, MC-7-AD, and MC-7-FD. With a thinner carbon layer, MC-7-SD exhibits a higher proportion of small-sized (2-5 nm) mesopores compared to MC-7-AD and MC-7-FD.

In order to investigate the structural change of mesoporous carbon microspheres as a function of carbonization temperature, MC-7-SD was carbonized at 650, 800 and 950 ℃. As shown in Figure 5.S4, a typical mesoporous micro-spherical morphology is well maintained despite various temperatures. A slight increase of the specific surface area and pore volume was observed with the rising of carbonized temperature (Table. 5S1). The increase in specific surface area and pore volume is similar to a previous report,[10a] which is mainly due to the higher degree of carbonization at increased temperature. Raman spectra (Figure 5.S5) show the graphitization of mesoporous carbons. The distinguishable peak at 1360 cm^{-1} (D band) is associated with the structural imperfections due to the lack of long-range order in amorphous and quasi-crystalline forms of carbon materials; meanwhile, the peak at 1592 cm^{-1} (G band) corresponds to the E$_{2g}$ species (stretching vibrations) of the infinite crystalline graphite.[33] The intensity ratio between D and G band (I$_D$/I$_G$) provides a meaningful index for the crystallinity of carbon material. The I$_D$/I$_G$ ratio slightly decreases from 0.90 to 0.88 with the increase of the carbonization temperature from 650 to

950 ℃, which is attributed to the increasing crystallinity of carbon at higher carbonization temperature.

The nitrogen doping contents of MC-7-SD samples carbonized at 650, 800, and 950 ℃ were also investigated. The XPS survey spectra (Figure 5.S6) show the surface chemistry is dominated by C, O, and N for all mesoporous carbons, and the N content decreases from 13.21 to 5.57 At% with the ascending temperature from 650 to 950 ℃. NCHS elemental analysis (Table. 5S2) was conducted to determine the nitrogen content in bulk material. It is also shown that the nitrogen content in MC-7-SD samples decreases from 13.29 to 6.47 wt.% when the carbonization temperature increases from 650 to 950 ℃, which is attributed to the decomposition of N-containing functional groups at elevated temperatures.[10a]

The capacitive performances of MC-7-SD carbonized at 650, 800, and 950 ℃ were tested in 6 M KOH (Figure 5.S7). The charge-discharge curves of three samples exhibit a typical EDLC behavior with triangular shapes. As mentioned before, MC-7-SD carbonized under higher temperature possesses a better crystallinity, but the N-doping content is decreased. Consequently, the capacitance of MC-7-SD is the lowest (242.5 F/g) carbonized at 650 ℃ and the highest (362.8 F/g) at 800 ℃. Further increasing the carbonization temperature to 950 ℃ leads to decreased capacitance of 330.1 F/g (all at 1 A/g). For this reason, 800 ℃ is chosen as the optimized carbonization temperature of MC-7-SD, MC-7-AD, and MC-7-FD in the following studies.

Regardless of various drying method during synthesis, elemental analysis reveals that MC-7-SD, MC-7-AD, and MC-7-FD show similar nitrogen content after 800 ℃ carbonization (Table. 5.2). XPS results further confirmed that about 8 At% nitrogen is accommodated in mesoporous carbons. Commonly, the high-resolution N1s spectra (Figure 5.4) include pyridinic-N (398.3±0.1 eV), pyrrolic-N (399.7±0.1 eV), quaternary-N (400.9±0.1 eV), and pyridine N-oxide (402.2±0.3 eV). Quaternary-N, also known as graphitic-N, has higher thermal stability by incorporating N atoms into graphitic carbon plane and bonded with three sp^2 carbon atoms. As shown in Table. 5.2, MC-7-SD, MC-7-AD, and MC-7-FD samples possess 30.09%, 40.61%, and 39.65% of quaternary-N, respectively. The high proportions of quaternary-N in polypyrrole-derived carbon are beneficial for the electron transfer and electrical conductivity of carbons.[34] On the other side, pyrrolic-N and pyridinic-N often considered electrochemically active in aqueous solution, contributing pseudo-capacitance due to the additional p-electron donation to the aromatic π system.[35] The total proportion of pyrrolic-N and pyridinic-N in MC-7-SD (32.54 and 29.23 At%) are higher than those in MC-7-AD (28.97 and 22.51 At%) and MC-7-FD (33.76 and 19.19 At%), possibly due to more edges in the carbon framework. With more electrochemically active nitrogen, MC-7-SD is expected to show larger pseudo-capacitive contribution in capacitance.
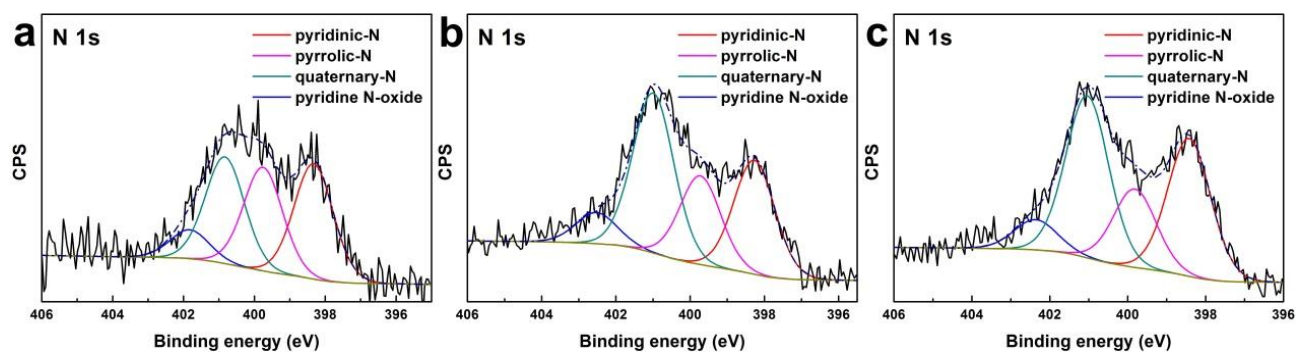
Figure 5.4 High-resolution N1s spectra of a) MC-7-SD, b) MC-7-AD and c) MC-7-FD.

Table. 5.2 The nitrogen-doping content of MC-7-SD, MC-7-AD, and MC-7-FD.

Sample	N wt%	N At%	Pyridinic-N At%	Pyrrolic-N At%	Quaternary-N At%	Pyridine N-oxide At%
MC-7-SD	9.46	8.67	32.54	29.23	30.09	8.14
MC-7-AD	9.75	7.05	28.97	22.51	40.61	7.91
MC-7-FD	9.33	8.50	33.76	19.19	39.65	7.40

The electrochemical performances of MC-7-SD, MC-7-AD, and MC-7-FD have been evaluated in Figure 5.5. Figure 5.5a shows the rectangular-shaped CV curves of MC-7-SD, MC-7-AD, and MC-7-FD. The broadened redox peaks in CV curves can be observed from -0.8 to -0.3 V. These wide and vague peaks are attributed to multiple faradaic peaks,[20] partially associated with the pseudo-capacitance of pyrrolic-N/pyridinic-N.[36] The representative galvanostatic charge-discharge curves of mesoporous carbons at a current density of 1 A/g are shown in Figure 5.5b. The charge-discharge curves are nearly linear and symmetric with a slight curvature, which suggests a good capacitive behaviour and electrochemical reversibility.[37] The dependence of specific capacitances on the current density in Figure 5c shows that MC-7-SD delivers the highest specific capacitance (533.6 F/g at 0.1 A/g, 362.8 F/g at 1 A/g) with a high surface area normalized capacitance (23.74 μF/cm^2 at 1 A/g). The specific capacitance and surface area normalized capacitance of MC-7-SD are higher than those of micropore-dominate activated carbon (161.5 F/g and 19.22 μF/cm^2 at 1 A/g, Figure 5.S8), revealing the high utilization efficiency of mesopore-dominate structure.
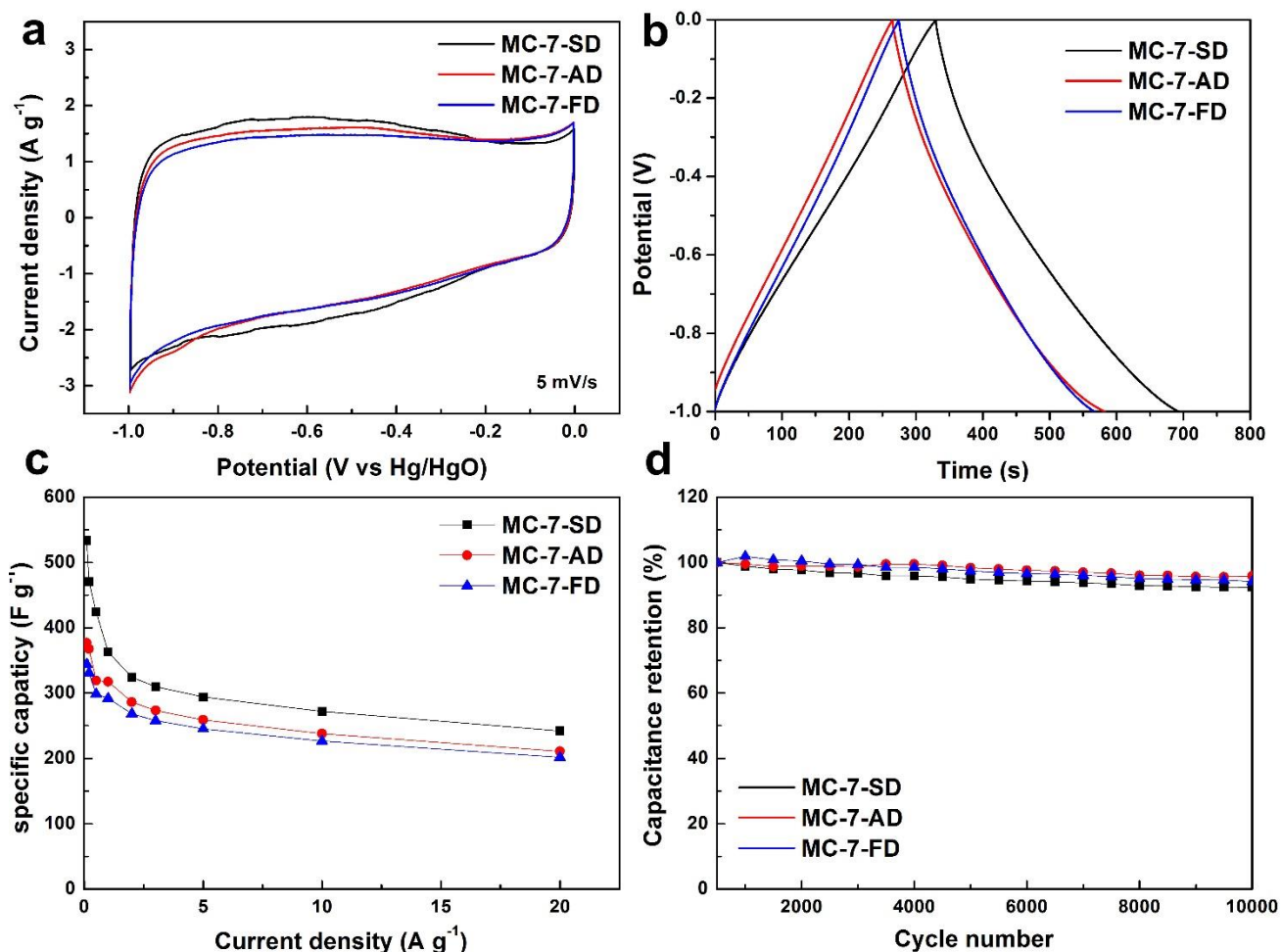
Figure 5.5 a) Cyclic voltammetry curves at 5mV/s, b) galvanostatic charge/discharge curves at 1 A/g, c) specific capacitance of MC-7-SD, MC-7-AD, and MC-7-FD and d) cycle performance of MC-7-SD, MC-7-AD, and MC-7-FD at 5 A/g.

With higher specific surface area and more electrochemically active nitrogen, the capacitance of MC-7-SD (362.8 F/g) is better than those of MC-7-AD and MC-7-FD (317.5 and 291.9 F/g at 1 A/g, respectively). It is noted the capacitance of MC-7-SD is comparable or better than those of mesoporous carbons reported in literature (Table. 5S3). Even at a high current density of 20 A/g, a capacitance of 242.2 F/g can be maintained in MC-7-SD, corresponding to 66.8% of capacity retention. Compared to other mesopore-dominate carbon materials,[7] The higher capacity retention of MC-7-SD indicates the advantage of large mesopore sizes favourable for rapid charge/discharge. A long-lasting cycle life with less than 8% capacitance loss after 10000 cycles is obtained in MC-7-SD under 5 A/g (Figure 5.5d), slightly weaker than those of MC-7-AD and MC-7-FD (5% and 6% capacitance loss, respectively). This observation is in accordance with a previous report: larger pores facilitate the ion transportation, resulting in better cycling stability under high current charge-discharge.[38] Apart from high gravimetric performance, MC-7-SD also achieves a superior

volumetric capacitive behaviour (208.1 F/cm^3 at 0.1 A/g) when calculating using an apparent density of 0.50 g/cm^3.

The superior electrochemical performance of MC-7-SD for EDLCs can be attributed to its unique structural features. Firstly, the thin carbon layer coated by vapour deposition results in a high mesoporous surface area, which leads to a high accessible electrode-electrolyte interface for electric double layer formation. Secondly, the high content of nitrogen doping provides additional electrochemically active nitrogen for pseudo-capacitance. Thirdly, relatively large mesopores in the carbon framework are beneficial for the remarkable capacitance retention at high current densities. Fourthly, the micro-spherical morphology of MC-7-SD is ideal for effective packing and excellent volumetric capacitive performance.

5.3 Conclusions

In summary, nitrogen-doped mesoporous carbon microspheres have been successfully synthesized by spray drying-vapour deposition method. The resulting carbon microspheres possess a mesopore-dominate (95%) high surface area of 1528 m^2/g, a nitrogen-doping of 8 At %, and an apparent density of 0.5 g/cm^3. Benefiting from its unique features, MC-7-SD manifests excellent gravimetric/volumetric performance (533.6 F/g and 208.1 F/cm^3). Our work opens up opportunities for the fabrication of efficient-packed porous carbon materials with heteroatom-doping for wide applications.

5.4 Experimental section

5.4.1 Material Synthesis

Highly Nitrogen-doped mesoporous carbon microspheres were synthesized via spray drying and vapor deposition method. Typically, Ludox SM colloidal silica (40 g, 30 wt. % suspension in H$_2$O, Sigma-Aldrich) was mixed with iron chloride (FeCl$_3$) solution (0.3 M, 25 ml) and deionized water (200 ml). The mixture was ultrasonicated for over 1 h and kept stirring while spray drying. The suspension was spray dried at an inlet temperature of 220 ℃, a pump rate of 1.5 ml/min, and N$_2$ gas flow of 60 ml/min. The spray dried sample was coated with pyrrole vapor for 48h in 50 ℃ oven before carbonized at 800 ℃ for 10 h in a nitrogen atmosphere. Then the composite was washed with 5 wt. % hydrofluoric acid (HF) to remove the sacrificial silica template. The resulting product was centrifuged and washed repeatedly with deionized water and dried in an oven (addressed as MC-7-SD). For comparison, all other procedures remained the same, but the suspension was dried using 50 ℃ oven or freeze-drier after sonication. The resultant was addressed as MC-7-AD or MC-

7-FD, respectively. Activated carbon Darco® G-60 (-100 mesh, Sigma-Aldrich) was also used for comparison.

5.4.2 Characterization

Field emission scanning electron microscopy (SEM) images were obtained using JEOL 7001. Transmission electron microscopy (TEM) images were taken using JEOL 1010 at 100 kV. High resolution transmission electron microscopy (HRTEM) was conducted under a Tecnai G2 F20 (FEI) operated at 200 kV. Nitrogen sorption isotherms were measured by Tristar II Surface Area and Porosity analyser (Micromeritics). The sample was degassed at 180 ℃ overnight under vacuum before the test. X-ray photoelectron spectroscopy (XPS) was recorded on a monochromatic Al Kα (1486.6 eV) X-ray source and 165 mm hemispherical electron energy analyzer. The elemental analysis was carried out using a Thermo Flash EA-1112 Series NCHS-O analyzer. Dynamic light scattering (DLS) measurement was conducted on a Malvern Zetasizer Nano ZS instrument at room temperature. Thermogravimetric (TG) analysis was performed using METTLER TOLEDO TGA/DSC1 STAR^e System from 25 ℃ to 900 ℃ in air with a heating rate of 5 ℃ min^{-1}.

5.4.3 Electrochemical measurements

A slurry composing of active material (80 wt. %), carbon black (10 wt. %), and polytetrafluoroethylene (PTFE, Sigma-Aldrich, 60 wt. % dispersion in H_2O) (10 wt. %) was mixed with ethanol. The working electrode was prepared by encapsulating mixture into Ni foam and dried at 100 ℃ overnight. A three-electrode system was used to measure the electrochemical performance in 6 M KOH solution. Ni foam and Hg/HgO electrode were served as counter and reference electrode, respectively. Electrochemical measurements were carried out over a 1 V potential window (-1~0 V vs. Hg/HgO) using Solartron Multistat 1480.

5.5 Supplementary information
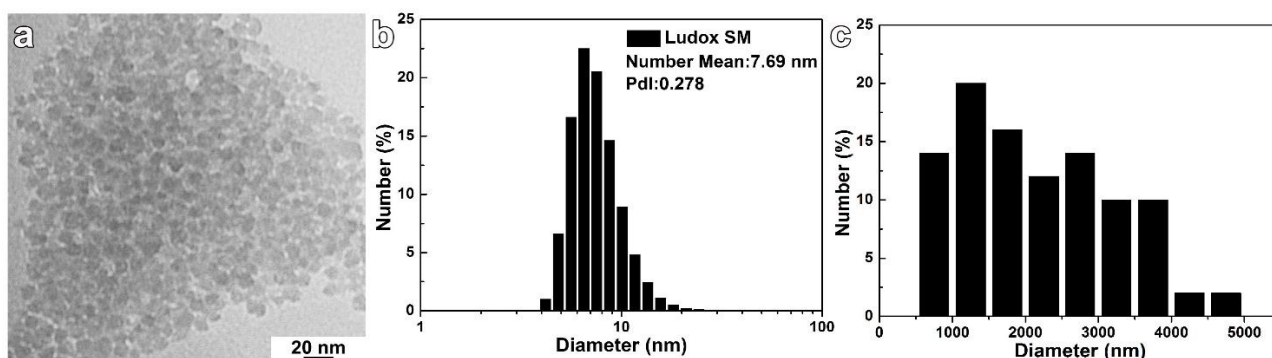
Figure 5.S1 a) TEM image and b) DLS analysis of sacrificial silica template, c) Size distribution of N-doped mesoporous carbon microspheres.
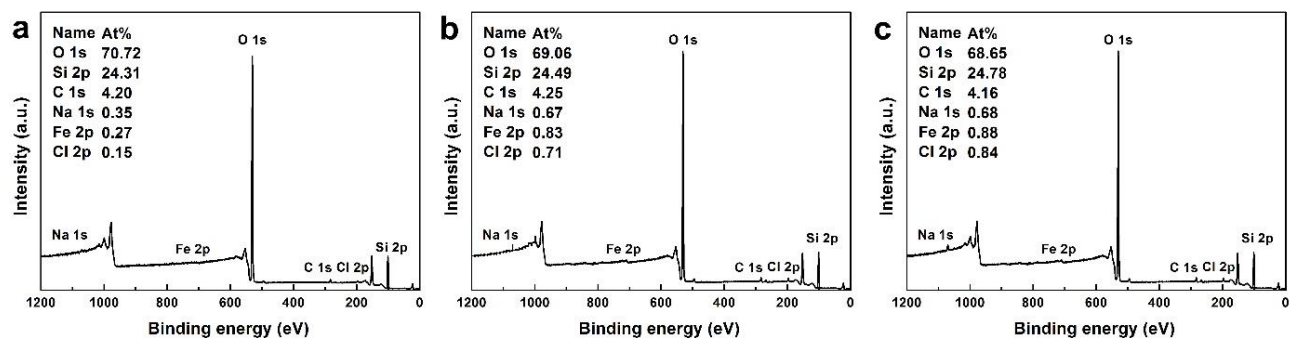
Figure 5.S2 XPS survey spectra of a) MC-7-SD template, b) MC-7-AD template, and c) MC-7-FD template. The C comes from contamination and Na comes from the stabilizer in the pristine silica suspension.
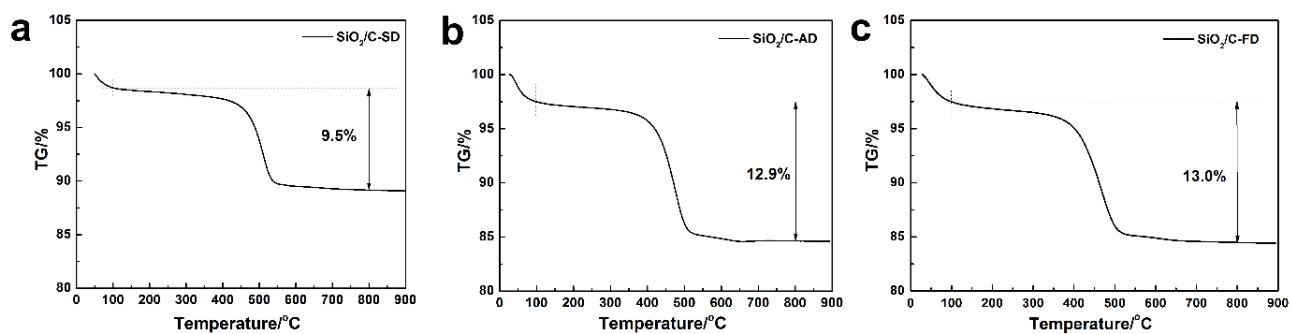
Figure 5.S3 TGA spectra of silica/carbon composite synthesized using a) spray drying, b) air drying, and c) freeze drying method.
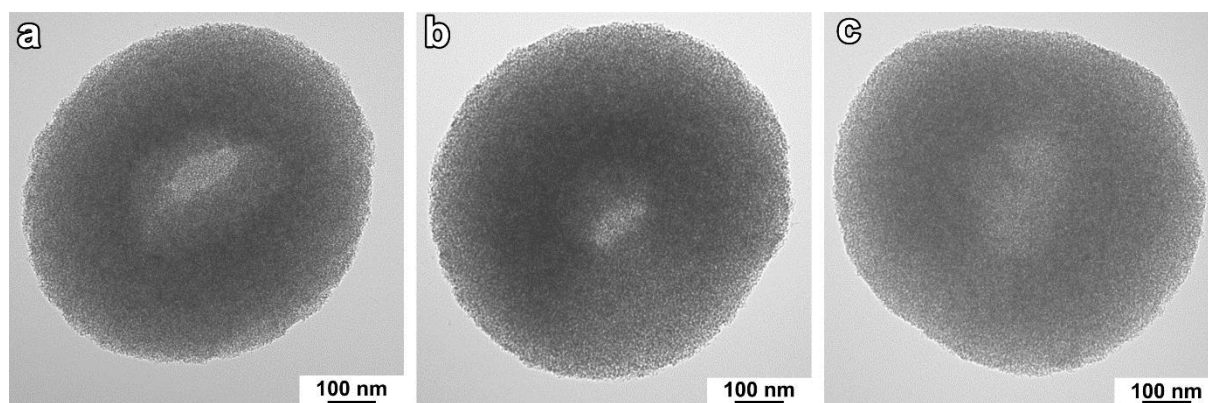
Figure 5.S4 TEM images of MC-7-SD carbonized at a) 650 ℃, b) 800 ℃, and c) 950 ℃.
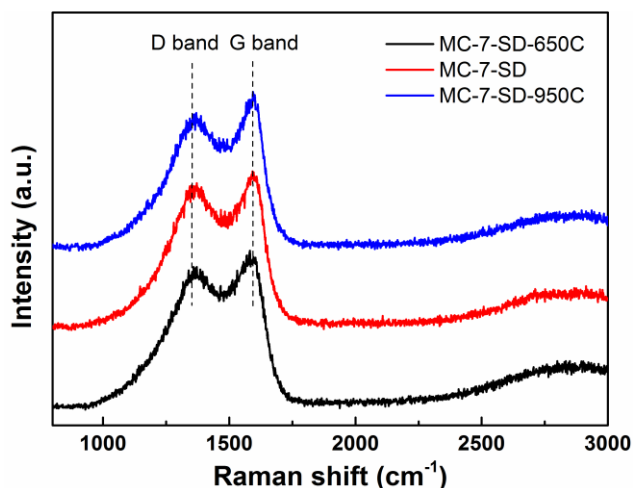
Figure 5.S5 Raman spectra of MC-7-SD carbonized in different temperature.
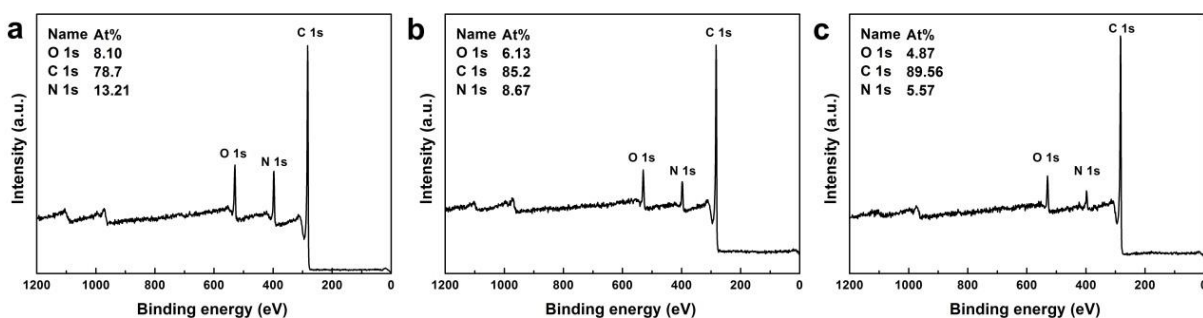
Figure 5.S6 XPS survey spectra of MC-7-SD carbonized at a) 650 ℃, b) 800 ℃, and c) 950 ℃.
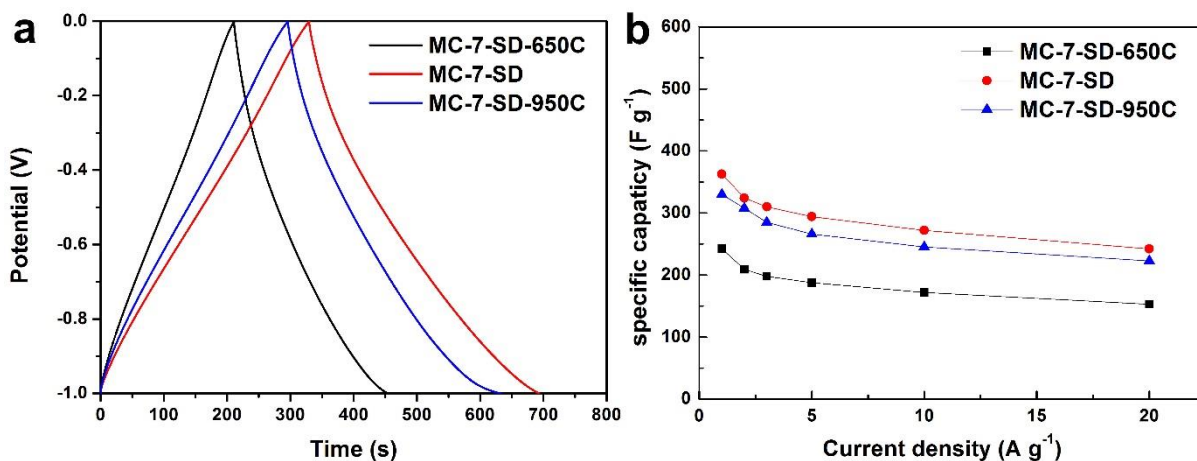
Figure 5.S7 a) Galvanostatic charge/discharge curves at 1 A/g, b) specific capacitances of MC-7-SD carbonized in different temperature.
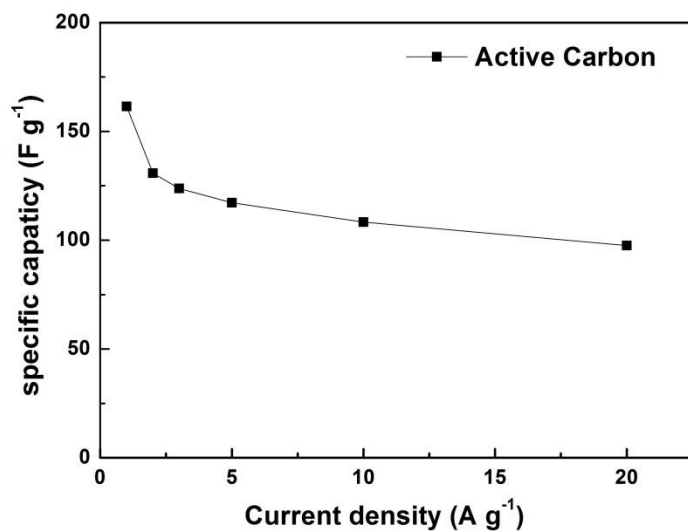
Figure 5.S8 Specific capacitance of activated carbon.

Table. 5.S1 Textural properties of MC-7-SD carbonized in different temperature.

Sample	S_{BET} (m^2/g)	V_t (cm^3/g)
MC-7-SD-650C	1437	1.4
MC-7-SD	1528	1.6
MC-7-SD-950C	1710	1.8

Note: S_{BET} is BET surface area calculated from P/P$_0$=0.05-0.3, V_t is total pore volume at P/P$_0$=0.995,

Table. 5.S2 Nitrogen-doping content of MC-7-SD carbonized in different temperature.

sample	MC-7-SD-650C	MC-7-SD	MC-7-SD-950C
Elemental analysis (wt%)	13.29	9.46	6.47

Table. 5.S3 Electrochemical performance comparison among mesoporous carbon materials.

Materials	Electrolytes	Specific capacitance	Reference
N-doped graphene nanosheets	6 M KOH	302 F/g at 5 mV/s	1
N-doped porous carbon nanofibers	6 M KOH	202 F/g at 1 A/g	2
N-doped ordered mesoporous carbon	6 M KOH	227 F/g at 0.2 A/g	3
3D hierarchical porous carbon	6 M KOH	236.3 F/g at 2 A/g	4
N-enriched nanoporous carbon	6 M KOH	261 F/g at 0.02 A/g	5
Heteroatom doped porous carbon flakes	6 M KOH	340 F/g at 1 A/g	6
Functionalized graphene nanosheets	6 M KOH	456 F/g at 0.5 A/g	7
N-doped carbon nanocages	6 M KOH	313 F/g at 1 A/g	8
Hollow carbon nanospheres	6 M KOH	203 F/g at 0.1 A/g	9
Bamboo-loke carbon nanofiber	3 M KOH	236 F/g at 5 A/g	10
N-doped mesoporous carbon	6M KOH	405 F/g at 1 A/g	11
Mesoporous carbon hollow spheres	6 M KOH	310 F/g at 1A/g	12
B/N co-doped carbon nanosheets	6 M KOH	223 F/g at 0.1 A/g	13
Graphene nanoribbons	1 M H_2SO_4	193 F/g at 10 mV/s	14
N-doped mesoporous carbon microspheres	6 M KOH	533.6 F/g at 0.1 A/g 362.8 F/g at 1 A/g	This work

[1] Wen, Z.; Wang, X.; Mao, S.; Bo, Z.; Kim, H.; Cui, S.; Lu, G.; Feng, X.; Chen, J., *Adv. Mater.* **2012**, *24*, 5610.

[2] Chen, L.-F.; Zhang, X.-D.; Liang, H.-W.; Kong, M.; Guan, Q.-F.; Chen, P.; Wu, Z.-Y.; Yu, S.-H., *ACS Nano* **2012**, *6*, 7092.

[3] Wei, J.; Zhou, D.; Sun, Z.; Deng, Y.; Xia, Y.; Zhao, D., *Adv. Funct. Mater.* **2013**, *23*, 2322.

[4] Qie, L.; Chen, W.; Xu, H.; Xiong, X.; Jiang, Y.; Zou, F.; Hu, X.; Xin, Y.; Zhang, Z.; Huang, Y., *Energy Environ. Sci.* **2013**, *6*, 2497.

[5] Wu, D.; Li, Z.; Zhong, M.; Kowalewski, T.; Matyjaszewski, K., *Angew. Chem. Int. Ed.* **2014**, *53*, 3957.

[6] Qian, W.; Sun, F.; Xu, Y.; Qiu, L.; Liu, C.; Wang, S.; Yan, F., *Energy Environ. Sci.* **2014**, *7*, 379.

[7] Yan, J.; Wang, Q.; Wei, T.; Jiang, L.; Zhang, M.; Jing, X.; Fan, Z., *Acs Nano* **2014**, *8*, 4720.

[8] Zhao, J.; Lai, H.; Lyu, Z.; Jiang, Y.; Xie, K.; Wang, X.; Wu, Q.; Yang, L.; Jin, Z.; Ma, Y.; Liu, J.; Hu, Z., *Adv. Mater.* **2015**, *27*, 3541.

[9] Xu, F.; Tang, Z.; Huang, S.; Chen, L.; Liang, Y.; Mai, W.; Zhong, H.; Fu, R.; Wu, D., *Nat Commun* **2015**, *6*, 7221.

[10] Sun, Y.; Sills, R. B.; Hu, X.; Seh, Z. W.; Xiao, X.; Xu, H.; Luo, W.; Jin, H.; Xin, Y.; Li, T.; Zhang, Z.; Zhou, J.; Cai, W.; Huang, Y.; Cui, Y., *Nano Lett.* **2015**, *15*, 3899.

[11] Lin, T. Q.; Chen, I.-W.; Liu, F. X.; Yang, C. Y.; Bi, H.; Xu, F. F.; Huang, F. Q., *Science*, **2015**, *350*, 1508.

[12] Zhang, H.; Noonan, O.; Huang, X.; Yang, Y.; Xu, C.; Zhou, L.; Yu, C., *Acs Nano* **2016**, *10*, 4579.

[13] Ling, Z.; Wang, Z.; Zhang, M.; Yu, C.; Wang, G.; Dong, Y.; Liu, S.; Wang, Y.; Qiu, J., *Adv. Funct. Mater.* **2016**, *26*, 111.

[14] Pachfule, P.; Shinde, D.; Majumder, M.; Xu, Q., *Nat Chem* **2016**, *8*, 718.

5.6 References

[1]   a) Simon, P.; Gogotsi, Y., *Nat. Mater.* **2008**, *7*, 845; b) Frackowiak, E.; Béguin, F., *Carbon* **2001,** *39*, 937.; c) Wang, G.; Zhang, L.; Zhang, J., *Chem. Soc. Rev.* **2012,** *41*, 797; d) Liu, C.; Li, F.; Ma, L.-P.; Cheng, H.-M., *Adv. Mater.* **2010,** *22*, E28; e) Choi, N.-S.; Chen, Z.; Freunberger, S. A.; Ji, X.; Sun, Y.-K.; Amine, K.; Yushin, G.; Nazar, L. F.; Cho, J.; Bruce, P. G., *Angew. Chem. Int. Ed.* **2012,** *51*, 9994.

[2]   Zhai, Y.; Dou, Y.; Zhao, D.; Fulvio, P. F.; Mayes, R. T.; Dai, S., *Adv. Mater.* **2011**, *23*, 4828.

[3]   Zhang, Y.; Feng, H.; Wu, X.; Wang, L.; Zhang, A.; Xia, T.; Dong, H.; Li, X.; Zhang, L., *Int. J. Hydrogen Energy* **2009,** *34*, 4889.

[4]   a) Barbieri, O.; Hahn, M.; Herzog, A.; Kötz, R., *Carbon* **2005,** *43*, 1303; b) Weingarth, D.; Zeiger, M.; Jäckel, N.; Aslan, M.; Feng, G.; Presser, V., *Adv. Energy Mater.* **2014,** *4*, 1400316.

[5]   Zhang, L. L.; Zhao, X. S., *Chem. Soc. Rev.* **2009,** *38*, 2520.

[6]   Huang, J.; Sumpter, B. G.; Meunier, V., *Chem. Eur. J.* **2008,** *14*, 6614.

[7]   Qian, W.; Sun, F.; Xu, Y.; Qiu, L.; Liu, C.; Wang, S.; Yan, F., *Energy Environ. Sci.* **2014,** *7*, 379.

[8]   Li, Z.; Xu, Z.; Tan, X.; Wang, H.; Holt, C. M. B.; Stephenson, T.; Olsen, B. C.; Mitlin, D., *Energy Environ. Sci.* **2013,** *6*, 871.

[9]   Li, W.; Liu, J.; Zhao, D. Y., *Nat. Rev. Mater.* **2016**, *1*, 16023.

[10]   a) Shen, G.; Sun, X.; Zhang, H.; Liu, Y.; Zhang, J.; Meka, A.; Zhou, L.; Yu, C., *J. Mater. Chem. A* **2015**, *3*, 24041; b) Wei, J.; Zhou, D.; Sun, Z.; Deng, Y.; Xia, Y.; Zhao, D., *Adv. Funct. Mater.* **2013**, *23*, 2322.

[11]   Ryoo, R.; Joo, S. H; Jun, S., *J. Phys. Chem. B.* **1999**, *103*, 7743.

[12]   Han, S.; Sohn, K.; Hyeon, T., *Chem. Mater.* **2000**, *12*, 3337.

[13]   Han, S.; Hyeon, T., *Chem. Comm.* **1999**, 1955.

[14]   a) Gogotsi, Y.; Simon, P., *Science* **2011**, *334*, 917; b) Wang, Q.; Yan, J.; Fan, Z., *Energy Environ. Sci.* **2016**, *9*, 729.

[15]   Li, W.; Liang, Z.; Lu, Z.; Yao, H.; Seh, Z. W.; Yan, K.; Zheng, G.; Cui, Y., *Adv. Energy Mater.* **2015**, *5*, 1500211.

[16]   Zhou, L.; Xu, H.; Zhang, H.; Yang, J.; Hartono, S. B.; Qian, K.; Zou J.; Yu, C., *Chem. Comm.* **2013**, *49*, 8695.

[17]   Tan, A.; Martin, A.; Nguyen, T.-H.; Boyd, B. J.; Prestidge, C. A., *Angew. Chem. Int. Ed.* **2012**, *51*, 5475.

[18]   Li, X.; Zhou, J.; wang, J.; Qiao, W.; Ling L.; Long, D.; *RSC Adv.* **2014**, *4*, 62662.

[19]   a) Wang, X.; Fan, X.; Li, G.; Li, M.; Xiao, X.; Yu A.; Chen, Z., *Carbon* **2015**, *93*, 258; b) Wang, D.; Fu, A.; Li, H.; Wang, Y.; Guo, P.; Liu J.; Zhao, X. S., *J. Power Sources* **2015**, *285*, 469.

[20]   Lin, T.; Chen, I.-W.; Liu, F.; Yang, C.; Bi, H.; Xu, F.; Huang, F., *Science* **2015**, *350*, 1508.

[21]   Han, F.; Li, D.; Li, W.-C.; Lei, C.; Sun Q.; Lu, A.-H., *Adv. Funct. Mater.* **2013**, *23*, 1692.

[22]   a) Shen, W.; Fan, W., *J. Mater. Chem. A* **2013,** *1*, 999; b) Wang, X.; Sun, G.; Routh, P.; Kim, D.-H.; Huang, W.; Chen, P., *Chem. Soc. Rev.* **2014,** *43*, 7067.

[23]   Ferrero, G. A.; Fuertes A. B.; Sevilla, M., *J. Mater. Chem. A* **2015**, *3*, 2914.

[24]   Gierszal, K. P.; Jaronic, M., *J. Phys. Chem. C* **2007**, *111*, 9742.

[25]   Zhang, H.; Hussain, I.; Brust, M.; Butler, M. F.; Rannard S. P.; Cooper, A. I., *Nat. Mater.* **2005**, *4*, 787.

[26]   a) Pei, F.; An, T. H.; Zang, J.; Zhao, X. J.; Fang, X. L.; Zheng, M. S.; Dong, Q. F; Zheng, N. F.; *Adv. Energy Mater.* **2016**, *6*, 1502539; b) Liu, Y; Zhang, H; Noonan, O; Xu, C; Niu, Y; Yang, Y; Zhou, L; Huang, X; Yu, C, *Chem. Eur. J.* **2016**, *22*, 14962.

[27]   Biswas, P.; Sen, D.; Mazumder, S.; Basak, C. B.; Doshi, P., *Langmuir* **2016**, 32, 2464.

[28]   Sen, D.; Bahadur, J.; Mazumder, S.; Bhattacharya, S., *Soft Matter* **2012**, *8*, 10036.

[29]   Ying, J.; Jiang, C.; Wan, C., *J. Power Sources* **2004,** *129*, 264.

[30]   Wilkowska, A.; Ambroziak, W.; Czyżowska, A.; Adamiec, J., *Pol. J. Food Nutr. Sci.* **2016**, *66*, 11.

[31]   Yang, C.-M.; Weidenthaler, C.; Spliethoff, B.; Mayanna M.; Schüth, F., *Chem. Mater.* **2005**, *17*, 355.

[32]   Zhang, H.; Yu, M.; Song, H.; Noonan, O.; Zhang, J.; Yang, Y.; Zhou L.; Yu, C., *Chem. Mater.* **2015**, *27*, 6297.

[33]   a) Tuinstra, F.; Koenig, J. L., *J. Chem. Phys.* **1970**, *53*, 1126; b)   Wang, Y.; Alsmeyer, D. C.; McCreery, R. L., *Chem. Mater.* **1990**, *2*, 557; c) He, C.; Wu, S.; Zhao, N.; Shi, C.; Liu E.; Li, J., *Acs Nano* **2013**, *7*, 4459.

[34]   Hou, J.; Cao, C.; Idrees, F.; Ma, X., *Acs Nano* **2015**, *9*, 2556.

[35]   a) Sun, L.; Tian, C.; Fu, Y.; Yang, Y.; Yin, J.; Wang, L.; Fu, H., *Chem. Eur. J.* **2014**, *20*, 564; b) Lai, L.; Potts, J. R.; Zhan, D.; Wang, L.; Poh, C. K.; Tang, C.; Gong, H.; Shen, Z.; Lin, J.; Ruoff, R. S., *Energy Environ. Sci.* **2012**, *5*, 7936.

[36]   Xu, B.; Hou, S.; Cao, G.; Wu, F.; Yang, Y., *J. Mater. Chem.* **2012**, *22*, 19088.

[37]   Zhang, H.; Noonan, O.; Huang, X.; Yang, Y.; Xu, C.; Zhou, L.; Yu, C., *Acs Nano* **2016**, *10*, 4579.

[38]   Ma, X.; Gan, L.; Liu, M.; Tripathi, P. K.; Zhao, Y.; Xu, Z.; Zhu, D.; Chen, L., *J. Mater. Chem. A* **2014**, *2*, 8407.

Chapter 6

Synthesis of nitrogen-doped Three-dimensionally Ordered Macroporous Carbon Microspheres

This chapter reports the development of Nitrogen-doped three-dimensionally ordered macroporous carbon microspheres via a spray drying-vapour deposition method. A hexagonal-close-packed periodicity of macropores is achieved through the spray drying method. Vapour deposition of polypyrrole followed by carbonization and etching is beneficial for the generation of carbon network with a wall thickness of 3.5 nm. The resultant 3DOM carbon microspheres possess a hexagonal close packing structure with a high surface area of 892 m^2/g, an ultrahigh pore volume of 7.5 cm^3/g and high nitrogen doping of 8 At%. Applied as the cathode material for Al-ion batteries, this material shows promising electrochemical performances, demonstrating its great potential for electrical energy storage applications.

6.1 Introduction

Ordered porous carbon materials have received tremendous attentions due to their superior physical and chemical properties, such as large surface area, uniform and adjustable pore size, high conductivity, and mechanical/chemical stability.[1-3] Among them, three-dimensionally ordered macroporous (3DOM) carbon materials hold a distinctive position,[4] because the well-ordered macropores can provide high pore volume with excellent accessibility for improved mass transportation,[5, 6] guest substances accommodation[7] or volume change buffering.[6]

Colloidal crystal templating is the most widely used method for the synthesis of 3DOM carbon materials.[2, 4] The colloidal crystal structures constructed by the ordered assembly of uniform-sized siliceous or polymer nanoparticles serve as sacrificial templates and direct the porous structure and the morphology of the carbon products. Despite their demonstrated success on pore structure control, conventional templates prepared through sedimentation, centrifugation, physical confinement, and vertical deposition process[2] have limited capability on tuning the material morphologies and only lead to powder or bulk monolithic 3DOM carbon products.

Micron-sized spherical morphologies are generally required for the electrode material design in rechargeable battery applications, due to the reduced solid-electrolyte interfaces to minimize side reactions and the potential high tapped density for electrode preparation.[8, 9] Recently, Cui and co-workers reported a emulsion assisted strategy for the assembly of colloidal siliceous nanospheres into micron-sized spherical hard template and consequently produced macroporous carbon microsphere materials with enhanced properties for lithium-sulfur battery applications.[8] However, this method requires complicated procedures for the formation of stable emulation system and the subsequent microsphere templates. Spray drying/pyrolysis approaches are also reported for development of micro-spherical materials with 3DOM architechtures.[10] Ko et al. claimed the preparation 3DOM-structured SnO_2-carbon microspheres through one-pot spray pyrolysis synthesis.[9] Droplets containing polystyrene nanobeads, tin oxalate and dextrin were dried first, and then macroporous SnO_2-carbon composite microspheres were obtained after thermal decomposition of polystyrene templates. However, very limited characterisations on the ordered periodicity of the claimed 3DOM structure is demonstrated. More importantly, the feasibility of spray drying strategy for the preparation of micro-spherical templates for pristine carbonaceous 3DOM microspheres synthesis has not been demonstrated.

The carbon precursors and their impregnation approaches are essential for the fabrication of 3DOM carbon materials with desired structures and surface chemistry for targeted applications.[4] Among various approaches, the chemical vapour deposition (CVD) method has attracted great interests, due to the advantage of forming uniform thin carbon coatings onto hard templates with diverse architechtures.[11-15] CVD method has been widely applied for the synthesis of carbon nanostructures from nanoporous materials to various carbon-based nanocomposites.[16] However, conventional CVD procedures using flammable gaseous carbon precursors at high temperature pose safety risks and limit the scalable production of desired materials for their massive applications.[15] Exploring novel carbon precursors with the ability to enable low temperature vapour deposition is critical for the further development of CVD technology with improved production capability and operational safety.[17] Because of its high vapour pressure (8.35 mmHg) at room temperature and the ease of polymerization, pyrrole holds great promises as the carbon precursors for the synthesis of carbonaceous nanomaterial through the low-temperature vapour deposition strategy. However, to date, applying such strategy on the synthesis of 3DOM carbon materials has not been reported.

Herein, we report the synthesis of nitrogen (N)-doped 3DOM carbon microsphere by a combined spray drying-low temperature vapour deposition approach. Benefiting from the micron-sized spherical silica templates assembled by spray drying, N-3DOM carbon microsphere presents well-ordered macroporous structure with a high surface area of 892 m^2 g^{-1} and an ultra-large pore volume of 7.5 cm^3 g^{-1} (the highest among all previously reported macroporous carbon materials). As a demonstration of the application potential, N-3DOM carbon microsphere was applied as the cathode material for rechargeable aluminum (Al)-ion batteries and demonstrated promising electrochemical performances (high reversible capacity of 117.3 mA h g^{-1} at 1 A g^{-1} and good capacity retention over 100 cycles).

6.2 Results and discussion

N-3DOM carbon microsphere was synthesized by spray drying silica nanoparticle/water suspension containing FeCl$_3$ catalyst, then coating polypyrrole through low-temperature vapour deposition. After carbonization at inert atmosphere and template removal, final carbon product can be produced. The morphology of N-3DOM carbon microsphere was investigated using scanning electron microscopy (SEM) and transmission electron microscopy (TEM). As shown in low-magnification SEM image (Figure 6.1a), N-3DOM carbon microsphere presents a spherical morphology with average particle size of 1-2 μm. The microspheres are constituted of tremendous macropores (Figure 6.1b), and the hexagonal

arrangement is found from the surface of the microsphere (shown in inset), which suggests that the microsphere obtained via spray drying-vapour deposition method possibly has hexagonal close-packed structure. TEM characterization (Figure 6.1c) also confirms the highly porous structure of carbon microsphere. Figure 1d shows the high-magnification image of the edge of this material. After measurement, the diameter of the macropore is 74.9 nm and the thickness of carbon wall is 3.5 nm. A window between the adjacent macropores is found with the size of 38 nm, resulting in 65.7 nm for the distance of centers between adjacent macropores.
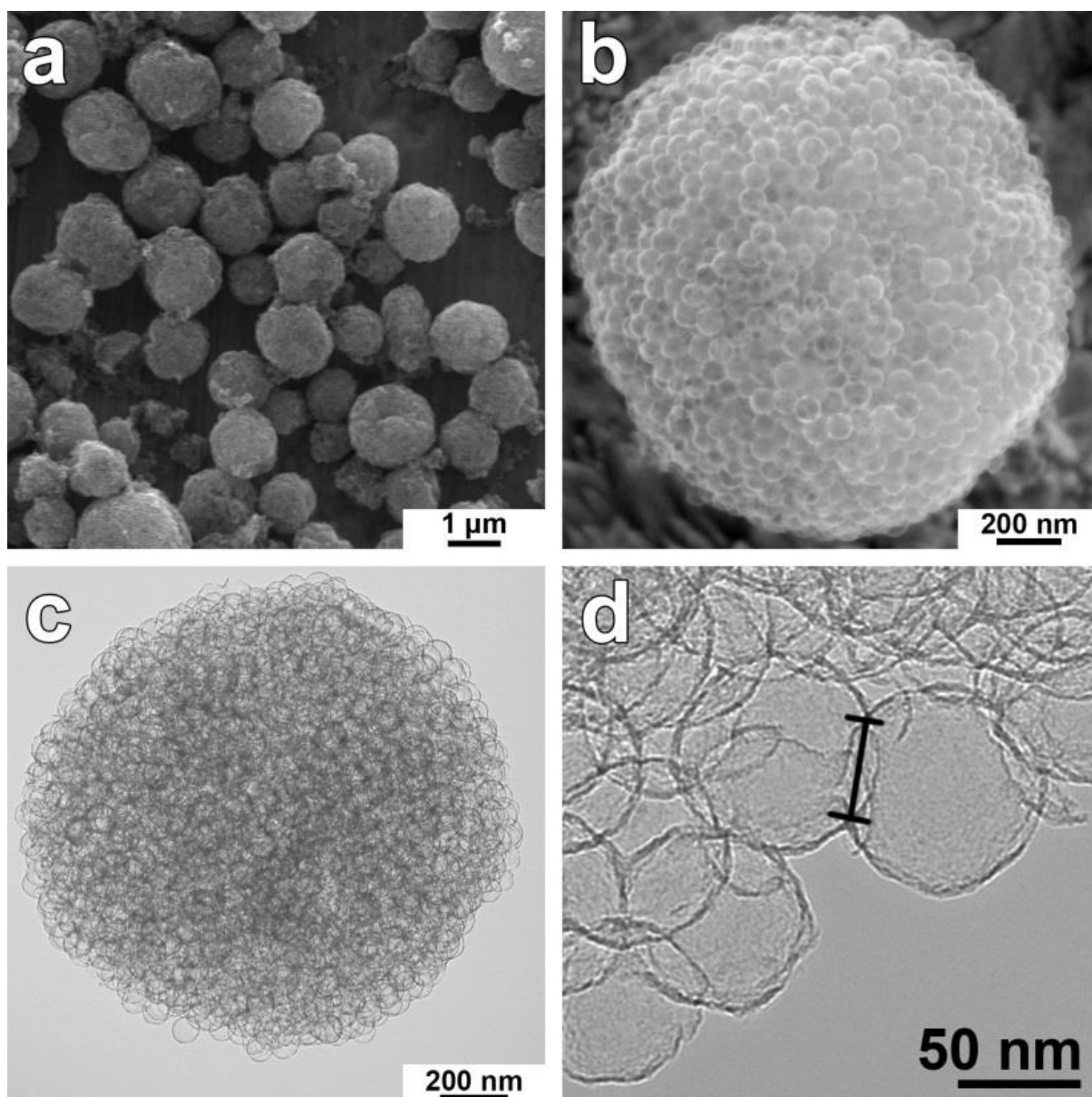

Figure 6.1 a-b) SEM and c-d) TEM images of N-3DOM carbon microsphere.

Nitrogen sorption analysis was employed to acquire more information about the pore structure of N-3DOM carbon microsphere. As shown in Figure 6.2, the carbon microsphere

shows typical IV isotherms with distinguished hysteresis loops. The adsorption branch of
isotherms exhibits major capillary condensation step in high relative pressure (P/P_0) range
of >0.8, indicating the existence of macropores. Calculated from the isotherms, this material
has a high Brunauer-Emmett-Teller (BET) surface area of 892 m^2/g. Moreover, N-3DOM
carbon microsphere has an ultra-large total pore volume 7.5 cm^3/g. which is the highest
among all macroporous carbon materials reported in literature.[18] The pore size distributions
(PSD) calculated by Broekoff–de Boer (BdB) model from adsorption/desorption branches are
shown in the inset. The adsorption branch gives two PSD peaks centred at 35.4 and 75.1 nm,
respectively. The peak centred at 75.1 nm is in high accordance with the size of macropores
measured from TEM, and also very close to the diameter of stöber silica nanoparticle
template (Figure 6.S1). The peak at 35.4 nm can be attributed by the octahedral voids in the
hexagonal close-packing structure. Apart from adsorption branch, a peak at 36.3 nm in
desorption branch is found. This size measured from nitrogen sorption is good consistent with
the observation from TEM, confirming the size of the window between adjacent macropores.
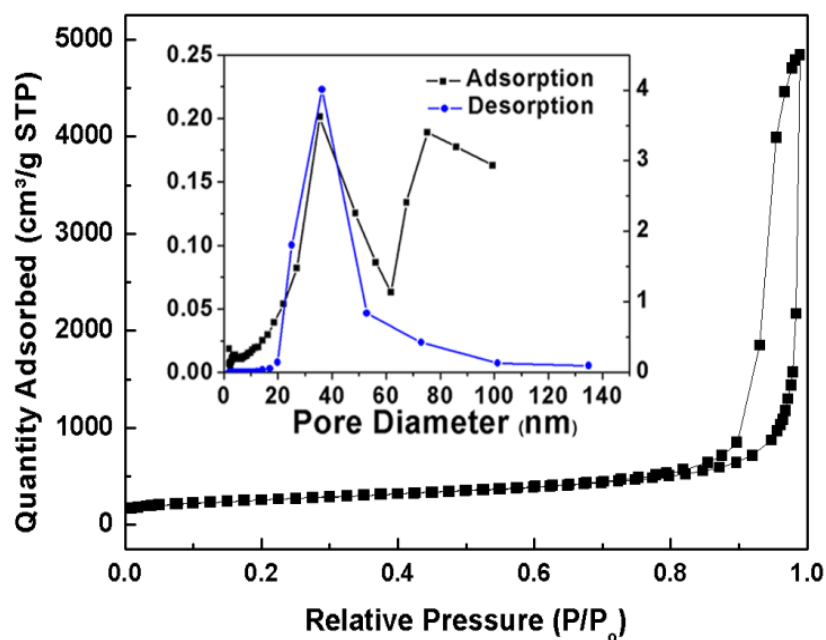
Figure 6.2 Nitrogen adsorption/desorption isotherm and pore size distribution (inset) of N-
3DOM carbon microsphere.

The macroporous structure of N-3DOM carbon microsphere was further investigated by
small angle X-ray scattering (SAXS). The SAXS pattern is shown in Figure 6.3. Four well-
resolved scattering peaks can be observed at q values of 0.09, 0.17, 0.24, and 0.31 nm^{-1},
which can be indexed to the 100, 110, 210 and 310 reflections, respectively. This observation
shows a clear hexagonal symmetry with orders of reflections: q^*, $\sqrt{3}q^*$, $\sqrt{7}q^*$, $\sqrt{11}q^*$, where

$q^*=2\pi/d_{\text{hcp}}$ with d_{hcp}=66.7 nm. The d_{hcp} calculated from SAXS pattern agrees well with the distance of adjacent macropore centres measured from TEM image (65.7 nm). The lattice constants of N-3DOM carbon microsphere is calculated to be a=66.7 nm and c=109 nm.
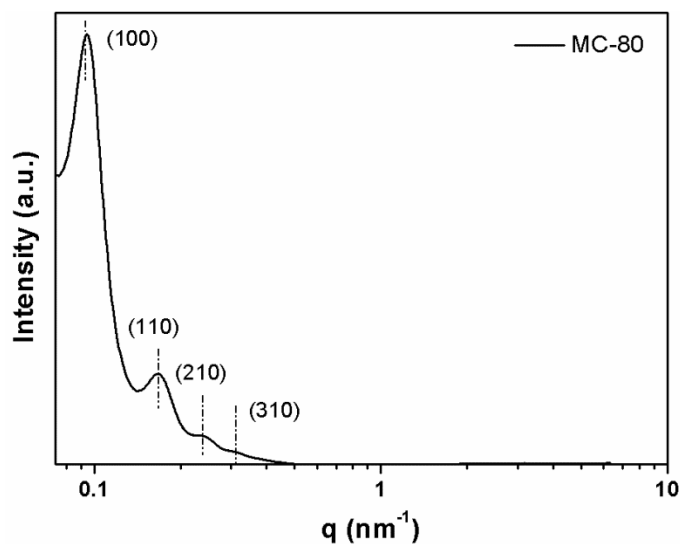

Figure 6.3 SAXS spectrum of N-3DOM carbon microsphere.

Electron tomography (ET) technique was used to study the detailed structures of N-3DOM carbon microsphere. A series of titled images were taken in the range of +65° to −65° with an increment of 1°. The ET slice, which cuts at the centre of the hollow spheres, exhibits a hexagonal close-packed morphology (Figure 6.4a). The carbon walls of the hollow spheres appear relatively continuous with average thicknesses of 3.5 nm. The pore diameter of the hollow spheres, the window between adjacent macropores, and the distance of adjacent pore centres are 75.7, 35.6, and 66.8 nm, respectively. The parameters measured from ET slices are in good accordance with the results measured from TEM images. Figure 6.4b is the 78 slices above Figure 6.4a along the z-axis, shows the ET slice of three triangle close-packed hollow spheres, cutting at the centre of the upper layer of hollow spheres. As the distance of each slice is 0.74 nm, the calculated central distance between two layers of hollow spheres is 57 nm (shown in Figure 6.4d). As c value in lattice constant reflects the central distance of three layers of hollow spheres, the central distance calculated from ET is similar to the results calculated from SAXS, revealing the periodic hexagonal close-packed structure of N-3DOM carbon microsphere.
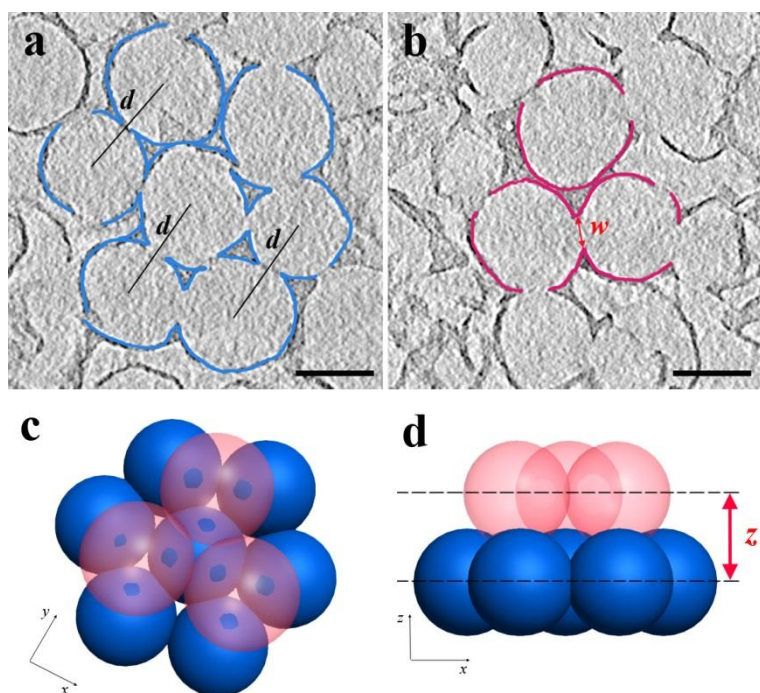
Figure 6.4 a) Electron tomography sliced at the center of 7 hexagonal close-packing spheres, b) the 78th ET slice above slice along z axis showing 3 close-packing spheres, c) top view of two layers of hexagonal close-packing model with 7 blue spheres packing as slice a and 3 red-transparent spheres packing as slice b, d) side view of the packing spheres with layer distance of z. Scale bar in a and b is 50 nm.

Besides hexagonal close-packed structure, the octahedral hollow voids can be observed from Figure 6.4a and 6.4b to show a typical "surface templating" morphology. The reason for surface templating is that iron chloride catalyst was added in the silica/water suspension and coated on the surface of the silica microspheres during spray drying. It is reported by incorporating the catalyst on the surface of aggregated template, the resulting carbon replica shows surface coating (surface templating) instead of complete filling of the entire void around the template (volume templating).[19] The observed octahedral hollow voids explain the ultrahigh pore volume of N-3DOM carbon microsphere: compared to volume templating synthesis, less mass of carbon was used in the surface templating synthesis of N-OMCMs, resulting in more hollow spaces and higher pore volume.

To investigate the formation of the 3DOM structure in N-3DOM carbon microsphere, the morphologies of as-obtained microspheres after spray drying, polypyrrole coating and carbonization were characterized by SEM (Figure 6.S2). A two-dimensional hexagonal pattern can be found on the surface of each microsphere, predicting the structural symmetry is formed during spray drying process and well maintained under the following procedure.

The microspheres with hexagonal close-packed structure assembled by spray drying colloidal silica nanoparticles is in accordance with literature reported.[20]

The nitrogen doping of N-3DOM carbon microsphere was confirmed by X-ray photoelectron spectroscopy (XPS), as shown in Figure 6.S3. According to XPS results, 8 At% nitrogen is accommodated in N-3DOM carbon microsphere after carbonization. The high-resolution N1s spectra (Figure S3) include 32.16% of pyridinic-N (398.5 eV), 15.59% of pyrrolic-N (399.6 eV), 44.99% of quaternary-N (401.0 eV), and 7.26% of pyridine N-oxide (402.4 eV). The high content of nitrogen doping and high proportion of quaternary-N in polypyrrole-derived carbon is beneficial for the electron transfer and superior electrical conductivity of carbons.

To demonstrate the application potential, N-3DOM carbon microsphere with high macroporous structure and conductive N-doped carbon skeleton was applied as the cathode material for rechargeable Al-ion batteries. The electrochemical performance was summarized in Figure 6.5. Similar to zeolite-templated carbon reported in previous literature,[21] the charge and discharge curves of N-OMCMs show capacitive behaviour without discernible plateau, with an average voltage of 1.5 V. The N-3DOM carbon microsphere delivers an initial discharge capacity of 117.3 mA h g^{-1} at the current density of 1C, then gradually decreases to 98.6, 92.8 and 88.4 mA h g^{-1} at the 20th, 50th and 100th cycle, respectively (Figure 6.5a). The N-3DOM carbon microsphere also shows a stable cycling performance with over 75% of the initial capacity is retained after 100 cycles, as shown in Figure 6.5b.

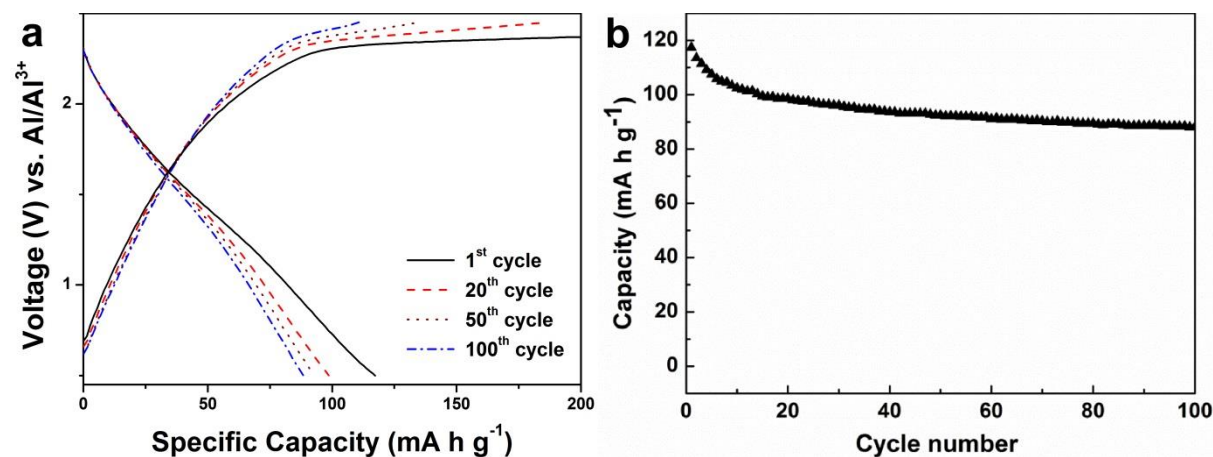
Figure 6.5 a) Representative charge-discharge profiles and b) Cycling performance of N-3DOM carbon microsphere.

The good electrochemical performance of N-3DOM carbon microsphere for Ai-ion batteries can be attributed to its unique structural features. First, the N-3DOM carbon microsphere shows high specific surface area, leads to a high electrode-electrolyte interface for AlCl$_4$$^-$ ion

insertion/desertion. Second, the macropores in N-3DOM carbon microsphere act as reservoir to provide good ion diffusion path. Third, the hexagonally closed-packed structure in N-3DOM carbon microsphere is beneficial for the charge storage capacity.[21] Fourth, the N-3DOM carbon microsphere contains a considerable amount of nitrogen to enhance the conductivity of the electrode material and the wettability to electrolyte.

6.3 Conclusion

Nitrogen-doped three-dimensionally ordered macroporous carbon microspheres were synthesized through a spray drying-vapour deposition method for the first time. A hexagonal-close-packed periodicity of macropores is achieved through the spray drying induced assembly of silica templates. Vapour deposition of polypyrrole followed by carbonization and silica-etching generate N-dopoed carbon network with a thin pore wall of 3.5 nm. The resultant 3DOM carbon microspheres possess a high surface area of 892 m^2/g, a record-large pore volume of 7.5 cm^3/g and a high nitrogen doping of 8 at%. Applied as the cathode material for Al-ion batteries, this material shows promising electrochemical performances, demonstrating its great potential for electrical energy storage applications.

6.4 Experimental section

6.4.1 Material Synthesis

The MC-80 porous carbon microspheres were synthesized using uniform nonporous silica nanoparticles developed by stöber as template.[22] Typically, ammonium hydroxide solution (1.5 ml, 28%, Sigma-Aldrich) was mixed with absolute ethanol (50 ml) and deionized water (3.8 ml) at 50 ℃. Then, tetraethyl orthosilicate (TEOS, 3 ml, 98%, Aldrich) was quickly added to the solution under vigorous stirring. After 3 h, the as-synthesized nanoparticles were washed with ethanol and water before dried in an oven.

As-obtained silica nanoparticles (1.6 g) were dispersed in deionized water (100 ml) under ultrasonication. Then Ferrite chloride solution (1.33 ml, 0.3 M, Sigma-Aldrich) was added under continuous stirring. The mixture was spray dried at an inlet temperature of 220 ℃, a pump rate of 1.5 ml/min, and N_2 gas flow of 60 ml/min. The spray-dried sample was sealed in pyrrole vapour for polypyrrole coating at 50 ℃ for 48 h, followed by carbonization in N_2 at 800 ℃ for 10 h. The resultant was obtained after using 5 wt. % hydrofluoric acid (HF) to remove the sacrificial nonporous silica template.

6.4.2 Characterization

Small-angle x-ray scattering (SAXS) was carried out at the SAXS beamline (BL16B1) of Shanghai Synchrotron Radiation Facility (SSRF). Field emission scanning electron microscopy (SEM) images were taken using JEOL 7100. Transmission electron microscope (TEM) images were obtained using JEOL 1010 microscope operated at 100 kV. Electron tomography (ET) was conducted under a Tecnai G2 F30 (FEI) operated at 300 kV. The specimens were prepared by dispersing the samples in ethanol under ultrasonication for 5 min, then directly deposited onto a formvar film supported copper grid (2000×1000 slot, Proscitech). Colloidal gold particles (10 nm) were deposited on both surfaces of the grid as fiducial markers for the subsequent image alignment procedures. Single tilting series was recorded in the range of +65 ° to −65 ° with an increment of 1 °. Nitrogen sorption isotherm was measured at 77 K using a Tristar II Surface Area and Porosity analyzer (Micromeritics). Before analysis, the samples were degassed at 180 ℃ overnight under vacuum. X-ray diffraction (XRD) patterns were carried out using Rigaku Miniflex X-ray Diffractometer with Co Kα radiation (λ= 0.179 nm). X-ray photoelectron spectroscopy (XPS) was recorded on a monochromatic Al Kα (1486.6 eV) X-ray source and 165 mm hemispherical electron energy analyzer. Fourier transform infrared (FTIR) spectra were performed with Thermo Nicolet Nexus 6700 FTIR spectrometer equipped with diamond crystal. Dynamic light scattering (DLS) measurement was conducted on a Malvern Zetasizer Nano ZS instrument at room temperature. The sample was dispersed in ethanol under ultrasonication, and then measured for at least 3 times.

6.4.3 Electrochemical measurements

The rechargeable aluminum-ion batteries were assembled using coin cell in an argon-filled glove box at room temperature. To prepare the cathode, N-3DOM carbon microsphere, carbon black, and polyvinylidene fluorid (PVDF) were mixed with a weight ratio of 8:1:1. After adding N-methylpyrrolidone (NMP) as the dispersing agent, the mixture slurry was coated onto a glassy carbon current collector and then dried at 110 ℃ under vacuum for overnight. Al foil was used as the anode and glass fiber was utilized as the separator. The electrochemical performance of the batteries was evaluated in a multichannel battery tester (LAND-CT2001A) at 25 ℃.
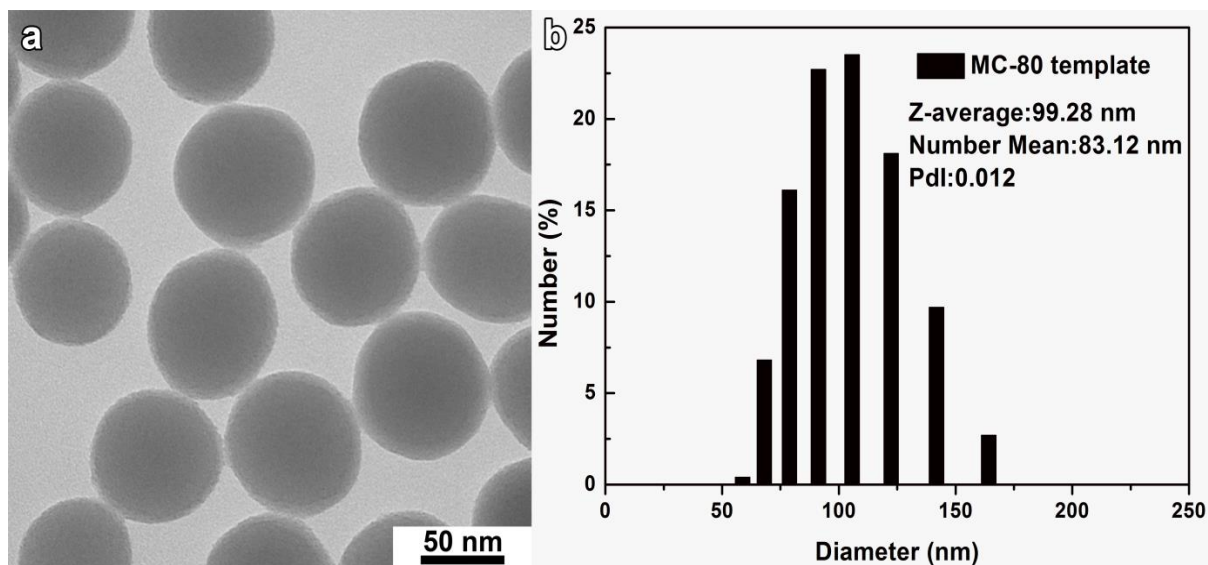
6.5 Supplementary information

Figure 6.S1 a) TEM image and b) DLS analysis of sacrificial silica template.
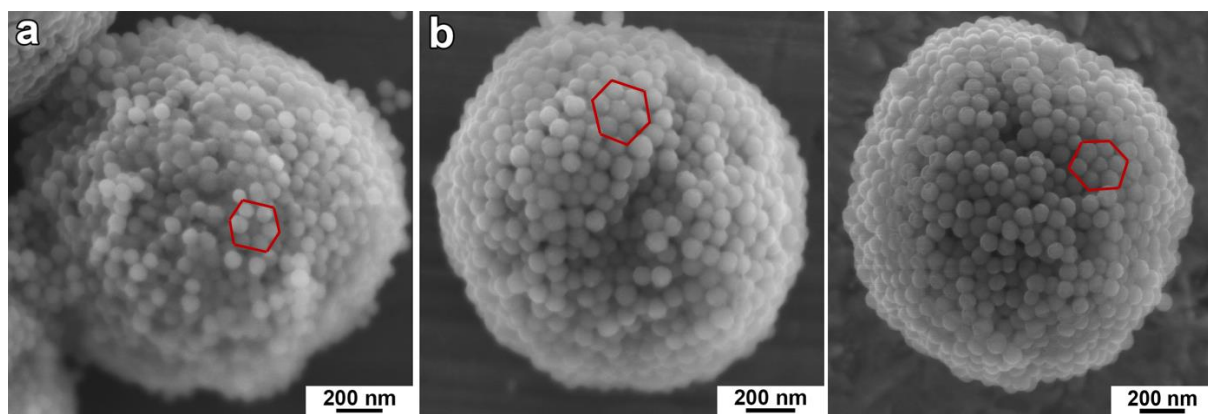

Figure 6.S2 SEM images of (a) spray-dried microspheres, (b) PPY-coated microspheres and (c) carbonized microspheres.
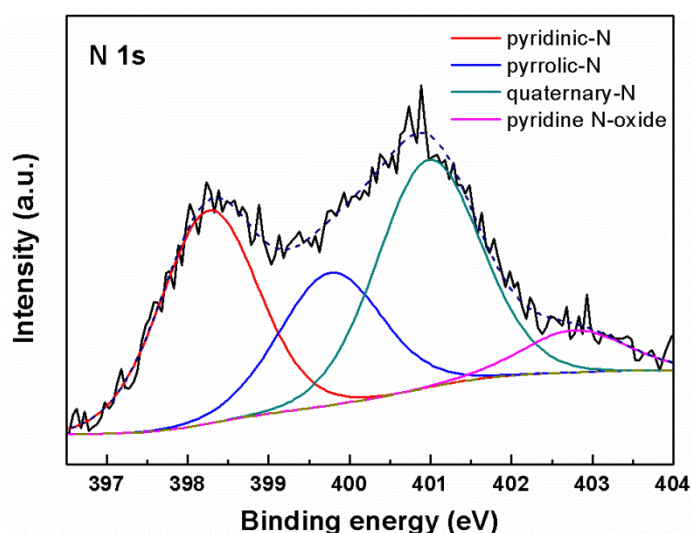
Figure 6.S3 High-resolution N1s spectra of N-3DOM carbon microsphere.

6.6 References

[1]   Lee, J.; Kim, J.; Hyeon, T., *Adv. Mater.* **2006,** *18*, 2073.

[2]   Stein, A.; Wilson, B. E.; Rudisill, S. G., *Chem. Soc. Rev.* **2013,** *42*, 2763.

[3]   Li, W.; Yue, Q.; Deng, Y.; Zhao, D., *Adv. Mater.* **2013,** *25*, 5129.

[4]   Stein, A.; Li, F.; Denny, N. R., *Chem. Mater.* **2008,** *20*, 649.

[5]   Woo, S. W.; Dokko, K.; Nakano, H.; Kanamura, K., *J. Mater. Chem.* **2008,** *18*, 1674.

[6]   Nishihara, H.; Kyotani, T., *Adv. Mater.* **2012,** *24*, 4473.

[7]   Ding, B.; Yuan, C.; Shen, L.; Xu, G.; Nie, P.; Zhang, X., *Chemistry* **2013,** *19*, 1013.

[8]   Li, W. Y.; Liang, Z.; Lu, Z. D.; Yao, H. B.; Seh, Z. W.; Yan, K.; Zheng, G. Y.; Cui, Y., *Adv. Energy Mater.* **2015,** *5*, 1500211

[9]   Ko, Y. N.; Park, S. B.; Kang, Y. C., *Small* **2014,** *10*, 3240.

[10]   Okuyama, K.; Abdullah, M.; Wuled Lenggoro, I.; Iskandar, F., *Adv. Powder Technol.* **2006,** *17*, 587.

[11]   Roberts, A. D.; Li, X.; Zhang, H., *Chem. Soc. Rev.* **2014,** *43*, 4341.

[12]   Wang, Z.; Li, F.; Ergang, N. S.; Stein, A., *Chem. Mater.* **2006,** *18*, 5543.

[13]   Xia, Y.; Mokaya, R., *Adv. Mater.* **2004,** *16*, 1553.

[14]   Su, F.; Zhao, X. S.; Wang, Y.; Zeng, J.; Zhou, Z.; Lee, J. Y., *J. Phys. Chem. B* **2005,** *109*, 20200.

[15]   Choy, K. L., *Prog. Mater. Sci.* **2003,** *48*, 57.

[16]   Nagpal, P.; Josephson, D. P.; Denny, N. R.; DeWilde, J.; Norris, D. J.; Stein, A., *J. Mater. Chem.* **2011,** *21*, 10836.

[17]   Jang, J.; Oh, J. H., *Chem. Commun.* **2004,** 882.

[18]   Gierszal, K. P.; Jaroniec, M., *J. Phys. Chem. C* **2007,** *111*, 9742.

[19]   Yu, J. S.; Kang, S.; Yoon, S. B.; Chai, G., *J. Am. Chem. Soc.* **2002,** *124*, 9382.

[20]   Liang, H.; Shinohara, K.; Minoshima, H.; Matsushima, K., *Chem. Eng. Sci.* **2001,** *56*, 2205.

[21]   Stadie, N. P.; Wang, S.; Kravchyk, K. V.; Kovalenko, M. V., *ACS Nano* **2017,** *11*, 1911.

[22]   Stöber, W.; Fink, A.; Bohn, E., *J. Colloid Interface Sci.* **1968,** *26*, 62.

Chapter 7

Conclusions and outlook

This chapter presents the conclusions of the work in this thesis and outlook for the future work.

7.1 Conclusions

Hollow-structured materials have shown wide applications in lithium-ion batteries, lithium-sulfur batteries, supercapacitors, and other energy storage devices. Besides high chemical stability, high thermal conductivity and electrical conductivity, hollow-structured materials achieve higher specific surface area compared to solid structures, thus improves the utilization of electrode materials by bringing more active sites for electrochemical reactions. Taking transition metal oxides as examples, the hollow-structured TMOs are able to buffer the large volume expansion and provide a short pathway for lithium-ion/electron diffusion. However, the stability of the delicate hollow structure during cycling is to be improved. Porous carbon materials have attracted tremendous attention as an electrode material for supercapacitors. Generally, surfactants are used to create mesoporous carbon or to prepare mesoporous silica as templates for carbon. The volumetric capacitance of mesoporous carbons has been restricted due to their low packing density. It is also desirable to prepare mesoporous carbons with high mesopore surface area and improved capacitance. Our innovative approaches have shown great potential in maintaining the stability of hollow-structured TMOs and synthesizing porous carbon microspheres with controllable pore size. The main conclusions in the thesis are specified below.

1) Polypyrrole coated zinc ferrite ($ZnFe_2O_4$-PPY) hollow spheres have been successfully synthesized via spray drying and vapour phase polymerization as anode electrode material for LIBs. We hypothesize that the cycling stability of metal oxide based anodes can be improved through the integration of hollow structuring and nanocompositing. The hollow interior is designed to buffer the large volume variation during cycling, while the structure integrity and electronic conductivity are improved by polypyrrole coating. Compared with the pristine $ZnFe_2O_4$, the $ZnFe_2O_4$-PPY shows significantly enhanced cycling stability. Our contribution provides an effective strategy to boost the electrochemical performance of transition metal oxides, which can be generally applied to other anode materials such as Si, which suffer from large volume change and insufficient conductivity issues. (Relevant content: Chapter 4)

2) To enhance the apparent density of the mesoporous carbon powder materials as electrode materials for supercapacitor, we report a novel spray drying coupled with vapour deposition method for the synthesis of nitrogen-doped mesoporous carbon microspheres. In this study, commercial silica colloidal nanoparticles are used as porogens to save the cost of products. The spray drying of silica colloidal nanoparticles gives a spherical morphology with a polydispersed distribution, increasing the packing density (0.5 g/cm^3) and the volumetric capacitance (208.1 F/cm^3). The vapour deposition of polypyrrole leads to an ultra-thin carbon network (1.8 nm) with 8 At% of nitrogen doping. The resultant nitrogen-doped mesoporous carbon microspheres shows a mesopore-

dominated (95%) structure with a high surface area (1528 m^2/g), results in an excellent gravimetric capacitance of 533.6 F/g. (Relevant content: Chapter 5)

3) Apart from mesoporous carbon microspheres, nitrogen-doped three-dimensionally ordered macroporous carbon microspheres can be synthesized through spray drying-vapour deposition method as well. It is found that the spray drying method is beneficial for the generation of macropores with a hexagonal-close-packed periodicity. A uniform carbon network with the thickness of 3.5 nm is achieved through vapour deposition of polypyrrole, followed by carbonization and HF etching. The 3DOM carbon microspheres show a hexagonal close-packed structure, a high surface area (892 m^2/g) and a high nitrogen doping (8 At%). Besides, the pore volume of resultant 3DOM carbon microspheres reaches the highest value (7.5 cm^3/g) compared to other 3DOM carbon materials. Our work opens up opportunities for the fabrication of ordered porous carbon microspheres with heteroatom-doping for wide applications. (Relevant content: Chapter 6)

In summary, hollow-structured TMOs and porous carbon materials have been synthesized as electrode materials for energy storage. Spray drying method is a facile approach for the large-scale production of hollow-structured materials. The knowledge generated from the thesis could be used as a guide for the synthesis of porous carbon microspheres with high surface area, high pore volume and narrow pore size distribution. Despite aforementioned achievements, it is still challenging to further improve the apparent density of electrode powder materials. It is also worth studying how to apply this approach in the fabrication of other electrode materials for energy storage.

7.2 Outlook

Based on the above conclusion, the following recommendations can be considered in future work.

1) Although complements are indispensable in buffering the volume variation and enhance the electrical conductivity of the electrode materials, the conducting polypyrrole used for coating usually contribute less discharge capacity than transition metal oxides. The optimal content of polypyrrole in the composite for high specific capacity, long cycle stability and excellent rate performance is worth studying.

2) We have developed a novel method to prepare polypyrrole coated zinc ferrite hollow spheres, this method is expected to the synthesis of other anode materials which suffer from large volume variations during charge-discharge, such as other TMOs, Si and Sn.

3) The spray drying coupled with vapour deposition method is a facile approach for the synthesis of porous carbon with narrow pore size distribution. Thus the correlation between pore size and capacitance of mesoporous carbon is worth studying.

4) Besides solid colloidal silica, nanoparticles with various pore structures and different morphologies can also be applied as the template for the fabrication of carbon replicas, such as nanozeolite, mesoporous silica, and metal-organic frameworks. Other carbon precursors are expected to apply in the synthesis of carbon material doped with heteroatoms.

5) Our preliminary results show the potential of nitrogen-doped 3DOM carbon microspheres for aluminium ion batteries. It is worth studying the potential of our 3DOM carbon microspheres as hosts for Li-Se/S batteries, Li-Sn batteries, and electrocatalysts.